UNIVERSITY OF SÃO PAULO
INSTITUTE OF ASTRONOMY, GEOPHYSICS AND ATMOSPHERIC SCIENCES
DEPARTMENT OF ATMOSPHERIC SCIENCES

JOÃO RAFAEL DIAS PINTO

Wave structure and dynamics in a higher Rossby number regime: implications for the atmospheric Superrotation of Venus and Titan

São Paulo

2014

JOÃO RAFAEL DIAS PINTO

Wave structure and dynamics in a higher Rossby number regime: implications for the atmospheric Superrotation of Venus and Titan

(Final version, original copy available in the library)

Thesis submitted in partial fulfillment of the requirements for the degree of Doctor of Sciences in the Institute of Astronomy, Geophysics and Atmospheric Sciences

Major Field: Meteorology

Advisor: Prof. Dr. Rosmeri Porfírio da Rocha

São Paulo

2014

ACKNOWLEDGEMENTS

I thank the State of São Paulo Research Foundation for the financial support (Grants 2010/15174-6 and 2012/13202-8) during the entire period of my doctorate, which was crucial for the development of this research.

I am extremely grateful to Dr. Jonathan Lloyd Mitchell for his precious scientific collaboration, for his constant enthusiasm and positive thinking, and for the time he dedicated to discuss many theoretical aspects of my research. My gratitude goes also to the Department of Earth, Planetary and Space Sciences of UCLA for kindly hosting me for nine months, which was a very productive (and happy) period.

I am grateful to my advisors Dr. Rosmeri Porfírio da Rocha and Dr. Tércio Ambrizzi for all support and discussions during the development of this research. I would like to thank Dr. Carlos Frederico Mendonça Raupp for the discussions on wave interactions and resonance.

I would like to sincerely acknowledge the department staff for always being so supportive during my all stay at USP.

I am truly thankful for the kind support and friendship from all my friends, André, Beatriz, Clara, Leonardo, Luciana, Marcelo, Marta, Michelle, Rosana, and especially to Nico. Having encouragement and help (not to mention lots of ears to complain to) has kept me balanced (or almost) throughout my entire doctorate and the final period of writing the thesis.

Why are things as they are and not otherwise?

Johannes Kepler (1571 – 1630) German astronomer

RESUMO

DIAS PINTO, J. R. **Dinâmica e estrutura de onda num regime de número de Rossby elevado: implicações para a Superrotação atmosférica de Vênus e Titã**. 2014. 125 f. Tese (Doutorado) – Instituto de Astronomia, Geofísica e Ciências Atmosféricas, Universidade de São Paulo, São Paulo, 2014.

A circulação geral de corpos com lenta rotação - como Vênus e Titã - é caracterizada pelo fenômeno de superrotação, no qual a atmosfera como um todo possui momento angular expressivamente maior que o da superfície sólida. O número de Rossby Ro, que caracteriza a influência da rotação sobre a circulação, é pequeno para a Terra, mas elevado para Vênus e Titã. Neste regime, é necessária a existência de um acoplamento específico de ondas que promova a geração de fluxos de momento em direção ao equador para a manutenção do escoamento zonal médio. Entretanto, ainda não é claro como tais ondas interagem entre si e com o escoamento médio. O objetivo deste estudo é o de investigar a dinâmica da superrotação atmosférica, baseado num conjunto de experimentos idealizados sob um regime de número de Rossby elevado. Os resultados mostraram que a superrotação somente emerge num planeta de lenta rotação se, simultaneamente, a inércia térmica atmosférica é aumentada e os efeitos do atrito reduzidos; a superrotação pode ser ainda obtida quando o raio planetário é reduzido. A circulação média zonal em superrotação é mantida considerando apenas a interação dinâmica de ondas de Rossby para convergir fluxo de momento na região equatorial. O ciclo de energia da circulação indicou transferência massiva de energia cinética das ondas de Rossby equatoriais para o escoamento médio em períodos curtos e esporádicos de instabilidade baroclínica. A modulação da amplitude dessas ondas sugere mecanismos não-lineares de interação onda-onda entre os modos. O regime encontrado propõe uma dinâmica mais próxima à de Titã do que a de Vênus.

Palavras-chave: Superrotação, Dinâmica Atmosférica, Vênus, Titã, Modelagem Numérica.

ABSTRACT

DIAS PINTO, J. R. **Wave structure and dynamics in a higher Rossby number regime: implications for the atmospheric Superrotation of Venus and Titan**. 2014. 125 f. Tese (Doutorado) – Instituto de Astronomia, Geofísica e Ciências Atmosféricas, Universidade de São Paulo, São Paulo, 2014.

The general circulation of slowly-rotating bodies, like Venus and Titan, is characterized by the superrotation phenomenon in which the bulk atmosphere has a larger angular momentum than the underlying solid surface. The Rossby number Ro, which characterizes the influence of rotation on the circulation, is small for Earth but large for both Venus and Titan. In this regime, it is required the existence of a specific atmospheric wave coupling generating equatorward momentum fluxes to maintain the mean zonal flow. However, it is not clear so far how these waves interact with the mean flow and among themselves. This thesis aims to study the dynamics of the atmospheric superrotation based on a set of idealized numerical experiments in a regime of higher Rossby number. It was shown that superrotation only emerges on a planet of slow rotation rate if the atmospheric thermal inertia is increased and the friction is decreased; alternatively, superrotation is obtained if planetary radius is reduced. The mean zonal superrotating circulation was maintained by only evoking the dynamical interaction between Rossby waves to converge eddy momentum fluxes at the equatorial region. The energetics of the circulation indicated massive transfer of kinetic energy from the equatorial Rossby wave to the mean flow occurring during short periods of stronger activity of the baroclinic instability. The modulation of the equatorial and extratropical Rossby wave amplitudes suggests non-linear of eddy-eddy interaction between these modes. The results suggest a dynamics closer to Titan's than Venus' regime.

Key-words: Superrotation, Atmosphere Dynamics, Venus, Titan, Numerical Modelling.

LIST OF FIGURES

Figure 1.1 – Vertical wind profile (m s^{-1}) measured by the space probes during descent through the atmosphere of: a) Venus by the Soviet Venera and Pioneer Venus probes, and b) Titan by the ESA Huygens probe. The wind plots were taken from Bougher et al. (1997), and Bird et al. (2005). The image of the spacecrafts being assembled was adapted from NASA and ESA image galleries. 2

Figure 1.2 – The hypothetical maximum of angular momentum within the fluid and the mathematical contour C. 4

Figure 1.3 – Sketched view of the main transports and the momentum balance in the Gierasch-Rossow-Williams mechanism: a) generation and maintenance of the zonal flow at higher latitudes and b) generation and consolidation of the superrotating zonal flow at the equatorial region (see text for more details). 7

Figure 1.4 – Rossby wave dynamics: regions of momentum convergence and divergence, and the acceleration of the zonal flow; and the associated areas of source and sink of wave activity. Based on Vallis (2006). 9

Figure 2.1 – σ vertical coordinate in ARW. Adapted from Skamarock et al., 2008. 13

Figure 2.2 – Horizontal and vertical discretization of the ARW. Adapted from Skamarock et al., 2008. 16

Figure 2.3 – Vertical cross section of the equilibrium temperature and the characteristic thermal and frictional time scales used in the Held-Suarez benchmark, which we use to force our model experiment. The values used for the constants in eqs. (2.21) - (2.25) are $(\Delta T)_y = 60K$, $(\Delta\theta)_z = 10K$, $p_0 = 1000\,hPa$, $\sigma_b = 0.7$, $\kappa = R/c_p = 2/7$, $\tau_a = 40\,days$ and $\tau_f = 1\,day$. 18

Figure 2.4 – Geopotential and wind signatures associated with the experiment with the sinusoidal-like heat source placed at the equatorial atmosphere: a) Matsuno (1966) results, b) WRF results in 700 hPa, after 15 days of integration. Warmer colors are related to positive geopotential heights whereas colder color to negative ones. 20

Figure 2.5 – Geopotential and wind signatures associated with the experiment with the isolated heat source placed at the equatorial atmosphere: a) Gill (1980) results, b) WRF results in 700 hPa, after 25 days of integration. Warmer colors are related to positive geopotential heights whereas colder color to negative ones. 21

Figure 2.6 – Propagation of Equatorial Rossby and Kelvin waves after the heat source was turned off on day 25: a) 8 hrs later, b) 16 hrs later and c) 24 hrs later. Dashed line denotes the sense of propagation of the modes. 22

Figure 3.1 – Schematic view of the different Rossby numbers (*R*o) and circulation regimes found on the terrestrial bodies of the solar system with substantial atmospheres. *R*o was computed based on typical scales of zonal winds (around 100 m s^{-1} for Venus and Titan and 10 m s^{-1} for Earth and Mars), rotation rate, and planetary radius. The lower panels depicts a hypothetical vertical cross section of zonal mean zonal wind (shaded, arbitrary scale) and mean overturning circulation (dashed lines, arbitrary scales) characteristic of each body's atmospheres. See text for more details. (Photo credits: NASA/JPL). 26

Figure 3.2 – Vertically-integrated total kinetic energy (x10^{6} J m^{-2}) during the last year of the simulations for each experiment. Apart from small oscillations the kinetic energy is constant, indicating a steady state has been achieved. 30

Figure 3.3 – Vertical cross-sections of the time- and zonal-mean variables. The left panels are the zonal wind component (westerly winds in shaded; easterlies in dashed line with contour each 3 m s^{-1}). The right panels are temperature (shaded, K) and stream function ψ (contour, kg s^{-1}). a) and b) Experiment control, Earth-like case (ψ contours each 20x10^{9} kg s^{-1}); c) and d) Experiment $\Omega^{*}= 1/20$ (ψ black contours each 100x10^{9} kg s^{-1}, white contours each 3x10^{9} kg s^{-1}); e) and f) Experiment $a^{*}= 1/20$ (ψ contours each 0.3x10^{9} kg s^{-1}). The nondimensional parameters were computed based on the values in Table 1 and Figure 3.5 (see text for more details). 32

Figure 3.4 – Vertically integrated net acceleration (in m s^{-1} day^{-1}) caused by the cells and the horizontal and vertical convergence of momentum by eddies: a) and b) for the Earth-like case experiment $\Omega^*= a^*= 1$; c) and d) for the $\Omega^*= 1/20$ experiment and, e) and f) for the $a^*= 1/20$ experiment. All the terms are integrated in the vertical in two layers: 1000 – 600 hPa and 100 – 600 hPa, and weighted by the atmospheric mass of the respective layer. Black lines indicate the terms related to the cells, red lines shows the eddy terms acting in the horizontal and the green lines, the eddy terms acting in the vertical. 34

Figure 3.5 – Local Rossby number (*R*o) given by the time and zonal mean zonal wind (contour, each 10 m s^{-1}) for: a) the Earth-like case experiment $\Omega^*= a^*= 1$; b) for the slow rotating $\Omega^*= 1/20$ experiment and, c) for the smaller radius $a^*= 1/20$ experiment. Calculus was based on eq. 3.6 and the values of the Table 3.1. 37

Figure 3.6 – Vertical cross-sections of the time- and zonal-mean variables. The left panels are the zonal wind component (westerly winds in shaded; easterlies in dashed line with contour each 3 m s^{-1}). The right panels are temperature (shaded, K) and stream function ψ (contour, kg s^{-1}). a) and b) Experiment $\Omega^*= 1/2$mod (ψ contours each 5x10^{9} kg s^{-1}); c) and d) Experiment $\Omega^*= 1/20$wkhd (ψ contours each 10x10^{9} kg s^{-1}).The nondimensional parameters were computed based on the values in Table 3.1. 39

Figure 3.7 – Zonal mean zonal wind profile (m s^{-1}) at 250 hPa for the experiments $a^*= 1/20$, $\Omega^* =1/20$ and $\Omega^* =1/20$mod. The black contour is the angular momentum conserving wind profile, computed as $U_M = \Omega a \frac{sin^2\phi}{cos\phi}$, where a is the planetary radius, Ω is the rotation rate and ϕ is the latitude. The purple contour is the potential vorticity (PV). Values used for the computation are based on the Table 3.1. 40

Figure 3.8 – Vertical cross section of the zonal mean convergence of momentum by the eddy transients $-\frac{1}{a\,cos^2\phi}\frac{\partial}{\partial\phi}\left(cos^2\phi\overline{[u^*v^*]}\right)$ (shaded, in m s^{-1} day^{-1}) and zonal mean zonal wind (contour with a bold line for zero values, m s^{-1}) for: a) $\Omega^* =1/20$, b) $a^* =1/20$ and, c) $\Omega^* =1/20$mod experiments. The red dashed lines indicate the levels from which the anomalies of geopotential were taken to perform the EOF analysis. 42

Figure 3.9 – Variability patterns of geopotential height (shaded, m) and horizontal wind (vector, m s^{-1}) associated with the EOFs for: a) experiment $\Omega^* =1/20$ at 400 hPa, b) experiment $a^* =1/20$ at 250 hPa and, c) experiment $\Omega^* =1/20$mod at 250 hPa. Convergence of momentum by each group of modes is also depicted in the panels on the right (black lines for 1st group and grey lines for the 2nd group, m s^{-1} day^{-1}). The percentage refers to the sum of the explained variance of the EOFs related to that mode. 43

Figure 3.10 – Variability patterns of geopotential height (shaded, m) and horizontal wind (vector, m s^{-1}) associated with the EOFs for: a) experiment Ω^* =1/20 at 600 hPa, b) experiment a^* =1/20 at 700 hPa and, c) experiment Ω^* =1/20mod at 700 hPa. Convergence of momentum by each group of modes is also depicted in the panels on the right (black lines for 1st group and grey lines for the 2nd group, m s^{-1} day^{-1}). The percentage refers to the sum of the explained variance of the EOFs related to that mode. 45

Figure 3.11 – Time series of the geopotential height anomalies (contours, m) at 250 hPa filtered in the frequency bands of the two dominant modes present in the experiment a^* = 1/20. a) 1st group, taken at latitude of 60° and b) 2nd group, taken at latitude of 39°. Both longitudes were arbitrarily chosen to be 0°. The area highlighted in grey was used to compute the meridional PV gradient and potential temperature in Figure 3.12b. 46

Figure 3.12 – Vertical cross section of time- and zonal-mean potential vorticity gradient (shaded, x10^{12}) and potential temperature (dashed lines, K) for the experiment a^* = 1/20. a) values averaged over the entire period, b) values averaged from model time 230 to 300, which is roughly represented by the grey box in Figure 3.11. 47

Figure 3.13 – Vertical cross section of the time evolution of the: a) zonal mean zonal wind component (m s^{-1}) and b) instantaneous acceleration due to eddies (m s^{-1} day^{-1}). Both variables are averaged between 15° S and 15° N latitudes. The dashed line indicated the approximated time that divides the spin-up and the steady state of the simulation. 49

Figure 3.14 – 600 hPa geopotential anomalies (shaded, m), wind (vectors, m s^{-1}) and instantaneous accelerations (contours, m s^{-1} day^{-1}) at different instants during the spin-up of the simulation a^* = 1/20: a) time 154, b) time 192, c) time 429, d) time 532, e) time 596, and f) time 629. The selected period refer roughly to the times of maximum acceleration in Figure 3.13b. 50

Figure 4.1 – Schematic vertical cross section displaying the zonal mean zonal wind (shaded, arbitrary scale) and the balance of momentum described the Gierasch-Rossow-Williams mechanism in a superrotating atmosphere. Theory shows that the vertically integrated momentum is transported poleward by the mean overturning circulation (black arrow, arbitrary size) and equatorward by eddies ("wavy" black arrow, arbitrary size) so that fast zonal current is maintained at the equatorial region. 55

Figure 4.2 – Large-scale features on the cloud-top of Venus atmosphere based on: a) schematic diagram describing the main cloudiness features observed by the ultraviolet images of Pioneer Venus; the two views represent the maximum and minium configurations of the tilt and typically occur two days apart (adapted from ROSSOW et al., 1980); and b) the horizontal combination of the horizontal structure of a extratropical Rossby wave and an equatorial Kelvin wave which explains the Y-like shape of the Venus upper level clouds (adapted from COVEY; SCHUBERT, 1982). 56

Figure 4.3 – Schematic plot of the complete energy cycle in the atmosphere as seen by Lorenz for the Northern Hemisphere. The main physical processes associated with positive conversion (given by the arrows) of the one form of energy to another is also shown (see text for more details). 62

Figure 4.4 – Vertical cross-sections of the time- and zonal-mean wind (contour, each 5 m s^{-1}) and eddy momentum fluxes (shaded, m^2 s^{-2}) for the: a) Earth-like regime and b) Superrotating regime. The blue dashed lines over the two plots indicate the vertical pressure level where the spectral analysis technique was applied (see text for more details). 64

Figure 4.5 – Latitudinal distribution of the eddy momentum flux cospectra $CP_{k,\omega}$ (m^2 s^{-2}, shaded) computed for the Earth-like regime at 250 hPa level (upper panels) and for the superrotating regime at 700 hPa (lower panels), as function of: a) and c) phase speed (integrated over all wavenumbers) and, b) and d) zonal wavenumber (integrated over all phase speeds). The contour represents the time- and zonal-mean zonal winds (m s^{-1}) averaged over the entire period at the respective levels. Dark colors indicate northward eddy momentum transport while brighter colors indicate southward transports. 67

Figure 4.6 – Frequency versus zonal wavenumber plot of the logarithm of the power spectrum of the nonaxisymmetric component of the zonal wind (m^2 s^{-2}, shaded) computed for the superrotating regime at 700 hPa level and summed for all latitude circles. Values are plotted from 3.7. 69

Figure 4.7 – Time- and zonal-mean of the variance of the filtered geopotential height (m^2) and wind components (m^2 s^{-2}) for: a) wave mode 1 ($k = 1$, $0 < \omega < 0.1$ cycles-per-day), and b) wave mode 2 ($k = 1$, $0.4 < \omega < 0.6$ cycles-per-day). The wave structures are given for the vertical pressure levels of 250 hPa (darker colors) and 700 hPa (lighter colors). 70

Figure 4.8 – Averaged spatial structure of the geopotential height and wind associated with wave mode 1 and wave mode 2. Although the scales are arbitrary, the intensity of the extratropical and tropical portions of the waves changes with height. ϕ_E and ϕ_T indicate the latitudes where the extratropical and tropical projections have their maximum amplitude; ϕ_0 delimits the meridional extension of the tropical wave guide for mode 2. See text for more details. 71

Figure 4.9 – Time- and zonal-mean distribution of the basic state zonal wind (contour, m s^{-1}) in the vertical plane (1000 – 100 hPa) averaged over the tropical zone and the extratropics; and in the meridional plane taken in 700 and 250 hPa. 72

Figure 4.10 – Time series of the geopotential height (m) taken at the specific latitudes where the mode have their maxima amplitude and at 700 hPa where the convergence of momentum by the eddies is maximized: a) during the period of the periodic behavior and b) during the period of the non-periodic behavior. Although just two periods of time have been displayed here, such patterns are found throughout the whole data. See table in Figure 4.8 for more details about the chosen latitudes. 74

Figure 4.11 – Geopotential height (shaded, m), horizontal wind (vectors, ms^{-1}) and eddy momentum flux convergence (contour, m s^{-1} day^{-1}) associated with the two wave modes during the periods of the: a), b) periodic behavior (model time 1634, 1668, 1702 and 1736) and c), d) non-periodic behavior (model time 199, 233, 267 and 301) at 250 hPa. 76

Figure 4.12 – Same of Figure 4.11 but for 700 hPa. 78

Figure 4.13 – Diagram of the total Lorenz energy cycle for the superrotating atmosphere. Here we split the energy cycle envolving the basic state and wave mode 1 (blue colors) and the basic state and wave mode 2 (red colors). The generation and dissipation terms (grey colors) are computed as residual values from the eqs. (4.7) – (4.10). The black color refers to only terms related to the basic state quantities (see text for more details). The energy amounts are given in J m^{-2} and the other terms are given in W m^{-2}. 80

Figure 4.14 – Vertically integrated energy (x10^{5} J m^{-2}) and conversion terms (W m^{-2}) for the periodic and non-periodic behaviors: a) and b) total energy of the basic state, wave modes 1 and 2; c) and d) baroclinic C_E and barotropic comversion C_K. The subscripts (0), (1) and (2) are related to the basic state (black lines), wave mode 1 (blue lines) and wave mode 2 (red lines), respectively (see text for more details). 81

Figure 4.15 – Kinetic energy transfers and baroclinic instability during three years of simulated stead-state. a) Zonal mean zonal wind (m s^{-1}) in 250 hPa averaged in the tropical region, b) The conversion of the wave mode 2 eddy kinetic energy into basic state kinetic energy (W m^{-2}), c) Time- and zonal-mean temperature difference between the latitude circles of 50° - 75° and 75° - 90° computed at the levels of 925 hPa (black line) and 400 hPa (grey line). b) Time- and zonal-mean zonal vertical wind shear (m s^{-1} hPa $^{-1}$) taken at the latitude of 75°. The grey box on the plots indicates the location within the total data set where the periods of periodic and non-periodic behavior are analyzed in the thesis. 84

Figure 5.1 – Zonal mean zonal wind and stream function taken from Figure 3.3 to represent the main differences of the atmospheric general circulation between the Earth-like and the superrotating regimes. The horizontal plot refers to an instantaneous snap-shot of the wind magnitude and direction. 88

Figure 5.2 – Relation between the simulated zonal mean circulation and the non-dimensional parameters of Rossby (R_O), Ekman (E_K) and Thermal (τ_a) numbers. The solid arrows indicate direct changes of these numbers whereas the dashed arrows depict indirect changes caused by only modification in the planetary rotation rate. The winds and mean overturning circulation (arbitrary scale) show the mean pattern obtained in different arrangement of the parameters. 89

Figure 5.3 – Sketched view of the main transport and momentum balance in a superrotating atmosphere: the role of tropical modes. 90

LIST OF TABLES

Table 3.1 – Values of rotation rate, planetary radius, thermal and frictional time scales and, the nondimensional numbers used in the numerical experiments. 29

LIST OF SYMBOLS

u	zonal wind component
v	meridional wind component
ω	pressure-coordinate vertical velocity
T	absolute temperature
Φ	geopotential
g	gravity acceleration (= 9.81 m s^{-2})
c_P	specific heat at constant parameter (= 1004 J kg^{-1} K^{-1})
R	constant of dry air (= 287 J kg^{-1} K^{-1})
Ω	planetary rotation rate
f	Coriolis parameter (= $2\Omega \sin \phi$)
β	Meridional gradient of f
a	planetary radius
k_a	forcing thermal coefficient
k_f	forcing dissipation coefficient
θ_{eq}	forcing potential temperature equilibrium profile
$\dot{Q}$	heat source of the artificial forcing
R_O	Rossby number
E_K	Ekman number
$\hat{\tau}_a$	Thermal number
ψ	mass stream function
ω	frequency
l	meridional wavenumber
k	zonal wavenumber
c	phase speed
$P_{k,\omega}$	power spectrum
$CP_{k,\omega}$	eddy momentum cospectra
ϕ	latitude
λ	longitude
ϕ_T	latitude where the tropical projection of the waves has maximum amplitude
ϕ_E	latitude where the extratropical projection of the waves has maximum amplitude

ϕ_0	latitude that defines the meridional extension of the tropical wave guide
A_Z	zonal available potential energy
K_Z	zonal kinetic energy
A_E	eddy available potential energy
K_E	eddy kinetic energy
G_Z, G_E	generation of zonal and eddy available potential energy
D_Z, D_E	dissipation of zonal and eddy kinetic energy
C_Z	energy conversion between A_Z and K_Z
C_E	energy conversion between A_E and K_E
C_A	energy conversion between A_Z and A_E
C_K	energy conversion between K_E and K_Z
$\bar{\sigma}$	averaged static stability parameter
t	time
α	specific volume
Q	diabatic heating
p_b, p_t	pressure-level limits of the vertical integration (1000 – 10 hPa)
F	frictional force

SUMMARY

CHAPTER 1. Introduction **1**

1.1. Atmospheric Superrotation: observational facts and physical constraints 2

1.2. Organization of the thesis 10

CHAPTER 2. Numerical Procedures **12**

2.1. The WRF Atmospheric Model 13

2.2. The Held-Suarez Benchmark 16

2.3. Sensitivity experiments 19

CHAPTER 3. Results – Part I **23**

Atmospheric superrotation in an idealized GCM: parameter dependence of the eddy response

3.1. Theoretical background 24

3.2. Methodology 28

3.2.1. Dimensionless governing equations and control parameters 28

3.2.2. Numerical experiments 29

3.3. Results 30

3.3.1. Circulation regimes at low and high Rossby numbers 30

3.3.2. Mean convergence of momentum and net accelerations in the steady state 33

3.3.3. The influence of the rotation rate on the parametric regime 36

3.3.4. Wave and eddies in the high Ro regime 40

3.3.5. Dynamical origin of the modes from experiment $a^* = 1/20$ 46

3.3.6. Analysis of the spin-up period of the model 48

3.4. Discussion 51

CHAPTER 4. Results – Part II **53**

Wave structure and dynamics in a superrotating terrestrial atmosphere

4.1. Theoretical background 54

4.2. Methodology 58

4.2.1. Numerical experiments 58

4.2.2. Spectral analysis technique 58
4.2.3. The Lorenz energy cycle 59
4.3. Results 64
4.3.1. Earth-like vs. Superrotating regime: zonal wind and eddy momentum fluxes distribution 64
4.3.2. Spectral analysis of the eddy component of the wind 66
4.3.3. Wave structure and properties in the superrotating state 68
4.3.3a. Spatial characteristics of the filtered modes 68
4.3.3b. Temporal behavior of the filtered modes 74
4.3.3c. Interactions among the basic state and the eddies 79
4.4. Discussion 85
CHAPTER 5. Final discussions and beyond 87
REFERENCES 92

CHAPTER 1.

Introduction

1.1. Atmospheric Superrotation: observational facts and physical constraints

The study of the large-scale atmospheric circulation of Venus and Titan, the biggest Saturn moon, is still a challenging subject in geophysical fluid dynamics. Direct and indirect measurements of wind magnitude have shown a strong zonal flow being the dominant component of the circulation. Figure 1.1 shows the vertical wind profile data taken by the space probes of the Soviet Venera series and the European Space Agency's Huygens probe which landed on the surface of Venus and Titan, respectively. These *in situ* measurements revealed winds reaching more than 100 m s^{-1} at high levels, even at the equator, and then almost monotonically decreasing toward the surface.

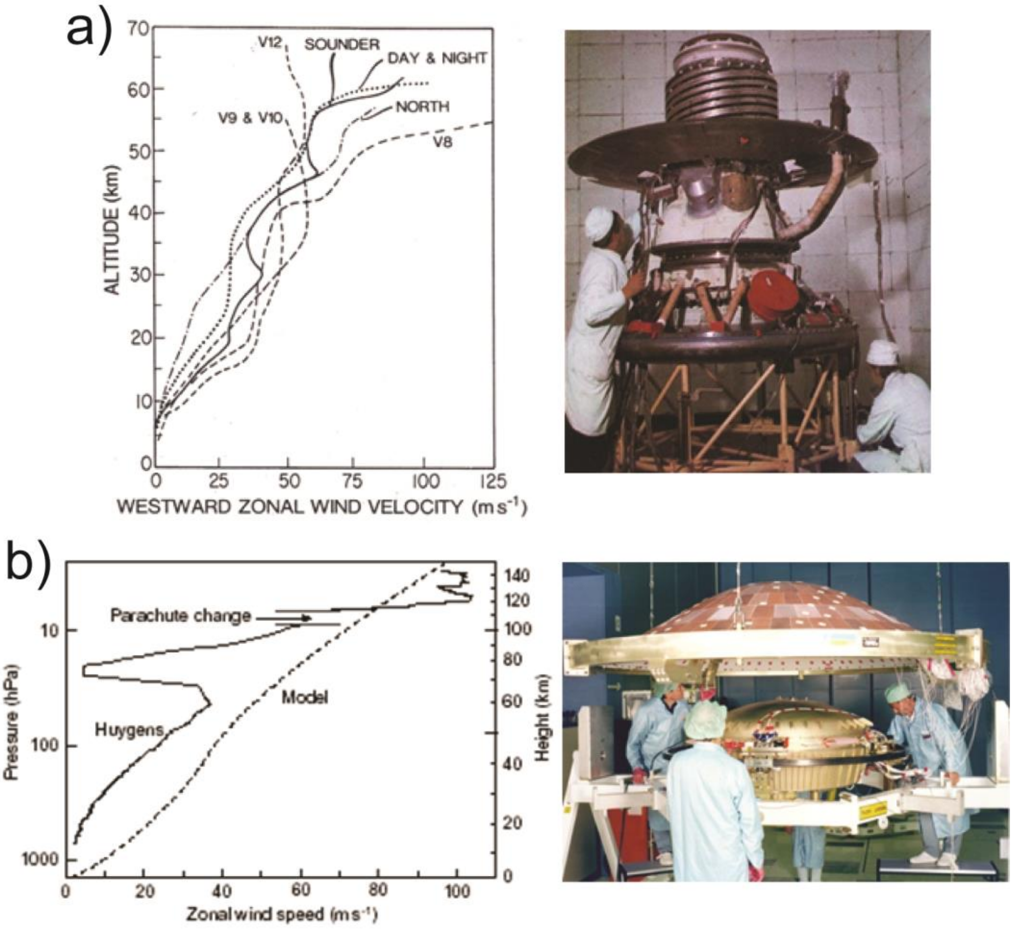

Figure 1.1 – Vertical wind profile (m s^{-1}) measured by the space probes during descent through the atmosphere of: a) Venus by the Soviet Venera and Pioneer Venus probes, and b) Titan by the ESA Huygens probe. The wind plots are taken from Bougher et al. (1997), and Bird et al. (2005). The image of the spacecrafts being assembled was adapted from NASA and ESA image galleries.

Such strong zonal winds at the upper level of Venus and Titan's atmosphere are in the so-called, superrotational state. This fact implies in a very non-intuitive situation: the bulk atmosphere rotates much faster than the solid surface. In Venus, for example, the whole atmosphere circles the planet in about 4.5 days whereas a point fixed at the surface takes 243 days for the same movement, since Venus has a very slow rotation rate. Titan, whose rotation period is about 16 days, is also a slower rotator and presents the same superrotating regime.

One of the key points of any study in superrotation is to explain how the maximum of angular momentum in the equatorial region, which arises from the strong winds there, is maintained in slower-rotator bodies. For that consider a two-dimensional atmosphere by ignoring any kind of asymmetry in the zonal direction. Thus, the x-component of the momentum equation can be given as

$$\frac{\partial u}{\partial t} + v\frac{\partial u}{\partial y} + w\frac{\partial u}{\partial z} - fv = \nu\frac{\partial^2 u}{\partial z^2} \tag{1.1}$$

Supposing a Boussinesq fluid, we have from the equation of mass conservation that $\nabla \cdot \vec{V} = 0$, so it is possible to combine eq. (1.1) and the non-divergence to write eq. (1.1) in the flux form,

$$\frac{\partial u}{\partial t} + \frac{\partial (uv)}{\partial y} + \frac{\partial (uw)}{\partial z} - fv = \nu\frac{\partial^2 u}{\partial z^2} \tag{1.2}$$

Now, consider the Earth's spherical geometry and by using the definition of angular momentum, we can write eq. (1.2) as

$$\frac{\partial M}{\partial t} = -\frac{1}{a\cos\phi}\frac{\partial (Mv\cos\phi)}{\partial \phi} - \frac{\partial (Mw)}{\partial z} + D \tag{1.3}$$

where, $M = (u + \Omega a\cos\phi)a\cos\phi$ represents the angular momentum per unit mass, and $D \approx \nabla \cdot (\nu\nabla M)$ represents frictional effects. Eq. (1.3) can be expressed in terms of divergence of fluxes, so

$$\frac{\partial M}{\partial t} = -\nabla \cdot M\vec{V} + \nabla \cdot (\nu\nabla M)$$

$$\frac{\partial M}{\partial t} = -\nabla \cdot (M\vec{V} - \nu\nabla M) \tag{1.4}$$

Let's now suppose that M has a maximum, $M = M_0$, in the interior of the fluid and this fluid is in a *steady state*. Following Held and Hou (1980), if we can draw a closed curve C surrounding this point (Figure 1.2), in which $M = M_0 - \delta$, and integrate eq. (1.4) around C we have:

$$\oiint \nabla \cdot \left(M\vec{V} - \nu \nabla M\right) dA = 0$$

where *dA* is an infinitesimal element of area bounded by *C*.

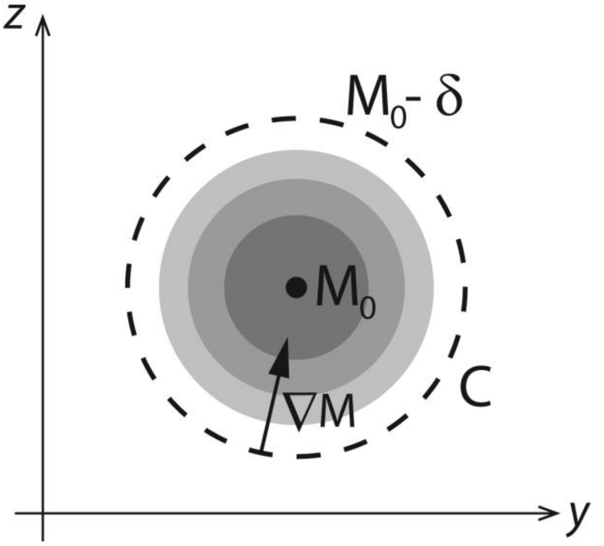

Figure 1.2 – The hypothetical maximum of angular momentum within the fluid and the mathematical contour *C*.

Thus,

$$\oint_C M\vec{V} \cdot \hat{n} dl = \oint_C \nu \nabla M \cdot \hat{n} dl \tag{1.5}$$

but from mass conservation, if we do not have sources or sinks of mass inside *C* we have from eq. (1.5),

$$\oint_C M\vec{V} \cdot \hat{n} dl = (M_0 - \delta) \oint_C \vec{V} \cdot \hat{n} dl = 0 \tag{1.6}$$

which means the net advective fluxes out of this region of the fluid is zero.

The right side of eq. (1.5), however, is

$$\oint_C \nu \nabla M \cdot \hat{n} dl < 0 \tag{1.7}$$

since $\nabla M \cdot \hat{n} < 0$ because *C* encircles a point of maximum. Therefore the non-zero outward diffusive fluxes (downgradient) tend to reduce the maximum in *M*. Such a situation is inconsistent, so *M* cannot have a maximum in the interior of the fluid in a steady state. According to Held and Hou (1980) only at a lower boundary the surface can balance the diffusive loss of westerly momentum into the interior.

This situation can be expressed by the Hide's theorem (HIDE, 1969): *an axisymmetric circulation in steady state cannot have a maximum of angular momentum* *except at the lower boundary*. We have three immediate consequences from this theorem (based on HELD; HOU, 1980):

- the maximum value of M must occur at the surface when the zonal winds is $u \leq 0$ (easterlies are allowed!);
- a threshold for M is given by its value at the equator Ωa^2 (where Ω is the rotation rate, a is the planetary radius);
- the zonal wind u must be everywhere in the fluid less than or equal to

$$U_M = \Omega a \frac{\sin^2\phi}{\cos\phi} \tag{1.8}$$

where U_M is the angular momentum-conserving wind profile.

A superrotating state implies either the atmosphere has more M than it would have in solid-body rotation with the underlying surface Ωa^2 (defined as **local superrotation**), or the entire atmosphere has more M than a state in solid-body rotation with the underlying surface (defined as **global superrotation**).

Following Hide's theorem, *equatorial superrotation* is inexistent in a purely axisymmetric circulation and therefore as the main consequence local superrotation must have longitudinally asymmetric motions which transport angular momentum ($[u^* v^*] \neq 0$) up the gradient of mean angular momentum.

This result has a profound implication for the superrotation in both Venus and Titan atmospheres; in order to maintain the surplus of angular momentum at the equator, it is necessary the existence of some disturbed mechanism that carries momentum toward the region.

In attempting to explain how angular momentum is fed in the equatorial upper atmosphere of Venus to maintain the superrotation, Gierash (1975) proposed that the mean meridional circulation (Hadley cell) driven by pole-equator thermal contrast would carry a fraction of the angular momentum from the lower to the upper atmosphere. According to the author, since the lower atmosphere gains angular momentum from the frictional interaction with the solid surface, the Hadley cell would transport momentum upward only if its poleward branch did not conserve angular momentum. Gierasch (1975) parameterized this latter effect by including a strong horizontal eddy diffusion of momentum in his model. Several mechanisms have been proposed to explain this eddy diffusion, as for example, by 1) large-scale barotropic waves (ROSSOW; WILLIAMS, 1979; HOURDIN et al., 1995; WILLIAMS, 2003; LUZ; HOURDIN, 2003), 2) thermal tides (FELS; LINDZEN, 1974; NEWMAN; LEOVY, 1992; TAKAGI; MATUSDA, 2007), and 3) gravity waves (LEOVY, 1973; HOU; FARRELL, 1987; GIERASCH, 1987; YAMAMOTO; TAKAHASHI, 2003).

Rossow and Williams (1979) showed that under a condition of strong static stability, small horizontal temperature gradient and a weak enough forcing of the flow, the upper atmosphere of Venus would present quasi-barotropic non divergent eddy motions that would provide the equatorward momentum transport necessary to complete the Gierasch cyle. Such bi-dimensional barotropic disturbances could be able to transport momentum but no heat, thus satisfying one restriction of the Gierasch model. According to Rossow and Williams (1979) to consider a weakly forced flow, the advective time scale of the mean circulation had to be greater than that related to the redistribution of momentum by eddies ($> 10^6$ s).

The combination between these ideas is referred as the Gierasch-Rossow-Williams mechanism (GRW), which is still used today to describe the global balance of angular momentum that occurs in a superrotating atmosphere. This model is fundamentally based on two elements: the existence of a mean overturning circulation that carries momentum poleward and non-axisymmetric disturbances that complete the balance by transporting momentum equatorward. First let us consider an initial solid body rotation state. Since angular momentum per unit mass increases with height in the atmosphere, the upward branches of the Hadley cells transport angular momentum aloft and, afterwards, toward the poles. Under slower rotation rate regimes, the Hadley cell in an equinoctial situtation extends deep into higher latitudes (WILLIAMS, 1988A; NAVARRA; BOCALLETI, 2002) in both hemispheres. Therefore, by conserving angular momentum the poleward branch of the overturning circulation builds-up a symmetric pair of jets at mid- and high-latitudes (Figure 1.3a).

Under the slow rotation regime, any structure of jet in the zonal flow should be barotropically unstable (ROSSOW; WILLIAMS, 1979). Thus as the jet gets stronger, it will become barotropically unstable; eddies will develop and they will transport momentum toward the equatorial region. Therefore, in this condition, the barotropically unstable jet could produce large-scale Rossby waves in the high-latitudes toward the equatorial region, and these modes would induce convergence of angular momentum necessary to maintain the winds there (Figure 1.3b).

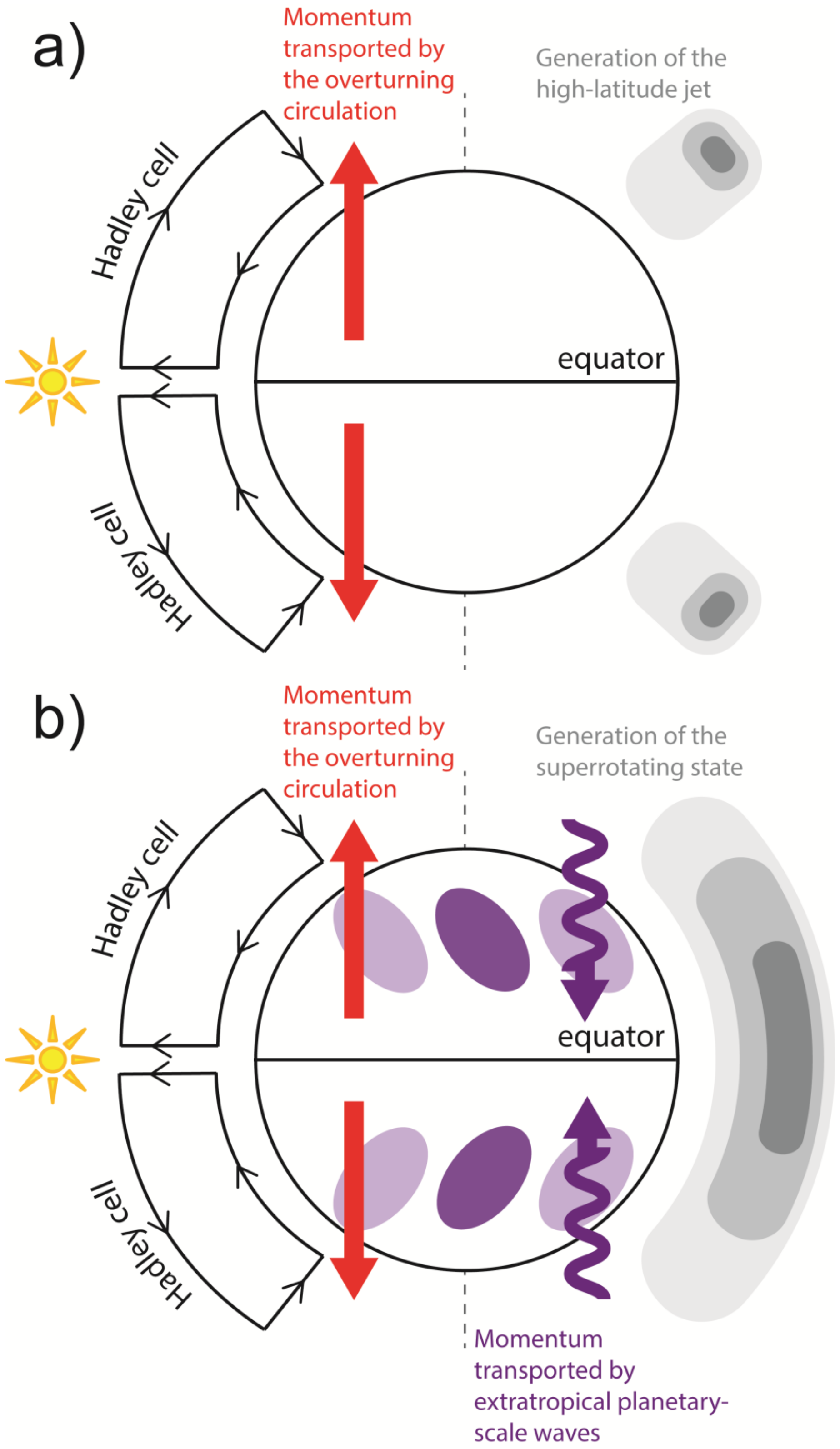
a)
Momentum transported by the overturning circulation
Generation of the high-latitude jet
Hadley cell
equator
Hadley cell
b)
Momentum transported by the overturning circulation
Generation of the superrotating state
Hadley cell
equator
Hadley cell
Momentum transported by extratropical planetary-scale waves

Figure 1.3 – Sketched view of the main transports and the momentum balance in the Gierasch-Rossow-Williams mechanism: a) generation and maintenance of the zonal flow at higher latitudes and b) generation and consolidation of the superrotating zonal flow at the equatorial region (see text for more details).

Propagation from extratropical to tropical regions is therefore required from eddies in order to maintain the superrotating jet. Although this model presents an intuitive and concise physical mechanism to explain superrotation, it is necessary to look at this point more carefully. For that, consider the linearized non-divergent vorticity equation, written in terms of stream function ψ,

$$\left(\frac{\partial}{\partial t} + U\frac{\partial}{\partial x}\right)\nabla^2\psi + \beta\frac{\partial\psi}{\partial x} = 0 \tag{1.9}$$

where $\zeta = \nabla^2\psi$ is the relative vorticity.

By applying the wave-solution $\psi(x, y, t) = \Psi e^{i(kx+ly-\omega t)}$ in eq. (1.9), we obtain the dispersion relation for the Rossby waves:

$$\omega = Uk - \frac{\beta k}{k^2 + l^2} \tag{1.10}$$

The meridional component of the group velocity is given by

$$c_g^y = \frac{\partial\omega}{\partial y} = \frac{2\beta kl}{(k^2 + l^2)^2} \tag{1.11}$$

Since the energy flux travels at the group velocity, the energy flux must be directed away from the source region (VALLIS, 2006), and therefore the group velocity must be away from this region as well.

The eddy component of the wind field can also be expressed in terms of the stream function as follows,

$$u^* = -\frac{\partial\psi}{\partial y} \qquad v^* = \frac{\partial\psi}{\partial x} \tag{1.12}$$

Applying the same wave-solution in these two relations, we obtain

$$\overline{[u^*v^*]} = -\frac{1}{2}|\Psi|^2 kl \tag{1.13}$$

Thus based on eq. (1.11) and eq. (1.13), northward of the stirring region $kl > 0$, implying in positive energy flux and negative momentum transport. Southward of this stirring region, instead, $kl < 0$ leading to negative energy flux and positive momentum transport (Figure 1.4). That is, the momentum fluxes associated with the Rossby waves is toward to the source region (VALLIS, 2006), and converges there. This fact leads to net eastward acceleration in the source region.

As the Rossby wave propagates it will find a latitude at which the flow has the same speed of the wave ($[U - c] \to 0$). Mathematically, from eq. (1.10), if $[U - c] \to 0$, l grows once it is inversely proportional to the difference of the velocities between the basic state and the disturbance,

$$l = \pm\left(\frac{\beta}{U - c} - k^2\right)^{\frac{1}{2}} \tag{1.14}$$

Physically if l grows, the group velocity (eq. 1.11) decreases rapidly so as any attenuation will have a longer time interval to act on these waves, leading to their dissipation. The latitude where this process occurs is often termed as *critical latitude*; Rossby waves will break and dissipate leading to momentum divergence there. Basing on arguments above such divergence will produce westward flow at the sink region (Figure 1.4).

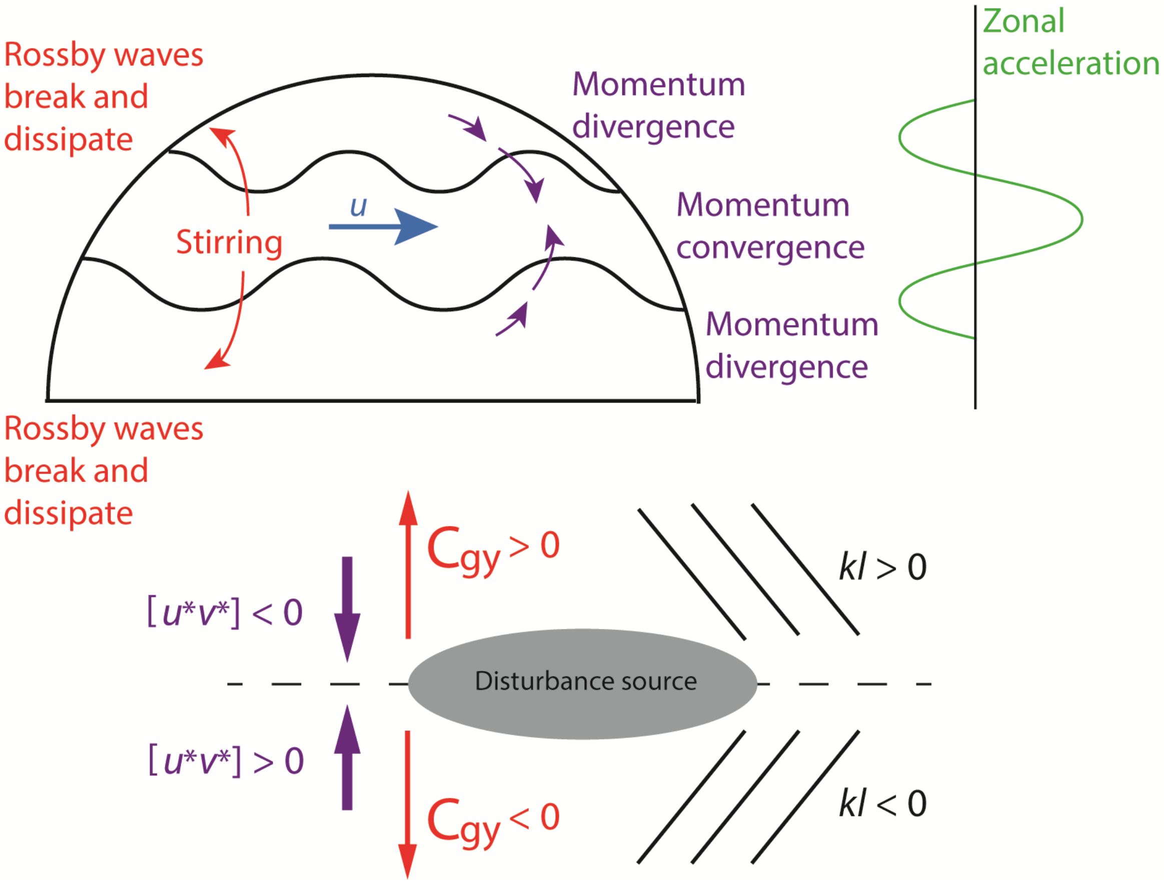
Rossby waves break and dissipate
Momentum divergence
Zonal acceleration
Stirring
u
Momentum convergence
Momentum divergence
Rossby waves break and dissipate
$C_{gy} > 0$
$[u^*v^*] < 0$
$kl > 0$
Disturbance source
$[u^*v^*] > 0$
$C_{gy} < 0$
$kl < 0$

Figure 1.4 – Rossby wave dynamics: regions of momentum convergence and divergence, and the acceleration of the zonal flow; and the associated areas of source and sink of wave activity. Based on Vallis (2006).

Two fundamental properties of the Rossby waves can be then established (based on HELD, 1999):

(i) *"When Rossby waves are forced at one latitude and propagate to some other latitude where they dissipate, they will decelerate the zonal flow* ($\partial u/\partial t < 0$) *in the dissipation region, and they accelerate the flow* ($\partial u/\partial t > 0$) *in the source region."*

(ii) *"Rossby waves will preferentially break and dissipate in those regions where* $U - c$ *is small, where* c *is the phase speed of the wave."*

The mechanism based on meridionally propagating extratropical Rossby waves would lead to deceleration of the flow in the equatorial regions and, therefore, these waves could not properly maintain the equatorial superrotation as proposed by the GRW model. Therefore this statement leads to a misconception regarding the dynamical origin of the modes and how they maintain the superrotation.

1.2. Organization of the thesis

The discussion above evokes the need of a better understanding on the main mechanisms responsible for the maintenance of the superrotation in a higher Rossby-number atmosphere. This thesis will focus on the analysis of the superrotation simulated with a global numerical atmospheric model and aims two specific points:

(i) The description of the main elements present in a higher Rossby-number atmosphere, highlighting the conditions necessary to reproduce superrotation in a general circulation model;

(ii) The study of the dynamical mechanisms behind the process of wave-mean flow interaction that drives the atmospheric superrotation.

The present study considered several assumptions:

- If eddies are excited in the tropical region, rather than in the extratropics, the momentum transport generated by these disturbances could provide the dynamical support for the superrotation;
- Other eddy sources such as thermal tides and small scale gravity waves are not considered;
- Seasonal cycles are also not considered, which means that the analyses are based on an equinoctial situation with a symmetric diabatic forcing. This is a very good approximation for Venus, where the Sun only goes to 2.6° from the equator, and the year has less than two solar days. But Titan spends almost 15 years with the Sun on each hemisphere, has obliquity of 27°, the year has over 600 solar days, and therefore the atmosphere circulation changes a lot between seasons;
- An idealized Earth-like treatment in a higher Rossby number regime is used to simulate the superrotation, so that the atmospheric properties and parameters of Venus and Titan are not considered. Here the higher Rossby number regime is

considered enough to capture the dynamical state of the superrotating atmosphere;

- The dynamical conditions reproduced in the simulations could be achieved in slowly-rotating rocky extrasolar planets;
- Although horizontal and vertical resolutions have impact in any simulation, it is beyond the scope of this thesis to explore the effects of either a finer or a poorer resolution on the strength of the superrotation;
- The same is valid for different numerical schemes of diffusion and time integration present in the model.

The main analysis and results are presented as follows. *Chapter 2* will describe the atmospheric general circulation model WRF, the idealized treatment used in the simulations to reproduce the diabatic forcing and friction, and some characteristics of the numerical experiments of sensitivity. *Chapter 3* will present the first part of the results, which aims to investigate under what conditions superrotation is properly simulated in a higher Rossby number regime. The main dynamical differences regarding the average zonal structure, momentum balance and eddies among several numerical experiments will be analyzed. *Chapter 4* will present in the details the second part of the results by describing the horizontal and vertical structure of the modes present in the superrotating state. The dynamics of such a kind of general circulation will be investigated by emphasizing the wave-mean flow interaction and the maintenance of the superrotation through the Lorenz energy cycle. Finally, *Chapter 5* will bring the main conclusion of the study and recommendations for future work.

CHAPTER 2.

Numerical procedures

2.1. The WRF Atmospheric Model

The numerical simulations were performed with version 3.3.1 of the Weather Researcher and Forecast Model (WRF; SKAMAROCK et al., 2008) dynamical core (ARW – Advanced Research WRF). Although originally designed for a regional domain, this model has been used for planetary applications, as for example, global simulations in Mars and Titan atmospheres (RICHARDSON et al., 2007; NEWMAN et al., 2011; TOIGO et al., 2012).

According to Skamarock et al. (2008) the WRF ARW core integrates the compressible, non-hydrostatic Euler equations, which are written in flux form using the variables that have conservation properties. These equations are formulated using the terrain-following vertical coordinate sigma σ,

$$\sigma = \frac{p_h - p_{ht}}{\mu} \tag{2.1}$$

where $\mu = p_{hs} - p_{ht}$, p_h is the hydrostatic component of the pressure, and p_{hs} and p_{ht} are, respectively, the surface and top boundary pressures. σ varies from 1 at the surface to 0 at the upper boundary of the vertical domain of the model (Figure 2.1).

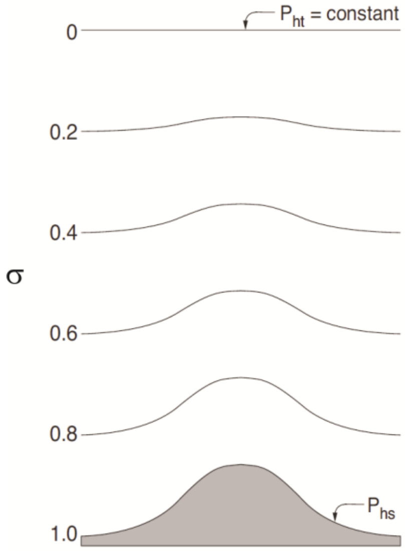

Figure 2.1 – σ vertical coordinate in ARW. Adapted from Skamarock et al., 2008.

The appropriate flux form variables are written in terms of the mass per unit area $\mu(x,y)$ within the column in the model at (x,y) such as,

$$\vec{U} = \mu\vec{u} = (U, V, W) \tag{2.2a}$$

$$\Sigma = \mu\dot{\sigma} \tag{2.2b}$$

$$\Theta = \mu\theta \tag{2.2c}$$

In these relations, $\vec{u} = (u, v, w)$ is the tridimensional covariant velocity field; $\dot{\sigma}$ is the vertical velocity in sigma coordinates; θ is the potential temperature. The non-conserved variables, which are also part of the governing equations, are $\Phi = gz$ the geopotential, p pressure, and $\alpha = \rho^{-1}$ the specific volume.

By using the definition in eqs. (2.2a), (2.2b) and (2.2c) the Euler equations in flux-form can be written as

$$\frac{\partial U}{\partial t} + \left(\nabla \cdot \vec{U}u\right) - \frac{\partial}{\partial x}\left(p\frac{\partial \Phi}{\partial \sigma}\right) + \frac{\partial}{\partial \sigma}\left(p\frac{\partial \Phi}{\partial x}\right) = F_U \tag{2.3}$$

$$\frac{\partial V}{\partial t} + \left(\nabla \cdot \vec{U}v\right) - \frac{\partial}{\partial y}\left(p\frac{\partial \Phi}{\partial \sigma}\right) + \frac{\partial}{\partial \sigma}\left(p\frac{\partial \Phi}{\partial y}\right) = F_V \tag{2.4}$$

$$\frac{\partial W}{\partial t} + \left(\nabla \cdot \vec{U}w\right) - g\left(\frac{\partial p}{\partial \sigma} - \mu\right) = F_W \tag{2.5}$$

The system of equations above with the relations for thermodynamics, mass continuity and geopotential tendency,

$$\frac{\partial \Theta}{\partial t} + \left(\nabla \cdot \vec{U}\theta\right) = F_\Theta \tag{2.6}$$

$$\frac{\partial \mu}{\partial t} + \left(\nabla \cdot \vec{U}\right) = 0 \tag{2.7}$$

$$\frac{\partial \Phi}{\partial t} + \mu^{-1}\left[\left(\vec{U} \cdot \nabla\Phi\right) - gW\right] = 0 \tag{2.8}$$

and along with the diagnostic relation for the inverse density

$$\frac{\partial \Phi}{\partial \sigma} = -\alpha\mu \tag{2.9}$$

and the equation of state

$$p = p_0\left(\frac{R_d\theta}{p_0\alpha}\right)^\gamma \tag{2.10}$$

form the governing equations of the WRF ARW dynamical core. In eqs. (2.3) – (2.9)

$$\nabla \cdot \vec{U}b = \frac{\partial(Ub)}{\partial x} + \frac{\partial(Vb)}{\partial y} + \frac{\partial(\Sigma\mathrm{b})}{\partial \sigma} \tag{2.11}$$

$$\vec{U} \cdot \nabla b = U\frac{\partial b}{\partial x} + V\frac{\partial b}{\partial y} + \Sigma\frac{\partial b}{\partial \sigma} \tag{2.12}$$

where b represents a generic variable. $\gamma = c_p/c_V = 1.4$ is the ratio of the heat capacities for dry air, R_d is the gas constant of dry air, and p_0 is the pressure of reference, typically taken 10^5 Pa. The right hand side terms F_U, F_V, F_W and F_Θ describe the forcing terms, as for example, model physics, mixing, Earth's rotation and spherical projections.

According to Skamarock et al. (2008), orthogonal projections to the sphere require that the physical distances between the grid points Δx and Δy in the projection vary with position on the grid. Therefore to transform the governing equations, map factors m_x and m_y are included by redefining the momentum variables as

$$(U,V,W,\Sigma)=\left(\frac{\mu u}{m_y},\frac{\mu v}{m_x},\frac{\mu w}{m_y},\frac{\mu\dot{\sigma}}{m_y}\right) \tag{2.13}$$

where $(m_x,m_y)=(\Delta x,\Delta y)/distance\ on\ the\ Earth$ represent the map factors.

In this study, the hydrostatic approximation for a dry atmosphere was used to simplify the set of equations. Thus eq. (2.5) is replaced to eq. (2.9), and the governing equations can be expressed as

$$\frac{\partial U}{\partial t}+m_x\left[\frac{\partial(Uu)}{\partial x}+\frac{\partial(Vu)}{\partial y}\right]+\frac{\partial(\Sigma \mathrm{u})}{\partial\sigma}+\left(\frac{m_x}{m_y}\right)\left[\mu\alpha\frac{\partial p}{\partial x}+\frac{\partial p}{\partial\sigma}\frac{\partial\Phi}{\partial x}\right]=F_U \tag{2.14}$$

$$\frac{\partial V}{\partial t}+m_y\left[\frac{\partial(Uv)}{\partial x}+\frac{\partial(Vv)}{\partial y}\right]+\left(\frac{m_y}{m_x}\right)\frac{\partial(\Sigma \mathrm{v})}{\partial\sigma}+\left(\frac{m_y}{m_x}\right)\left[\mu\alpha\frac{\partial p}{\partial y}+\frac{\partial p}{\partial\sigma}\frac{\partial\Phi}{\partial y}\right]=F_V \tag{2.15}$$

$$\frac{\partial\Phi}{\partial\sigma}=-\alpha\mu \tag{2.16}$$

$$\frac{\partial\Theta}{\partial t}+m_x m_y\left[\frac{\partial(U\Theta)}{\partial x}+\frac{\partial(V\Theta)}{\partial y}\right]+m_y\frac{\partial(\Sigma\Theta)}{\partial\sigma}=F_\Theta \tag{2.17}$$

$$\frac{\partial\Phi}{\partial t}+\mu^{-1}\left[m_x m_y\left(U\frac{\partial\Phi}{\partial x}+V\frac{\partial\Phi}{\partial y}\right)+m_y\Sigma\frac{\partial\Phi}{\partial\sigma}-m_y gW\right]=0 \tag{2.18}$$

and

$$p=p_0\left(\frac{R_d\theta}{p_0\alpha}\right)^\gamma \tag{2.19}$$

The curvature and Coriolis terms for the momentum equation are given as

$$F_{U\,cor}=\left(\frac{m_x}{m_y}\right)\left[fV+\frac{uV}{a}tan\phi\right]-\frac{uW}{a}-eW\cos\varphi_r \tag{2.20a}$$

$$F_{V\,cor}=\left(\frac{m_y}{m_x}\right)\left[-fU+\frac{uU}{a}tan\phi-\frac{uW}{a}-eW\cos\varphi_r\right] \tag{2.20b}$$

where φ_r is the local rotation angle between the y-axis and the meridians, ϕ is the latitude, $f=2\Omega\sin\phi$, $e=2\Omega\cos\phi$, Ω is the angular rotation rate of the Earth, and a the planetary radius.

Regarding the model discretization, ARW uses a time-split integration scheme, in which significantly meteorological slow- or low-frequency modes are integrated using a 3rd Runge-Kutta time integration scheme. High-frequency modes are integrated over a smaller time steps in order to maintain numerical stability (SKAMAROCK et al., 2008).

In space, ARW uses a C grid staggering for the variables as shown in Figure 2.2. Normal velocities are then staggered one-half grid length from the thermodynamic variables. The grid distances in *x*- and *y*-axis are constant in the model formulation; changes in the physical grid lengths associated with the various map projections are taken into account by the map factors described in eqs. (2.13).

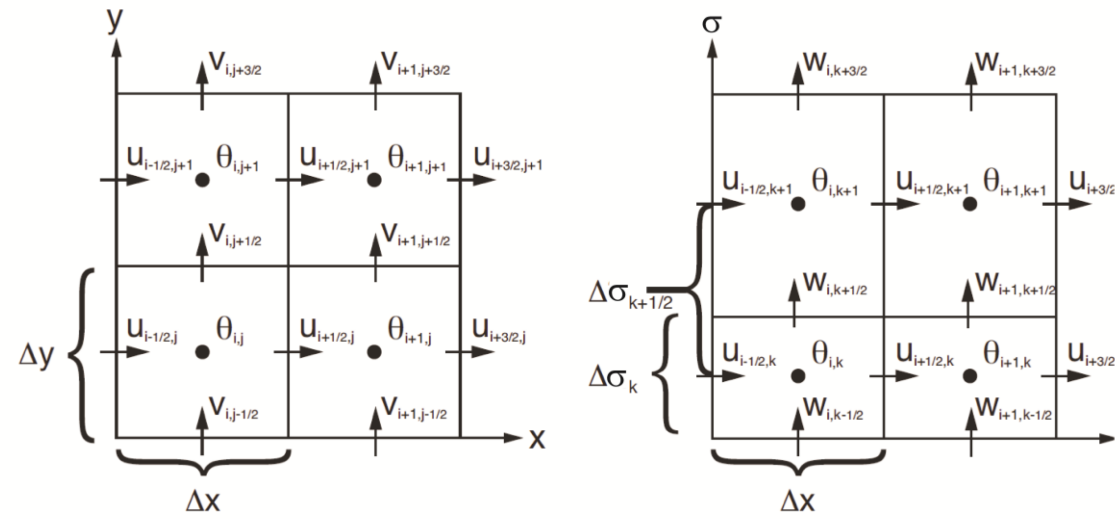
y
$v_{i,j+3/2}$
$v_{i+1,j+3/2}$
$u_{i-1/2,j+1}$
$\theta_{i,j+1}$
$u_{i+1/2,j+1}$
$\theta_{i+1,j+1}$
$u_{i+3/2,j+1}$
$v_{i,j+1/2}$
$v_{i+1,j+1/2}$
Δy
$u_{i-1/2,j}$
$\theta_{i,j}$
$u_{i+1/2,j}$
$\theta_{i+1,j}$
$u_{i+3/2,j}$
$v_{i,j-1/2}$
$v_{i+1,j-1/2}$
x
Δx
σ
$w_{i,k+3/2}$
$w_{i+1,k+3/2}$
$u_{i-1/2,k+1}$
$\theta_{i,k+1}$
$u_{i+1/2,k+1}$
$\theta_{i+1,k+1}$
$u_{i+3/2}$
$\Delta\sigma_{k+1/2}$
$w_{i,k+1/2}$
$w_{i+1,k+1/2}$
$\Delta\sigma_{k}$
$u_{i-1/2,k}$
$\theta_{i,k}$
$u_{i+1/2,k}$
$\theta_{i+1,k}$
$u_{i+3/2}$
$w_{i,k-1/2}$
$w_{i+1,k-1/2}$
Δx

Figure 2.2 – Horizontal and vertical discretization of the ARW. Adapted from Skamarock et al., 2008.

Since global simulations were performed in this study, the assumption of a spherical geometry lead to the problems of numerical instabilities associated with the poles. To solve that, WRF ARW uses polar filtering in order to reduce the time step restriction associated with the convergence of the gridlines toward the poles. For a given variable, this filtering is accomplished by applying a one-dimensional Fourier transform to this variable over a constant latitude circle and poleward a specified latitude value (here defined as the default value of 45°). The Fourier coefficients with wavenumbers above a prescribed threshold are truncated, after which a transformation back to physical space is applied, completing the filter step (SKAMAROCK et al., 2008).

2.2. The Held-Suarez Benchmark

The numerical experiments conducted by Held and Suarez (1994) to test different numerical cores of general circulation models reproduced a state of climate similar to the observed by simply prescribing the diabatic heating and friction as arithmetical expressions – the Held-Suarez benchmark. All physical parameterizations related to short- and long-wave radiation, turbulence, surface fluxes and convection, included in the terms F_U, F_V and F_Θ in eqs. (2.14), (2.15) and (2.17), were artificially substituted by a simple Newtonian cooling and Rayleigh friction.

This kind of simplification has been widely used by several studies (WILLIAMS, 2003; YAMAMOTO; TAKAHASHI, 2003; POTTER et al., 2014) and intends to isolate the main large scale dynamical process of the atmospheric general circulation without considering the complications of all physical processes together. The idealized treatment of Held-Suarez coupled with the ARW core set for a global domain without land-sea distribution, topography, diurnal and seasonal cycles was the basis of the numerical experiments performed in this study.

The mathematical expressions provided by Held and Suarez (1994) in isobaric coordinates, are given by,

$$\left(\frac{d\theta}{dt}\right)_{Diab} = -k_a(\phi,p)\left[\theta - \theta_{eq}(\phi,p)\right] \tag{2.21}$$

$$\left(\frac{d\vec{U}}{dt}\right)_{Fric} = -\,k_f(p)\vec{U} \tag{2.22}$$

where,

$$\theta_{eq}(\phi,p) = max\left\{200\,K, \left[315\,K - (\Delta T)_y\, sin^2\phi - (\Delta\theta)_z \ln\left(\frac{p}{p_0}\right) cos^2\phi\right]\left(\frac{p}{p_0}\right)^{\kappa}\right\} \tag{2.23}$$

$$k_a(\phi,p) = \frac{1}{\tau_a}\left[1 + 9\,max\left(0, \frac{\sigma - \sigma_b}{1 - \sigma_b}\right) cos^4\phi\right] \tag{2.24}$$

$$k_f(p) = \frac{1}{\tau_f}\, max\left(0, \frac{\sigma - \sigma_b}{1 - \sigma_b}\right) \tag{2.25}$$

Here $\sigma = p/p_0$ is the pressure-normalized level and, k_a, k_f and θ_{eq} are, respectively, the pressure, the thermal and dissipation coefficients and the forcing potential temperature equilibrium profile. The dimensional constants are $(\Delta T)_y$, the horizontal temperature contrasts, $(\Delta\theta)_z$ the vertical temperature contrast, p_0 the surface pressure, and σ_b is the level of the boundary layer, which were held constant in all our experiments.

The latitudinal cross-sections of forcing temperature profile, the thermal and frictional time scales as well as the parameter values used in the simulations are depicted in Figure 2.3. The temperature forcing (eq. 2.23) is intended to approximate an equilibrium profile of a zonally symmetric atmosphere in which only radiation and convection affect the thermal distribution (i.e. without dynamics). Temperatures decrease monotonically through the troposphere and the stratosphere is treated as an isothermal layer. Since there is no exchange between the atmosphere and the underlying surface, the Newtonian relaxation towards this forcing profile (eq. 2.21) has the effect of near-surface adiabatic heating, radiative cooling and convection in the free troposphere through spatial dependence of the thermal relaxation time (eq. 2.24, Figure 2.3). This relaxation time is 40 days above $\sigma_b = 0.7$ and becomes smaller toward the surface and the tropical region.

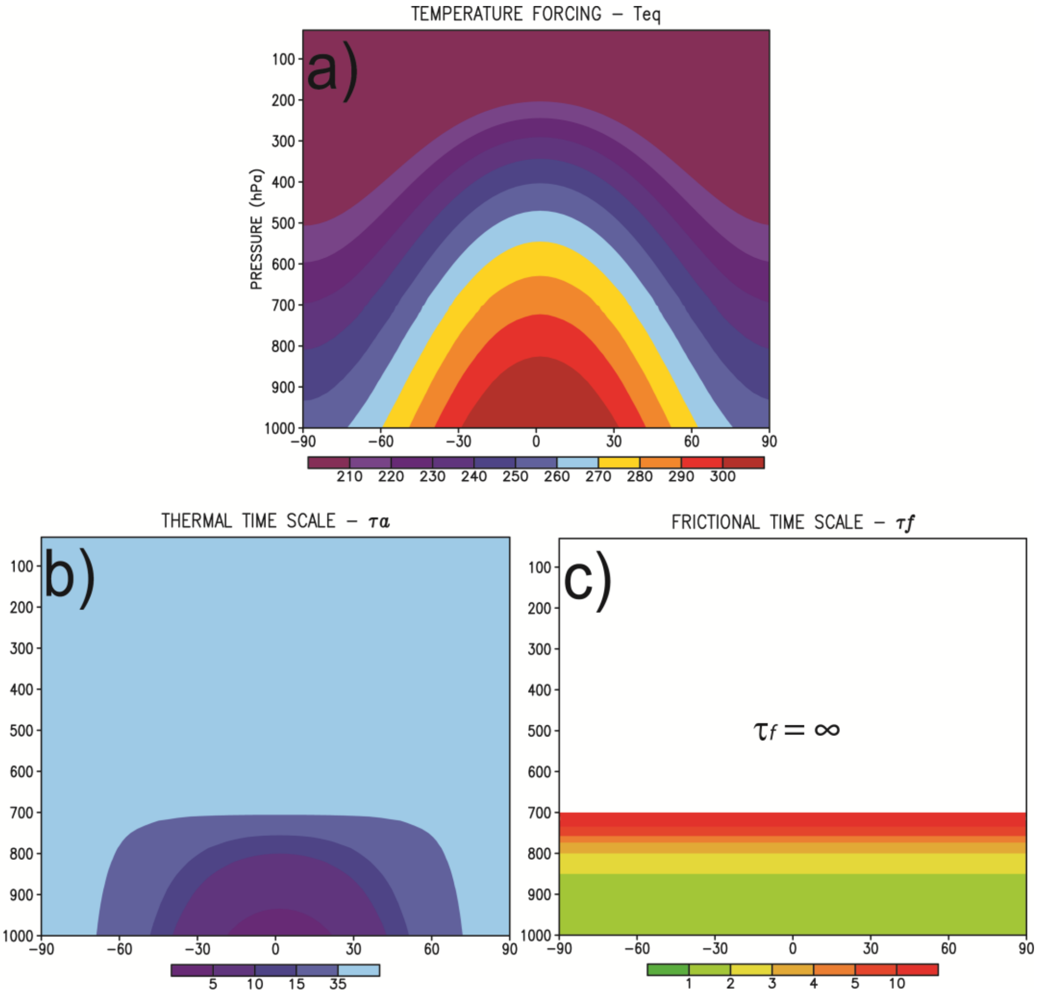

Figure 2.3 – Vertical cross section of the equilibrium temperature and the characteristic thermal and frictional time scales used in the Held-Suarez benchmark, which we use to force our model experiment. The values used for the constants in eqs. (2.21) – (2.25) are $(\Delta T)_y = 60K$, $(\Delta\theta)_z = 10K$, $p_0 = 1000\, hPa$, $\sigma_b = 0.7$, $\kappa = R/c_p = 2/7$, $\tau_a = 40\, days$ and $\tau_f = 1\, day$.

Rayleigh friction representing dissipation in the boundary layer (eqs. 2.22 and 2.25) is applied below $\sigma_b = 0.7$. The frictional time scales (Figure 2.3) ranges with height from 1 day at the near surface to infinity in the free atmosphere (which means that the friction has no role in this layer). No friction is applied above the level $\sigma_b = 0.7$ aside from a small artificial attenuation given by the 2D Smagorinsky first order closure (with the empirical constant c_s set 0.25, SMAGORINSKY, 1963) scheme and second order diffusion terms in order to avoid numerical instabilities.

2.3. Sensitivity experiments

Since it was hypothesized that the equatorial activity was responsible for triggering modes which would maintain the superrotating state, a proper simulation of equatorial waves is crucial to reproduce the phenomenon. In this section, sensitivity experiments were carried out in order to test the ability of the idealized model in reproducing equatorial waves. For that, the tropical atmosphere was forced by an anomalous axisymmetric heat source $\dot{Q}$ superimposed to the diabatic term of the Held-Suarez benchmark, such that eq. (2.21) became,

$$\left(\frac{d\theta}{dt}\right)_{Diab} = -k_a\left[\theta - \theta_{eq}\right] + \dot{Q} \tag{2.26}$$

Two different configurations for $\dot{Q}$, one based on Matsuno (1966) and another one based on Gill (1980), were adopted in eq. (2.26). Specific equatorial wave patterns were produced by these two authors by imposing heat (mass) sources with specific functional forms in the shallow water equations for the equatorial beta-plane. Although the ARW is a fully non-linear numerical core, the reproduction of these patterns would indicate that the model is able to reproduce equatorial waves. Neither physical parameterizations nor any numerical scheme from those used in the experiments of superrotation were modified in this sensitivity test.

Figure 2.4 presents the experiment similar to Matsuno (1966), in which a mass source and sink were placed about the equator. The author specified a wavenumber one sinusoidal-like forcing in the longitudinal direction with an exponential decaying toward higher latitudes. Here such a forcing was mimicked by a heat source with similar functional form,

$$\dot{Q} = \dot{Q}_0 \sin(n\lambda)\, exp\left[-\left(\frac{\phi - \phi_0}{\Delta\phi}\right)^2\right] sin\left(\pi\frac{\sigma - \sigma_T}{\sigma_B - \sigma_T}\right) \tag{2.27}$$

The first term on the right hand side of eq. (2.27) was constant during the whole integration. $\dot{Q}_0$ was set to 2 K day^{-1}, which is smaller than those values found in regions with high convective activity in the Earth's tropical atmosphere (10 – 15 K day^{-1}), but enough to not provide a strong "initial quick" in the atmosphere. The second term gives the axisymmetric structure with heating and cooling by setting $n = 1$; the third one confines the forcing in the tropical region with a Gaussian shape, centered in $\phi_0 = 0°$ and with meridional width $\Delta\phi = 15°$. In the vertical direction, the heating/cooling is provided by the last term, with stronger heating/cooling between $\sigma_T = 0.2$ and $\sigma_B = 0.8$.

The simulation test was run for 20 days, starting from a motionless atmosphere with no meridional temperature gradients $(\Delta T)_y$. Figure 2.4 shows the results obtained after 15 days of integration in 700 hPa and those obtained by Matsuno (1966). Both experiments show the formation of cyclonic and anticyclonic gyres at the equatorial region associated with the formation of wavenumber one Rossby waves. The maxima of heating and cooling at 120° E and 60° W, respectively, were coincident with the region of divergence and convergence (Figure 2.4b). As expected, the strong zonal flow associated with the wind circulation around these gyres was strongly trapped in the equatorial region.

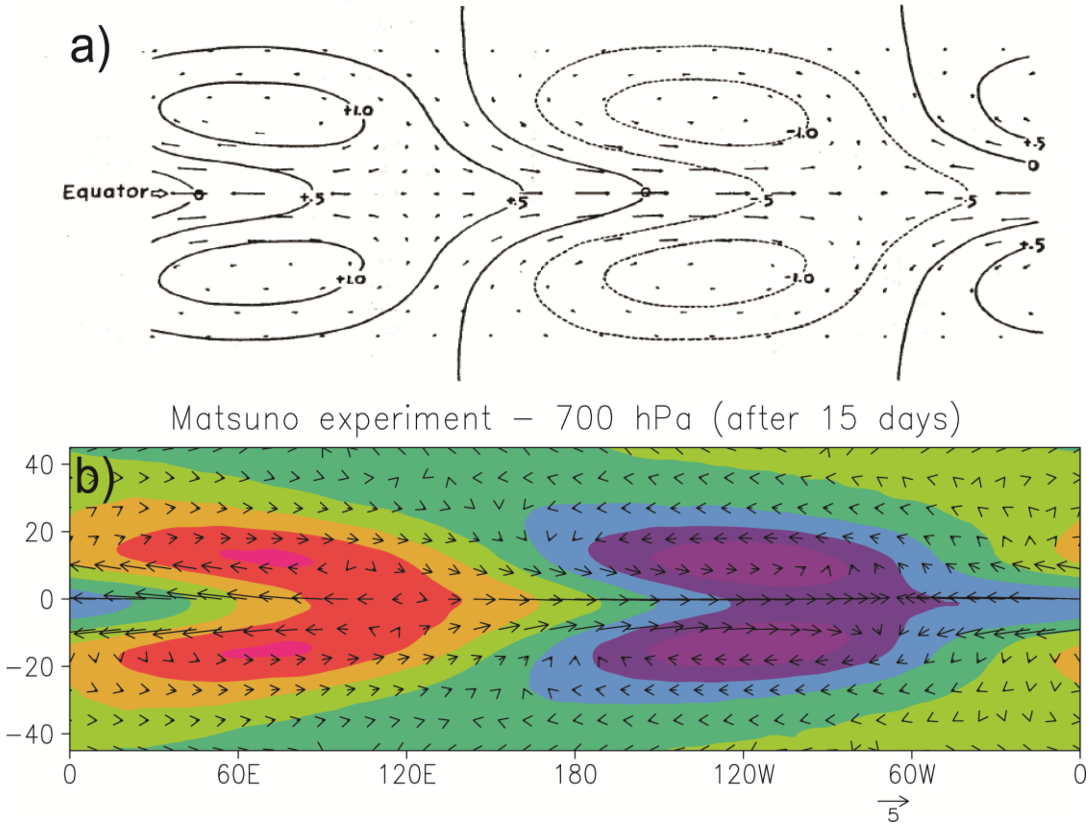

Matsuno experiment – 700 hPa (after 15 days)

Figure 2.4 – Geopotential and wind signatures associated with the experiment with the sinusoidal-like heat source placed at the equatorial atmosphere: a) Matsuno (1966) results, b) WRF results in 700 hPa, after 15 days of integration. Warmer colors are related to positive geopotential heights whereas colder color to negative ones.

In order to reproduce the Gill (1980) experiment, in which an isolated heat source is placed at the equator, a circular forcing was adopted. The longitudinal structure of eq. (2.27) was modified from a sinusoidal to a Gaussian form, centered at longitude $\lambda_0 = 180°$

with width $\Delta\lambda = 15°$, such that

$$\dot{Q} = \dot{Q}_0 exp\left[-\left(\frac{\lambda-\lambda_0}{\Delta\lambda}\right)^2\right] exp\left[-\left(\frac{\phi-\phi_0}{\Delta\phi}\right)^2\right] sin\left(\pi\frac{\sigma-\sigma_T}{\sigma_B-\sigma_T}\right) \tag{2.28}$$

Figure 2.5 shows the geopotential anomalies and winds in 700 hPa after 25 days of integration. The horizontal pattern was similar to the periodic forcing in the longitudinal direction, with a pair of troughs about the equator, although an asymmetry east from the heat source was observed. Instead of a single equatorial Rossby wave, a coupling between equatorial Rossby and Kelvin waves was obtained from an isolated source of heat.

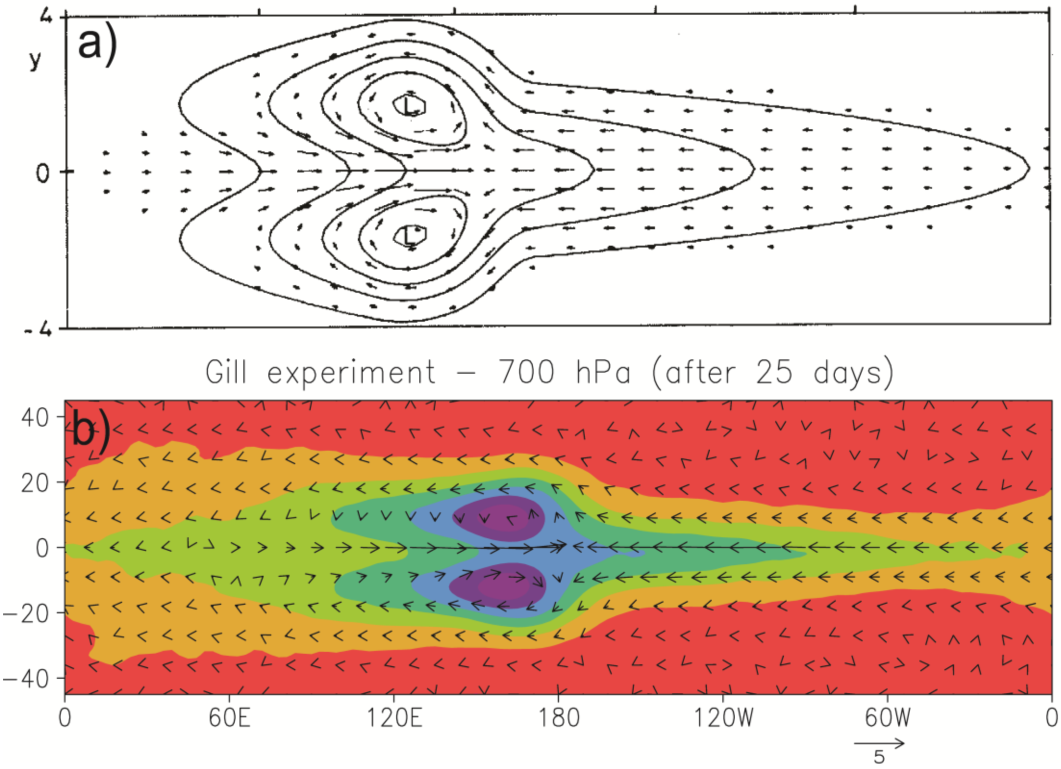

Figure 2.5 – Geopotential and wind signatures associated with the experiment with the isolated heat source placed at the equatorial atmosphere: a) Gill (1980) results, b) WRF results in 700 hPa, after 25 days of integration. Warmer colors are related to positive geopotential heights whereas colder color to negative ones.

In both numerical experiments depicted in Figures 2.4 and 2.5, the forcing was kept on during the whole period of integration. In order to test the idea of zonal propagation of equatorial waves, the heat source was turned off after day 25 and then the simulation was performed until day 30. The sequence shown in Figure 2.6 indicates that after the forcing was shut down there was a separation between the two modes: the faster Kelvin wave propagated eastward whereas the slower Rossby wave presented a small displacement westward. Although it was not shown here, there was an evident degradation of the modes 48 hours after the forcing was turned off due to the existent dissipation in the model. These results show that the WRF ARW core was able to reproduce the experiments of equatorial waves generation, and therefore it was appropriate for the study.

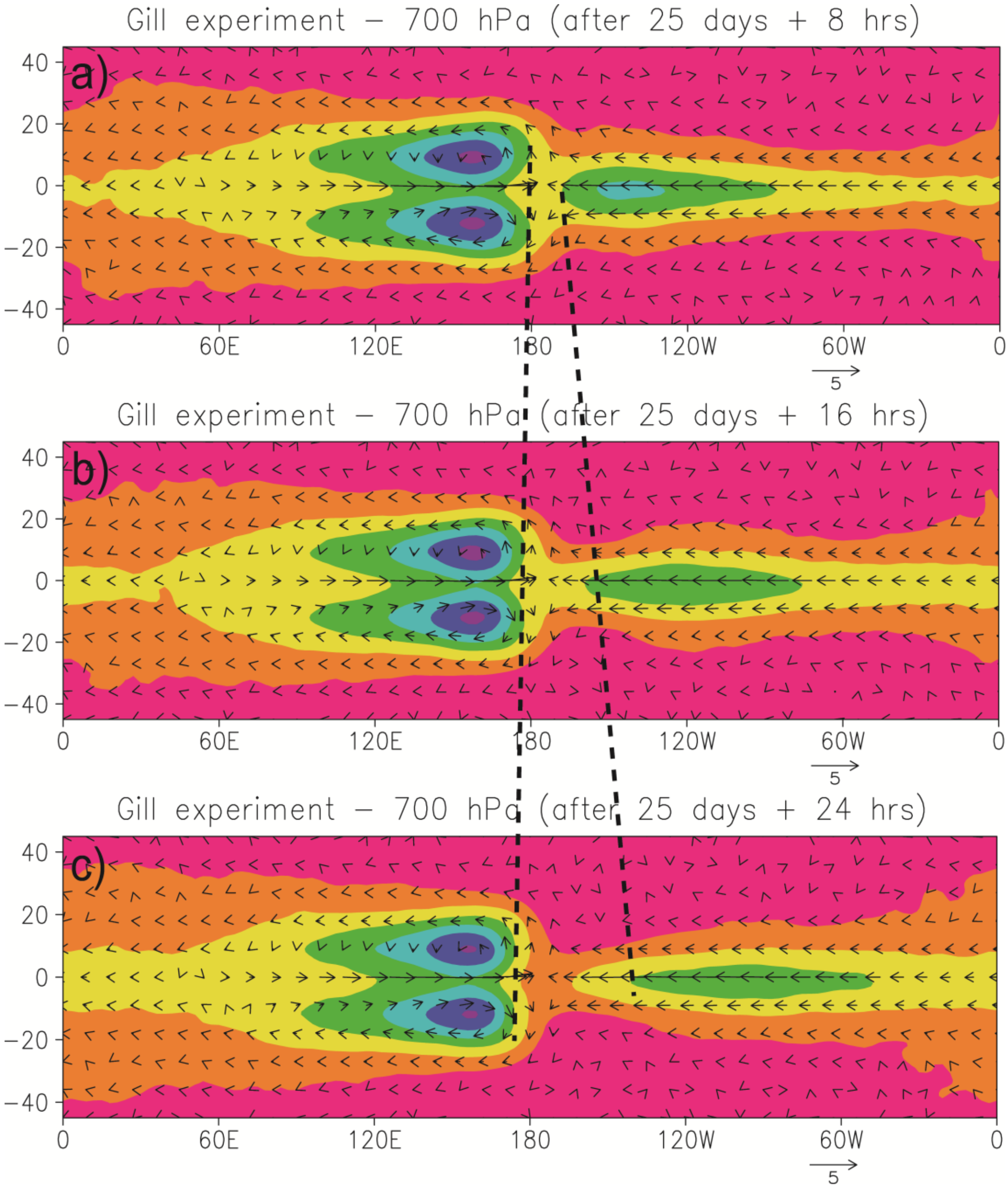

Gill experiment – 700 hPa (after 25 days + 8 hrs)

Gill experiment – 700 hPa (after 25 days + 16 hrs)

Gill experiment – 700 hPa (after 25 days + 24 hrs)

Figure 2.6 – Propagation of Equatorial Rossby and Kelvin waves after the heat source was turned off on day 25: a) 8 hrs later, b) 16 hrs later and c) 24 hrs later. Dashed line denotes the sense of propagation of the modes.

CHAPTER 3.

Results – Part I

Atmospheric superrotation in an idealized GCM: parameter dependence of the eddy response

Idealized Earth-like general circulation models (GCMs) have been extensively used to study superrotation on so-called "slowly rotating" bodies like Venus and Titan, however they tend to have difficulty producing superrotation if only the rotation rate is reduced to Titan- or Venus-like values. The Rossby number, $Ro = U/2\Omega L$, which characterizes the influence of rotation on the circulation, is small for Earth but large for both Venus and Titan. However, the differences in other non-dimensional control parameters are often ignored in idealized planetary circulation studies. In this first part, a simplified Earth-like GCM is used to demonstrate the importance of the other non-dimensional parameters in obtaining a superrotating flow, and to identify the wave-modes responsible for generating and maintaining superrotation. It is shown that superrotation only emerges on a planet of slow rotation rate if the atmospheric thermal inertia is simultaneously increased; alternatively, superrotation is obtained if the only planetary radius is reduced. When only the rotation rate is reduced, a nearly axisymmetric circulation with intense Hadley cells is produced preventing strong and persistent winds over the equator. The mechanism for generating and maintaining superrotation in the model involves a coupling between equatorial and high-latitude waves. However, during the short period of spin-up the generation involves equatorial Kelvin-like waves, whereas at the steady-state maintenance involves equatorial Rossby-like waves.

3.1. Theoretical background

Nondimensional variables involving typical values of velocities, length, diffusivity, density, viscosity and rotation rate, play a key role in characterizing many dynamical aspects of the fluid. Among them, the Rossby number (Ro) is one of the most important parameters in geophysical fluid mechanics to characterize dynamical properties of the flow. Defined as

$$R_O = U/2\Omega L \quad (3.1)$$

where U, 2Ω and L are typical magnitudes of zonal wind, planetary rotation and flow length scales, it relates the ratio of advection to Coriolis force for a given flow of a rotating fluid or a large scale atmospheric motion (HOLTON, 2004; VALLIS, 2006). The geostrophic approximation holds for small values of Ro, as is the case for Earth's mid and high latitudes.

The terrestrial bodies in the solar system with substantial atmospheres, Earth, Mars, Venus and Saturn's moon Titan, present two distinct regimes of atmospheric circulation. Figure 3.1 shows that at global scales, Ro << 1 for Earth and Mars while Ro > 1 for Venus and Titan. The mean zonal structures of these atmospheres roughly exhibit two different regimes, which are defined as the classic and superrotating, and they are described in more detail in the next paragraphs.

Earth and Mars are fast rotating and large terrestrial bodies, which gives them rather small global values of Ro ~ 0.01. In this regime, there are substantial differences between the circulation in low and high latitudes. At low latitudes, the meridional circulation is characterized by upward motion of relatively warm air at the equator and sinking of cold air at subtropical latitudes along the latitudinal plane, which develops prograde zonal flow, on the poleward edge of each tropical overturning circulation, or Hadley cell (Figure 3.1). At higher latitudes, on the other hand, the flow is dominated by large scale eddies which arise from baroclinic instability (HOLTON, 2004; VALLIS, 2006). Seasonal cycles complicate this picture somewhat, and their effects will not be considered here.

Since the rotation rates of Venus and Titan are slower compared to Earth and Mars' (the rotation period is about 16 days for Titan and around 240 days for Venus), numerical studies often focus on Earth-like atmospheres under slow rotation (DEL GENIO; SUOZZO, 1987; WILLIAMS, 1988a,b,; DEL GENIO et al., 1993; NAVARRA; BOCCALETTI, 2002; WILLIAMS, 2003; WALKER; SCHNEIDER, 2006). In parallel, simulations using numerical models set for either simplified or fully parameterized physical processes (as for example, turbulent dissipation at the boundary layer, radiative transfer, chemical reactions and aerosols) of Venus (YAMAMOTO; TAKAHASHI, 2003; LEE et al., 2005; LEE et al., 2007; HOLLINGSWORTH et al., 2007; LEBONNOIS et al., 2010; PARISH et al., 2011) and Titan (HOURDIN et al., 1995; TOKANO et al., 1999; TOKANO, 2007; RICHARDSON et al., 2007; FRIEDSON et al., 2009; NEWMAN et al, 2011; MITCHELL et al. 2011, 2012; LEBONNOIS et al., 2012) have been performed in order to gain a more complete and accurate view of the general circulation patterns (and their time dependence) for each body. A common feature of all these studies is that the Hadley cell is larger in meridional extent (Figure 3.1) and poleward heat fluxes efficiently act to reduce the latitudinal contrast of the temperature. Since the Rossby deformation radius is proportional to Ω^{-1} (EADY, 1949; VALLIS, 2006), baroclinic instability weakens in this regime of higher Rossby numbers due to the fact that the typical unstable wavelength no longer fits on the planet (WILLIAMS, 1988a,b; NAVARRA; BOCCALETTI, 2002). Due to the large obliquity of Titan (around 26.7° to the ecliptic) the Hadley cell is also expected to have strong seasonal variation changing from a situation depicted on Figure 3.1, with a symmetric pair of overturning circulation at the equator during the equinox, to a single inter-hemispheric Hadley cell. Structural changes regarding to the mean overturning circulation from an Earth to a higher *R*o regime are common to the modeling studies.

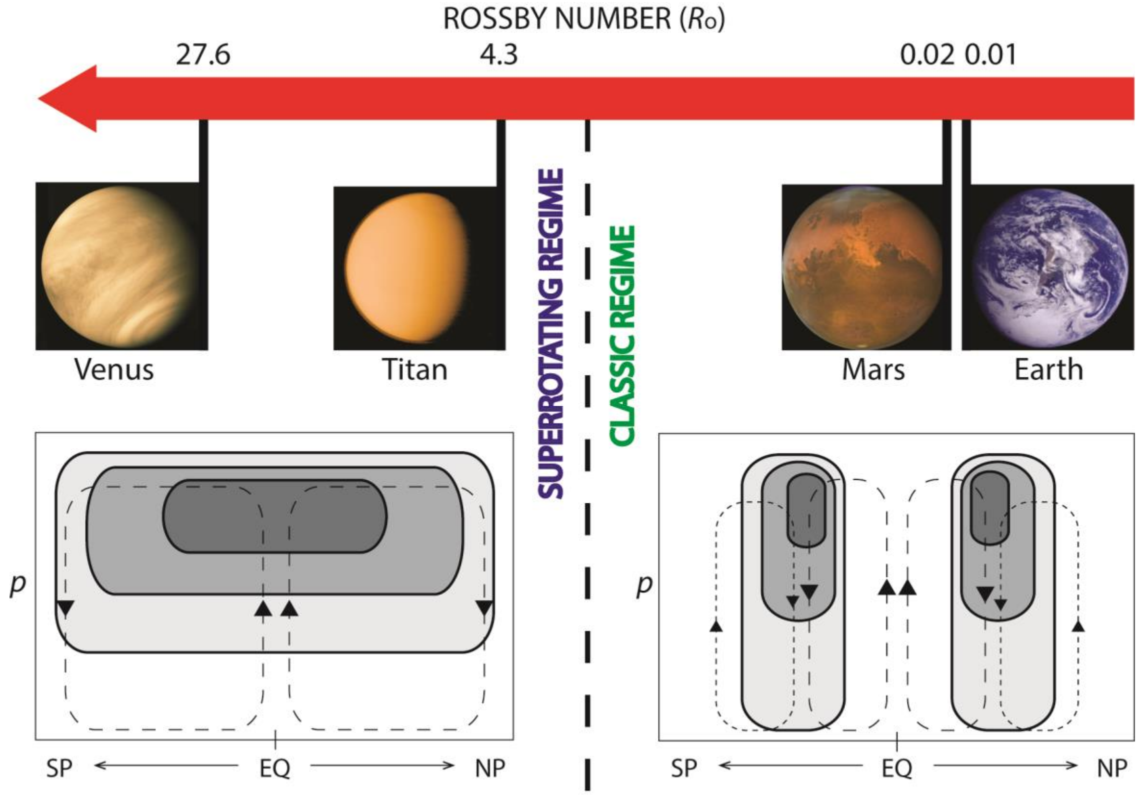

Figure 3.1. Schematic view of the different Rossby numbers (*R*o) and circulation regimes found on the terrestrial bodies of the solar system with substantial atmospheres. *R*o was computed based on typical scales of zonal winds (around 100 m s^{-1} for Venus and Titan and 10 m s^{-1} for Earth and Mars), rotation rate, and planetary radius. The lower panels depicts a hypothetical vertical cross section of zonal mean zonal wind (shaded, arbitrary scale) and mean overturning circulation (dashed lines, arbitrary scales) characteristic of each body's atmospheres. See text for more details. (Photo credits: NASA/JPL).

However, few models today are able to reproduce the full strength of the zonal wind distribution on Venus and Titan. Both in situ and indirect observation from each body (for example BOUGHER et al. 1997; KOSTIUK et al., 2001; BIRD et al., 2005; WIDEMANN et al., 2008) have shown strong zonal flow with magnitude of 100 m s^{-1} at the upper level being the dominant component of the atmospheric circulation even at the equator. Such strong zonal winds of Venus and Titan's equatorial atmospheres are in, so-called, superrotation. Some models produce only weak superrotation with zonal winds of 2 – 60 m s^{-1} at the equator (e.g., TOKANO et al., 1999; LEE et al., 2007; RICHARDSON et al., 2007; FRIEDSON et al., 2008; LEBONNOIS et al., 2010) while others produce stronger equatorial winds (HOURDIN et al., 1995; YAMAMOTO; TAKAHASHI, 2003; NEWMAN et al., 2011; LEBONNOIS et al., 2012) more in-line with observations (KOSTIUK et al., 2001; WIDEMANN et al., 2008;, for example). This discrepancy among similar models has yet to be understood, making the study of superrotating flow a challenging subject in geophysical fluid dynamics.

Through eq. (3.1), a larger Ro (for the same wind typical scale U) could be achieved by either slowing the rotation rate of the planet down or decreasing the typical horizontal length scale on which the winds occur. When Earth-like models are run at slower rotation rates, they tend to produce strong jets at higher latitudes but also tend to fail in reproducing superrotating flow over the equator (see for example in WILLIAMs 1988a; NAVARRA; BOCCALLETI, 2002). Mitchell and Vallis (2010) changed the Rossby number by decreasing the planetary radius in an idealized Earth-like model, and showed that in the cases with $Ro > 1$, the dynamics adjusted itself in such way that superrotation was produced. Therefore different outcomes can be obtained in simplified models when either the rotation rate or the planetary radius is reduced. This study aims to identify how these differences are obtained in a simplified Earth-like GCM by describing the momentum balance achieved when changing rotation rate versus planetary radius. A key goal is to identify the wave modes that maintain the superrotation at the equator in the steady state. The study is organized as follows: section 3.2 describes the theoretical framework and the design of the numerical experiments, section 3.3 presents the momentum budgets and eddy diagnostics of the experiments and the partial conclusions are given in section 3.4.

3.2. Methodology

3.2.1. Dimensionless governing equations and control parameters

In the simplified modeling framework, the three-dimensional flow is described by the horizontal momentum and thermodynamics equations in which the diabatic and frictional effects are given by a linear Rayleigh friction and Newtonian cooling

$$\frac{\partial \vec{u}}{\partial t} + (\vec{V} \cdot \nabla)\vec{u} + \vec{f} \times \vec{u} = -\nabla\Phi - \frac{\vec{u}}{\tau_f} \tag{3.2}$$

$$\frac{\partial \theta}{\partial t} + (\vec{V} \cdot \nabla)\theta = -\frac{(\theta - \theta_{eq})}{\tau_a} \tag{3.3}$$

where, $\vec{u} = u\,\vec{\imath} + v\vec{\jmath}$ and $\vec{V} = u\,\vec{\imath} + v\vec{\jmath} + \omega\vec{k}$ are, respectively, the two-dimensional and three-dimensional wind fields in pressure vertical coordinates and ω is the vertical pressure velocity in this coordinate; $f = 2\Omega sin\phi$ is the Coriolis parameter; Φ is the geopotential, and τ_f and τ_a are the characteristic frictional and thermal damping time scales of the simplified parameterizations. By traditional scaling arguments, these equations can be written in terms of nondimensional variables and parameters, indicated by the "hats" (see sections 2.12.1 and 5.1 of VALLIS, 2006) as:

$$\frac{\partial \hat{\vec{u}}}{\partial \hat{t}} + R_O\left(\hat{\vec{V}} \cdot \nabla\right)\hat{\vec{u}} + \hat{\vec{f}} \times \hat{\vec{u}} = -\nabla\hat{\Phi} - E_K\hat{\vec{u}} \tag{3.4}$$

$$\frac{\partial \hat{\theta}}{\partial \hat{t}} + R_O\left(\hat{\vec{V}} \cdot \nabla\right)\hat{\theta} = -\frac{(\hat{\theta} - \hat{\theta}_{eq})}{\hat{\tau}_a} \tag{3.5}$$

In eqs. (3.4) and (3.5), $R_O = U/2\Omega L$ represents the Rossby number, $E_K = 1/2\Omega\tau_f$ the Ekman number and $\hat{\tau}_a = 2\Omega\tau_a$ a thermal damping number. These three nondimensional parameters describe both dynamical and thermal properties of the flow, and therefore govern the behavior of the system once the obtained circulation can be seen as a combination of values of these different nondimensional parameters. For instance, the Ekman number governs the magnitude of friction in the boundary layer whereas the thermal number governs the thermal inertia of the atmosphere.

3.2.2. Numerical experiments

With the goal of understanding the influence of increasing the Rossby number, it was devised a set of numerical experiments intended to highlight its importance relative to the other non-dimensional numbers by either decreasing the rotation rate or the planetary radius. With a characteristic length scale given by the planetary radius a the measure of the local Rossby number is defined as

$$R_O = \frac{U}{2\Omega sin\phi \; acos\phi} \qquad (3.6)$$

Two sets of numerical experiments were run: in the first one named a^* (= a/a_{earth}), the radius is varied from Earth's to values 20 times smaller, which roughly corresponds to the radius of 280 km used in the superrotating experiment by Mitchell and Vallis (2010). In the second experiment, referred to Ω^* (= $\Omega/\Omega_{\text{earth}}$), the rotation rate was reduced by the same factor, from Earth's values to values 20 times smaller. The values of the constants and nondimensional numbers for the whole set of numerical experiments are given in Table 3.1.

Table 3.1. Values of rotation rate, planetary radius, thermal and frictional time scales and, the nondimensional numbers used in the numerical experiments.

Experiment	Ω (x10^{-5} s^{-1})	a (x10^{6} m)	τ_a (days)	τ_f (days)	Ro	Ek	τ_a
$\Omega^* = 1$	7.292	6.371	40	1	0.04	0.08	500
$a^* = 1/20$	7.292	0.319	40	1	1.30	0.08	500
$\Omega^* = 1/20$	0.365	6.371	40	1	0.80	1.60	25
$\Omega^* = 1/20$ wkhd	0.365	6.371	800	1	1.20	1.60	500
$\Omega^* = 1/20$ mod	0.365	6.371	800	20	1.30	0.08	500

The simulations were initiated from an isothermal and motionless atmosphere and run with 32 vertical levels and 3.0° x 3.0° horizontal grid spacing. In order to integrate the model for equivalent dynamical/inertial times, the numerical experiments were run for 10 years, or 3,650 days for simulations with Earth's rotation rate and 73,000 days for those with $\Omega^* = 1/20$. The data output were given at each 3 files per day. Unless otherwise stated, the results presented here are averaged over the last year of each experiment at the statistically steady phase. Figure 3.2 shows the total kinetic energy at the equilibrium for all experiments during this final year of the simulations indicating the steady state.

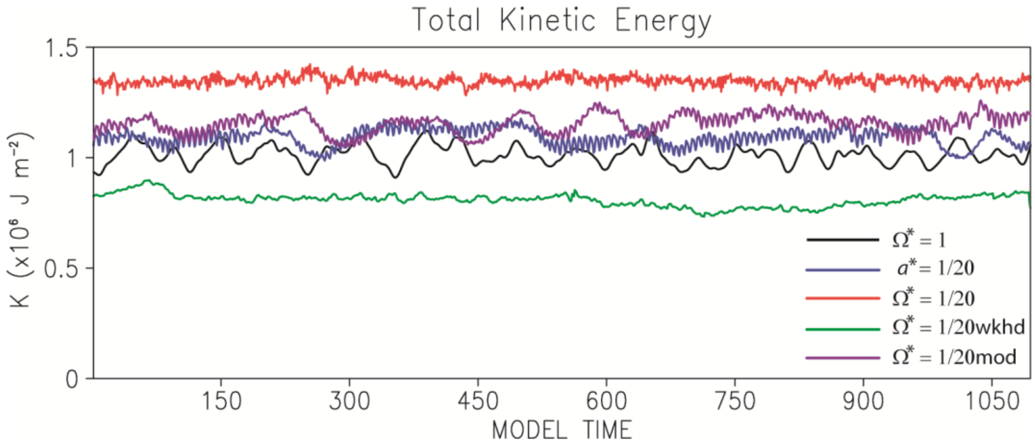

Figure 3.2. Vertically-integrated total kinetic energy (x10^6 J m^{-2}) during the last year of the simulations for each experiment. Apart from small oscillations the kinetic energy is constant, indicating a steady state has been achieved.

3.3. Results

3.3.1. Circulation regimes at low and high Rossby numbers

Figure 3.3 depicts the vertical cross section of time- and zonal-mean zonal winds, temperature and overturning mass flux, which is expressed by a stream function $\psi = 2\pi a cos\phi \int_{p_0}^{p}[\bar{v}]\, dp/g$. In the Earth-like regime (Figures 3.3a and 3.3b) the model reproduces the main features of the general circulation, being dominated by two westerly (prograde) subtropical jets in mid-latidudes (peak of 30 m s^{-1} centered about 40° at 200 hPa), and the weaker near-surface easterlies in the equatorial region. The baroclinic thermal structure given by the temperature gradients at mid- and high-latitudes is also reproduced, as well as the overturning circulation of the Hadley cells in the tropics and the Ferrell cells at high latitudes. The Hadley cell is a two-dimensional, axisymmetric overturning. In reality, there can be zonal asymmetric circulation created by land-sea distribution (Walker cell) and topography. However since these two forcing features are absent in the model configuration, the overturning circulation can be purely expressed by the axisymmetric structure given by Figure 3.3b.

In the Ω^* = 1/20 experiment, the circulation is in a higher *R*o regime, and the subtropical jets shift to high latitudes and become stronger (Figure 3.3c). The Hadley cell is both wider in latitude and stronger (with peak of 500x10^9 kg s^{-1}), which in turn decreases the temperature contrasts in its range of influence, as can be observed in Figure 3.3d. The latitudinal expansion of the Hadley cell shifts the subtropical jets and baroclinic zones poleward, thus promoting high-latitude jet formation. These features have been noted by other studies of circulation under slow rotation rates (HUNT, 1979; WILLIAMS; HOLLOWAY, 1982; WILLIAMS, 1988a,b; NAVARRA; BOCCALETTI, 2002; WALKER; SCHINEIDER, 2006). A general conclusion is the latitudinal extension of the mean meridional circulation increases with smaller rotation rate, transporting heat further poleward and decreasing the latitudinal thermal gradients over much of the globe. However, a significant baroclinic zone remains poleward of 60º N/S latitudes. The poleward shift of the jets may be partly understood from an axisymmetric and nearly inviscid perspective, in which the latitude of a jet maximum should increase as the Rossby number increases (HELD; HOU, 1980; MITCHELL; VALLIS, 2010). In this experiment, the tropospheric zonal circulation is dominated by two strong jets, and there is no occurrence of westerly, superrotating winds at the equator. In the narrow baroclinic zone around the latitudes of 80º - 90º N/S, a weaker Ferrell cell (two orders of magnitude weaker than the Hadley cell) is observed in each hemisphere (Figure 3.3d).

However, another pattern of winds emerges when the planetary radius is reduced in experiment $a^* = 1/20$. The flow is predominantly prograde (westerly) in much of the atmosphere, except at the lower levels and latitudes where they are easterly (Figure 3.3e and 3.3f). A single jet is located in the equatorial region (around 25-30 ms^{-1}), which is characteristic of a strongly superrotating state. The latitudinal extension of the mean meridional circulation (about 60° of width) did not vary considerably between the two experiments $a^* = 1/20$ and $\Omega^* = 1/20$, whereas its strength is more than three orders of magnitude less (peak of 1.2×10^9 kg s^{-1}) than the $\Omega^* = 1/20$ experiment. In the higher latitudes a weak Ferrell cell is observed even though the mean thermal state has a more barotropic configuration. Apart from small differences in intensity, the superrotating zonal wind pattern in this configuration is in agreement with the experiments described in Mitchell and Vallis (2010) in which the transition to the superrotation was observed for Rossby number bigger than 1.0 (see their $R_{OT} = 10.5$ simulation).

Although the two experiments described here have similar values of R_o, the rotation rate experiment does not transition to a superrotating state. Del Genio and Suozzo (1987), Del Genio et al. (1993) and others noticed that many Earth-based models fail to produce superrotation if run in a slower rotation configuration, but they follow the general behavior (barotropic thermal structure, wider Hadley cells) as described above. Since in the two simulations, one succeeded and one failed to produce a superrotating zonal jet at the equator, it is important to analyze how the winds at the equator are maintained in a time- and zonal-mean framework. In the following section, the components of the circulation (mean meridional circulation and transient eddies) that are responsible for convergence and divergence of momentum at the equator will be diagnosed in both non-superrotating and superrotating states.

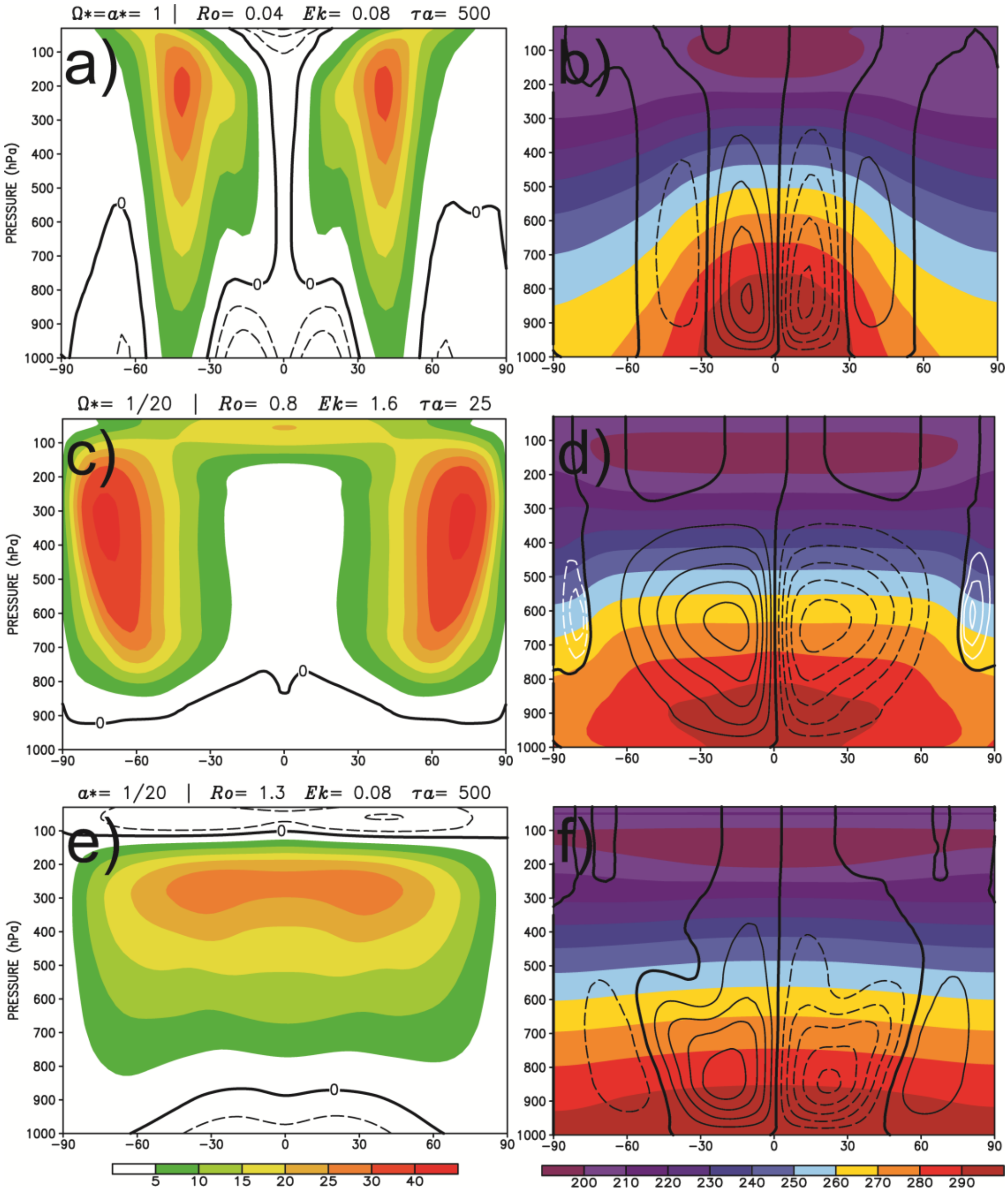

Figure 3.3. Vertical cross-sections of the time- and zonal-mean variables. The left panels are the zonal wind component (westerly winds in shaded; easterlies in dashed line with contour each 3 m s^{-1}). The right panels are temperature (shaded, K) and stream function ψ (contour, kg s^{-1}). a) and b) Experiment control, Earth-like case (ψ contours each 20×10^9 kg s^{-1}); c) and d) Experiment $\Omega^* = 1/20$ (ψ black contours each 100×10^9 kg s^{-1}, white contours each 3×10^9 kg s^{-1}); e) and f) Experiment $a^* = 1/20$ (ψ contours each 0.3×10^9 kg s^{-1}). The nondimensional parameters were computed based on the values in Table 1 and Figure 3.5 (see text for more details).

3.3.2. Mean convergence of momentum and net accelerations in the steady state

The time- and zonal-mean zonal momentum equation written in a flux form is given by:

$$\begin{aligned}&\frac{\partial[\bar{u}]}{\partial t}+\frac{1}{a\cos\phi}\frac{\partial}{\partial\phi}(\cos\phi\,[\overline{uv}])+\frac{\partial}{\partial p}[\overline{u\omega}]-2\Omega\sin\phi\,[\bar{v}]+\frac{2\Omega\cos\phi\,[\bar{\omega}]}{\rho g}\\&-\frac{tan\phi}{a}[\overline{uv}]\;+\frac{[\overline{u\omega}]}{a\rho g}=[\bar{F}_x]\end{aligned} \tag{3.7}$$

where u, v and ω are the wind components, ϕ is the latitude, a the planetary radius, p pressure and F_x the frictional processes. According to Lorenz (1967) the transport of momentum in the atmosphere can be decomposed in three components related to the mean meridional circulation, transient and stationary eddies. Based on the notation of Peixoto and Oort (1992), both meridional and vertical momentum fluxes can be written as a sum of these components:

$$\begin{aligned}[\overline{uv}]&=[\bar{u}][\bar{v}]+\overline{[u'v']}+[\bar{u}^*\bar{v}^*]\\ [\overline{u\omega}]&=[\bar{u}][\bar{\omega}]+\overline{[u'\omega']}+[\bar{u}^*\bar{\omega}^*]\end{aligned} \tag{3.8}$$

where bar denotes average in time, brackets the zonal mean; their departures are given, respectively, by the prime and starred terms . Since stationary forcings are absent in the model (i.e., the Held-Suarez benchmark is axisymmetric, see Chapter 2) starred terms are absent. Since $\frac{[\overline{u\omega}]}{a\rho g}$ and $\frac{2\Omega\cos\phi[\bar{\omega}]}{\rho g}$ terms are too small compared to the others, eq. (3.7) can be written as:

$$\begin{aligned}\frac{\partial[\bar{u}]}{\partial t}=&-\frac{1}{a\,\cos\phi}\frac{\partial}{\partial\phi}(\cos\phi\,[\bar{u}][\bar{v}])+2\Omega sin\phi[\bar{v}]-\frac{\partial}{\partial p}[\bar{u}][\bar{\omega}]+\frac{tan\phi}{a}[\bar{u}][\bar{v}]\\&-\frac{1}{a\,\cos\phi}\frac{\partial}{\partial\phi}\left(\cos\phi\,\overline{[u'v']}\right)+\frac{tan\phi}{a}\overline{[u'v']}-\frac{\partial}{\partial p}\overline{[u'\omega']}\;+[\bar{F}_x]\end{aligned} \tag{3.9}$$

Eq. (3.9) establishes that the net acceleration (deceleration) of the time- and zonal-mean zonal winds are due to the combination of the convergence (divergence) of the momentum transport by the mean meridional cells and transient eddies, the Coriolis and the metric terms. The momentum balance postulated in the Gierasch-Rossow-Williams mechanism, as an attempt to understand how superrotation is maintained (GRW, GIERASCH, 1975; ROSSOW; WILLIAMS, 1979), involves the transport by the overturning circulation ($[\bar{u}][\bar{v}]$ and $[\bar{u}][\bar{\omega}]$), and that of non-axisymmetric disturbances ($\overline{[u'v']}$ and $\overline{[u'\omega']}$) generated by the instabilities of a barotropically unstable high latitude jet (ROSSOW; WILLIAMS, 1979; HOURDIN et al., 1995; WILLIAMS, 2003; LUZ; HOURDIN, 2003). For the present analysis, the terms related to the cell transports (including the Coriolis and metric terms) are summed together to account for the combined effects of the overturning circulations.

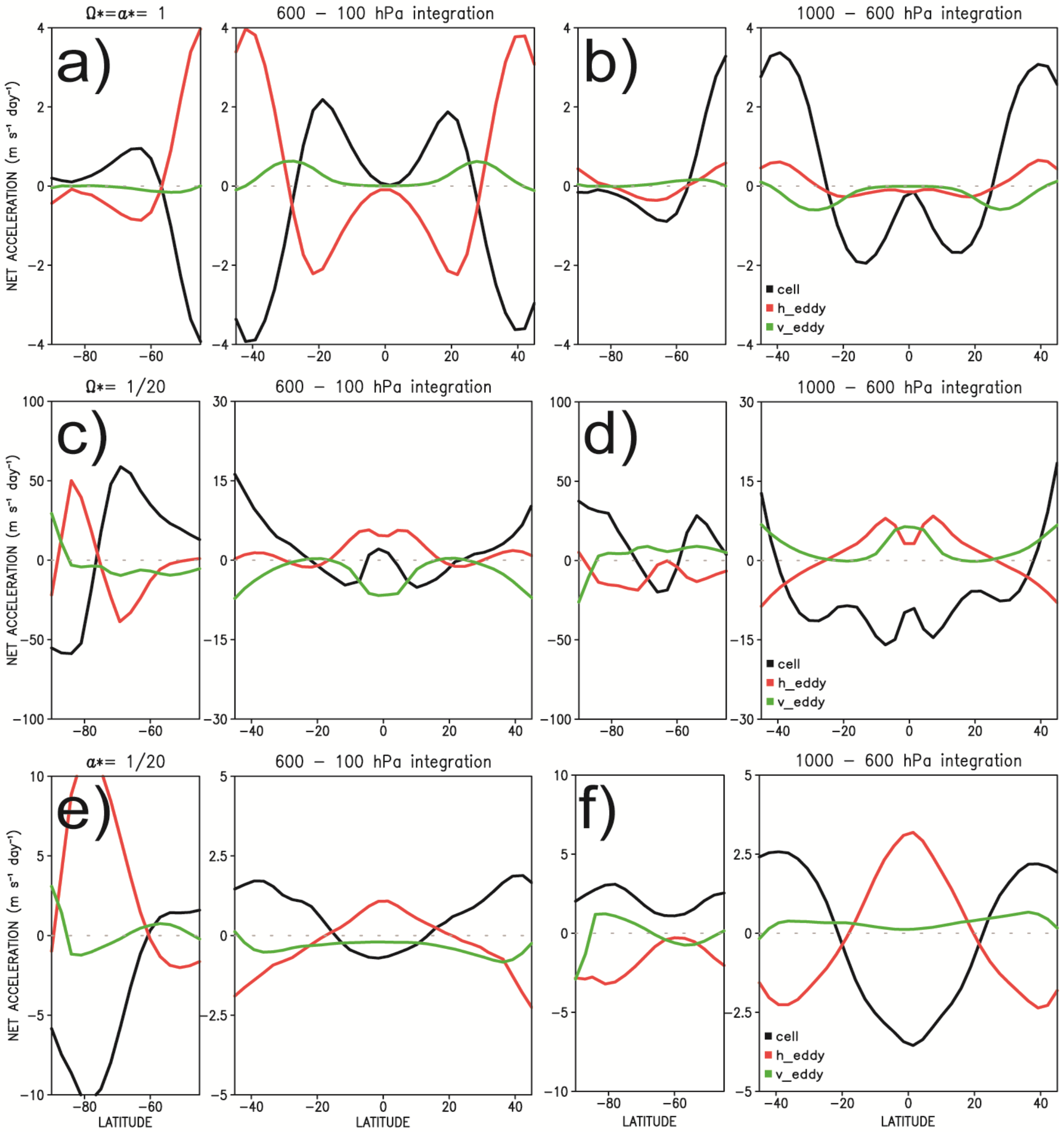

Figure 3.4. Vertically integrated net acceleration (in m s^{-1} day^{-1}) caused by the cells and the horizontal and vertical convergence of momentum by eddies: a) and b) for the Earth-like case experiment $\Omega^*= a^*= 1$; c) and d) for the $\Omega^*= 1/20$ experiment and, e) and f) for the $a^*= 1/20$ experiment. All the terms are integrated in the vertical in two layers: 1000 – 600 hPa and 100 – 600 hPa, and weighted by the atmospheric mass of the respective layer. Black lines indicate the terms related to the cells, red lines shows the eddy terms acting in the horizontal and the green lines, the eddy terms acting in the vertical.

Figure 3.4 depicts the mass-weighted vertical integral of net acceleration/deceleration of the zonal wind. The combined effects of the cells and transient eddies are divided in two vertical layers: 1000 – 600 hPa where the effects of the frictional boundary layer of the model are important, and 600 – 100 hPa for the free troposphere. All terms are weighted by the atmospheric mass of the vertical layer, $A_{p0}^{p} = \int_{p0}^{p} A dp / \int_{p0}^{p} dp$, with a generic variable A, and bottom and top level pressures p_0 and p. Since the magnitudes of the accelerations in mid- and high-latitudes and near the equator are different, they are displayed separately on different scales. For reasons of symmetry only the higher latitudes (above 45° S) of the Southern Hemisphere are shown.

In an Earth-like scenario the upper branch of the Hadley cell carries westerly momentum poleward from the equatorial region into the subtropics, thus accelerating the flow there (Figure 3.4a). Westerly momentum is transported by eddies and converges in midlatitudes in order to maintain the jets in these regions (see PEIXOTO; OORT, 1992; SCHNEIDER, 2006). The low-level equatorward branch of the Hadley cell carries easterly momentum toward the equator (Figure 3.4b). Due to instabilities in the jet regions, Rossby waves are produced and they propagate toward the subtropics and high latitudes, decelerating the flow (see VALLIS, 2006; RANDEL; HELD, 1991). These effects are strongest in the upper layer.

In the a*, Ω*= 1/20 cases with higher Rossby numbers, the contrasting zonal mean wind structures (Figures 3.3c and 3.3e) between the experiments are reflected in different eddy and cell transports. For the slow-rotating experiment Ω*= 1/20, the cell term promotes strong acceleration of the zonal mean jets in the upper layer (i.e. the free troposphere of the model; Figures 3.4c and 3.3c). Since in this regime the Hadley circulation is wider (Figure 3.3d) these effects extend toward higher latitudes than in the Earth-like experiment. At polar latitudes where strong shear is present (Figure 3.3c), a Ferrel cell offsets eddy transports in a similar manner to the mid-latitudes in the Earth-like case. In the lower levels near the equator, small accelerations generated by the horizontal and vertical transport by eddies oppose the deceleration created by the low-level branch of the overturning circulation (Figure 3.4d). In the upper layers, vertical transport by eddies decelerate equatorial winds while horizontal eddy transport accelerates them (Figure 3.4c).

For the smaller planetary radius experiment a*= 1/20, the cell decelerates the flow at the equator and accelerates it in mid- and subtropical latitudes in upper levels, though the values are two orders of magnitude smaller than in the previous experiment (Figures 3.3e and 3.3d). At very high latitudes, where strong shear is present, the transport provided by the indirect Ferrell cell (Figure 3.3f) acts also to decelerate the flow. In contrast to the previous case, here the vertical transport by eddies has relatively little influence on the momentum balance at the equator, and instead there is a balance between horizontal eddy transport accelerating (decelerating) the equator (subtropics) and the Hadley cell decelerating (accelerating) the equator (subtropics) at all levels. In this superrotating configuration (in steady state), the eddies transport more momentum where friction is present to sustain westerly flow against friction. In upper levels where the superrotation is well established, less is required from eddies to maintain the flow against the weak Hadley cell (see SARAVANAN, 1993; MITCHELL; VALLIS, 2010).

The analysis shows that high value of Rossby number can yield two completely different states. While in the slow-rotating experiment there is the predominance of a strong jet in high latitudes, decreasing the radius instead produces intense and persistent westerly winds at the equator. The next section explores the origin of these differences based on the influence of other nondimensional parameters.

3.3.3. The influence of the rotation rate on the parametric regime

Estimates of the nondimensional numbers determined through the relations in the eqs. (3.4) and (3.5) are shown in Table 1 and the top of Figures 3.3a – 3.3f. The local Rossby number Ro (eq. 3.6) is shown in Figure 3.5 for the three simulations. A mean value was obtained by averaging in a layer between 200 – 400 hPa (i.e. at the jet levels) from |80°| to |10°| of latitude. Both $\Omega^*= 1/20$ and $a^*= 1/20$ simulations have a mean local Rossby number about two orders of magnitude larger than that of the Earth-like regime (0.04, see Figures 3.3 and 3.5). Large Ro indicates that the nonlinear acceleration in the advective terms (eq. 3) has comparable magnitude to the other terms, and thus, it cannot be neglected. When this happens the regime is no longer geostrophic and the cyclostrophic term becomes important.

Besides the change in the Rossby number, other very important changes occur in the thermal and Ekman numbers. When the rotation rate is held fixed, and the planetary radius is reduced to induce a higher Ro regime, the Ekman and thermal numbers, which do not depend on a, remain fixed compared to the Earth regime (Figures 3.3a and 3.3e). Thus both frictional and thermal characteristics, controlled by these two parameters, are not changed. However when the rotation rate is reduced, although a higher Ro regime is achieved, the other parameters are also indirectly changed because they also depend on the planetary rotation rate. Therefore the modification in the rotation rate also alters the influence of friction in the boundary layer and changes the cooling and heating rates, i.e. the thermal properties, of the troposphere.

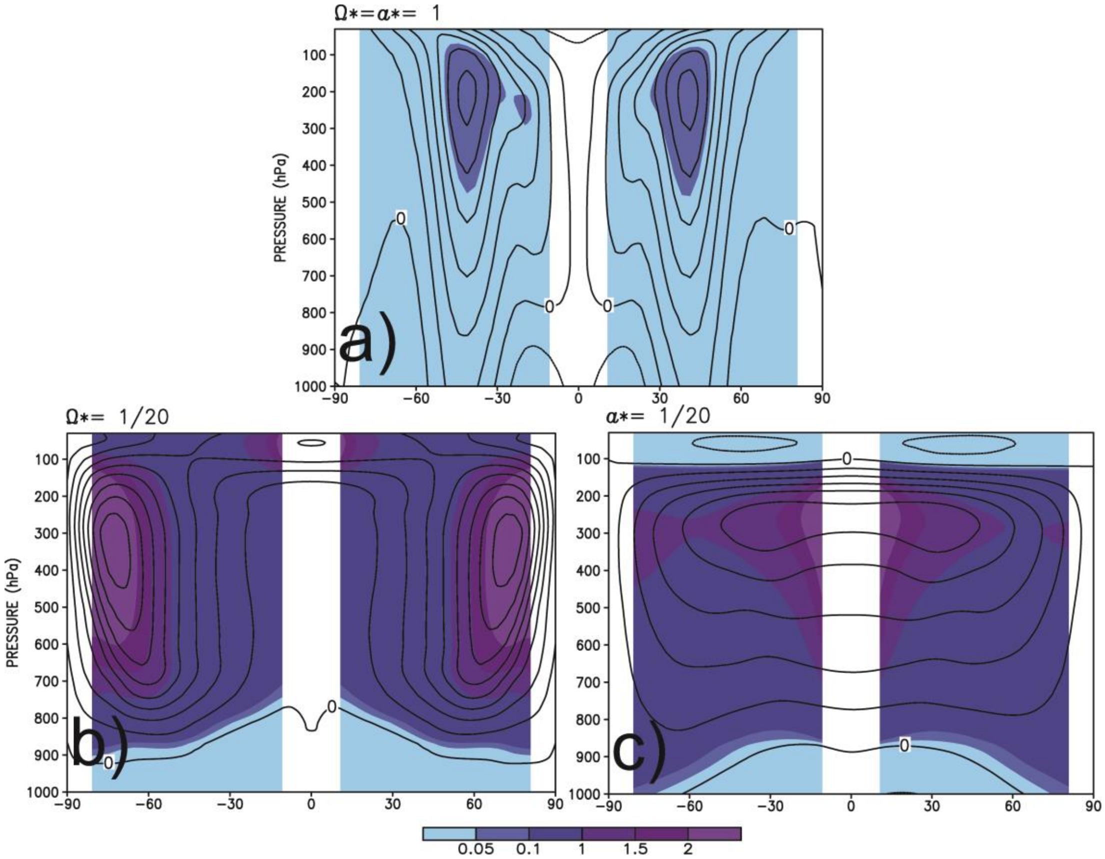

Figure 3.5. Local Rossby number (Ro) given by the time and zonal mean zonal wind (contour, each 10 m s^{-1}) for: a) the Earth-like case experiment Ω*= a*= 1; b) for the slow rotating Ω*= 1/20 experiment and, c) for the smaller radius a*= 1/20 experiment. Calculus was based on eq.3.6 and the values of the Table 3.1.

If the other nondimensional numbers were recomputed for the experiment Ω*= 1/20, one would obtain an Ekman number 20 times bigger and a thermal relaxation coefficient 20 times smaller, which translates to 20 times stronger friction and heating/cooling rates. Read (2011) by computing the Taylor number, which is also a form of friction parameter, for the slow rotation experiments in Williams (1988a,b) paper pointed out that all these regimes were relatively strongly damped and therefore superrotation could not develop. With this high damping close to the surface, a consistent interpretation might involve kinetic energy extracted from the system, not allowing eddies to grow and evolve, and thus suppressing instabilities (JAMES; GRAY, 1986; PASCALE et al., 2013).

Previous analysis has shown that the mean meridional circulation intensifies in the slow-rotating experiment, and consequently suppressing of the superrotation. In order to test these ideas two extra experiments were run, Ω^* =1/20mod and Ω^* =1/20wkhd (see Table 3.1). Since the reduction of the rotation rate simultaneously modifies the three parameters, these experiments were performed in order to evaluate the impacts of offsetting the rotation rate variations in both Ekman E_k and thermal τ_a numbers. By definition E_k proportionally increases to the reduction of Ω whereas τ_a decreases. Therefore these changes were offset by weakening the friction and increasing the thermal relaxation time scale (i.e. leading to a higher thermal inertia) in the Held-Suarez forcing (eqs. 2.24 and 2.25 of Chapter 2) by the same factor.

Figure 3.6a depicts the modified version of the experiment Ω^* =1/20 (Ω^* =1/20mod), in which the intensity of both friction and Hadley cell are modified in order to offset the effects of the slower rotation rate in the nondimensional parameters. A comparison of the magnitude of these numbers as well as the spatial pattern of the zonal mean circulation shows that the results of the experiment a^*= 1/20 were indeed reconstructed (Figure 3.3e). Such a behavior is a direct indication of the dynamical similarity between the two regimes, i.e. atmospheres that shares the same nondimensional numbers are dynamically equivalent and therefore they will exhibit the same statistical properties.

In order to evaluate which parameter is the most important to control the existence and intensity of the superrotation in the slow-rotating simulations, we performed the experiment Ω^* =1/20wkhd (*weaker Hadley*) in which only the intensity of the Hadley cell was changed. Thus the Ekman number remains the same as that of the experiment Ω^* =1/20 (Figure 3.3c), indicating intense friction at the model boundary layer. Figure 3.6c shows a hybrid wind pattern, with two jets in high latitudes but with substantial westerly winds in the equatorial region. This reinforces the importance of the mean meridional circulation intensity on the existence of the equatorial superrotation (SHELL; HELD, 2004), so that by only decreasing the Hadley cell strength the zonal winds pattern in the Figure 3.3c are substantially modified, giving rise to a new configuration depicted by the Figure 3.6c.

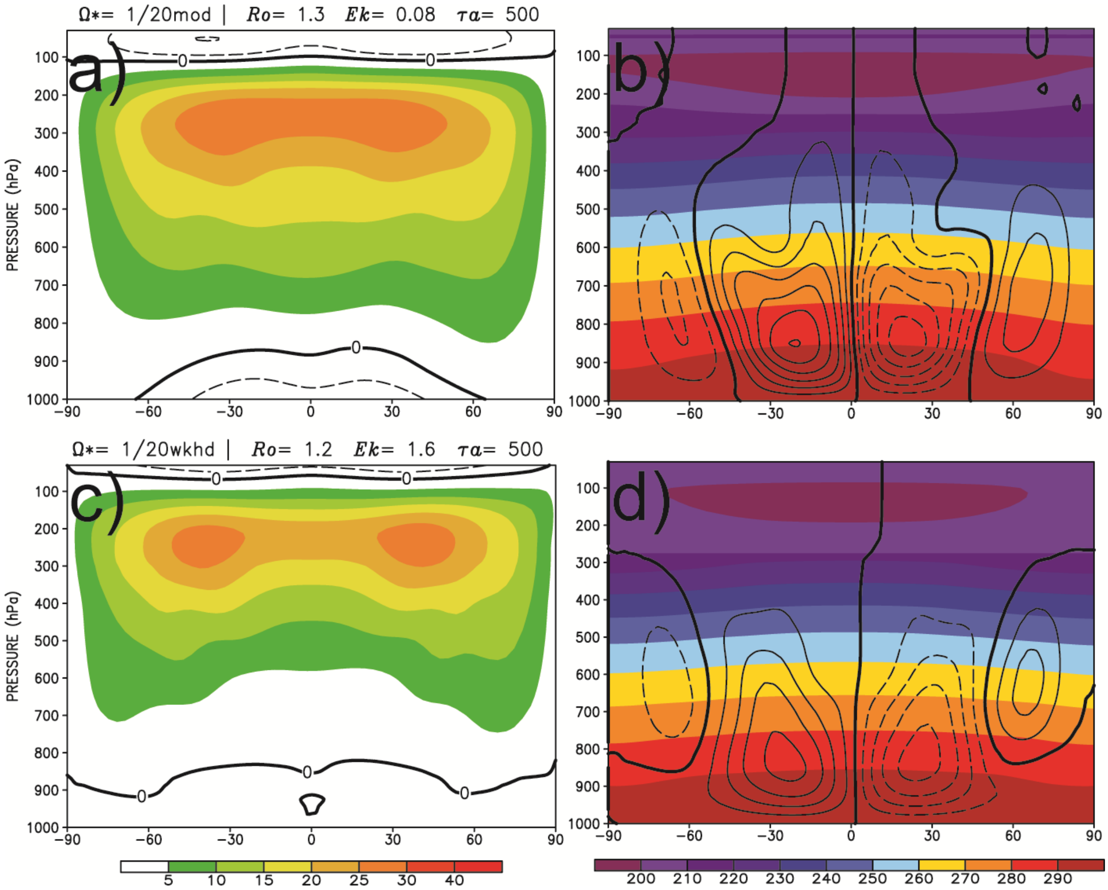

Figure 3.6. Vertical cross-sections of the time- and zonal-mean variables. The left panels are the zonal wind component (westerly winds in shaded; easterlies in dashed line with contour each 3 m s^{-1}). The right panels are temperature (shaded, K) and stream function ψ (contour, kg s^{-1}). a) and b) Experiment Ω*= 1/2mod (ψ contours each 5x10^{9} kg s^{-1}); c) and d) Experiment Ω*= 1/20wkhd (ψ contours each 10x10^{9} kg s^{-1}).The nondimensional parameters were computed based on the values in Table 3.1.

Figure 3.7 presents the wind profile of the zonal mean zonal wind at the jet level for the experiments a*= 1/20, Ω* =1/20 and Ω* =1/20mod, $[\bar{u}]$, along with their associated potential vorticity, PV, and the hypothetical angular momentum conserving zonal wind, U_M. Both the a*= 1/20 and Ω* =1/20mod experiments are in a superrotating state. As it was discussed above such a pattern requires a specific balance of accelerations between the meridional cells and transient eddies at the tropical region. For the experiment Ω* =1/20, however, the zonal wind profile behaves as a nearly angular momentum conserving wind until around 60°, where the eddy accelerations start shifting the actual wind profile away from U_M. The low latitudes also have a very uniform PV distribution, as expected for angular momentum conservation. Therefore with a strong and dominant Hadley cell, the low-latitude circulation behaves as an axisymmetric one, in which an angular momentum maximum at the equator is not allowed to occur (HIDE, 1969; LINDZEN, 1990).

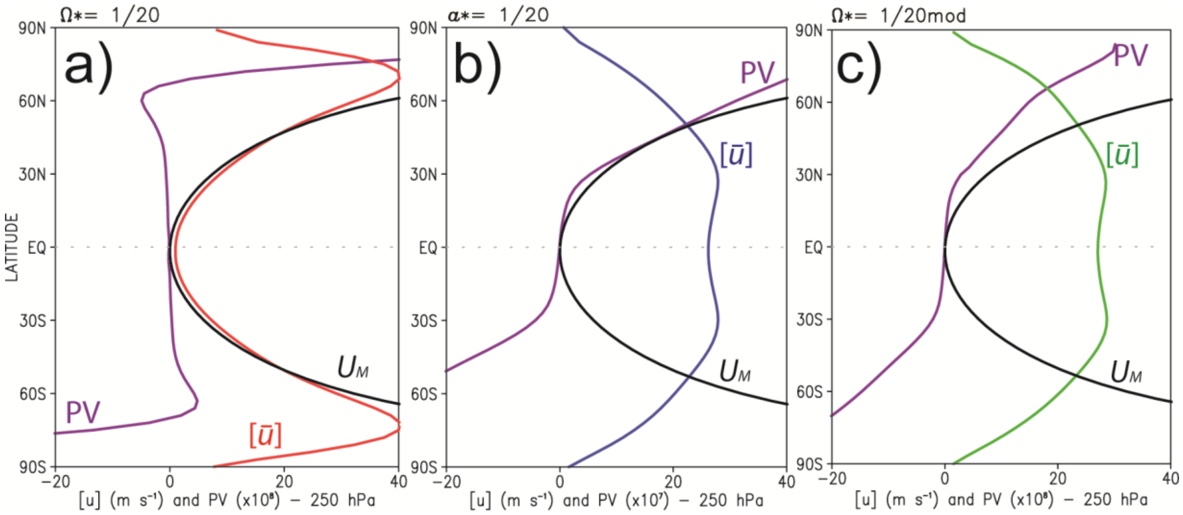

Figure 3.7. Zonal mean zonal wind profile (m s^{-1}) at 250 hPa for the experiments a*= 1/20, Ω* =1/20 and Ω* =1/20mod. The black contour is the angular momentum conserving wind profile, computed as $U_M = \Omega a \frac{sin^2\phi}{cos\phi}$, where a is the planetary radius, Ω is the rotation rate and ϕ is the latitude. The purple contour is the potential vorticity (PV). Values used for the computation are based on the Table 3.1.

3.3.4. Wave and eddies in the high *R*o regime

In Chapter 1, it was argued that under a slow rotation regime, any structure of jet in the zonal flow should be barotropically unstable (ROSSOW; WILLIAMS, 1979) and therefore, propagating modes triggered by the unstable jet in high latitudes could propagate toward the equatorial region inducing convergence of momentum necessary to maintain the winds there (which is the basis of the GRW mechanism; see DEL GENIO; SUOZZO, 1987; DEL GENIO et al., 1993; HOURDIN et al., 1995; DEL GENIO; ZHOU, 1996; WILLIAMS, 2003; LUZ; HOURDIN, 2003; LEBONNOIS et al., 2010). However, based on fundamental properties of linear Rossby waves (see eqs. 11 and 13 from Chapter 1, for example), such a propagation (here is considered Rossby-waves as the planetary disturbances) toward the equator would lead to deceleration in that region, or in other words divergence of momentum.

In order to distinguish which mode contributes toward momentum convergence (acceleration) at the equator, the geopotential height and wind fields were regressed onto the Empirical Orthogonal Functions (EOF, known also as Principal Component Analysis PCA) from the zonally asymmetric component of the geopotential height. EOFs are widely used in meteorology and they are derived as the eigenvalues and eigenvector from a covariance (or correlation) matrix (see LORENZ, 1956; NORTH, 1984; HANNACHI et al., 2007). The first few EOFs (i.e eigenvectors) and the associated eigenvalues are interpreted as natural modes of variability and their spatial patterns. Propagating wave-like oscillations, for instance, are represented by the EOFs analysis as a pair of eigenvectors with similar eigenvalues, and the associated spatial patterns are shifted by a quarter of wavelength. EOF analysis were performed at two different vertical levels: one where the *convergence of momentum at the equator* was maximum, and the second one at higher levels where *the zonal mean winds* were strongest.

Here the analysis are presented for the Ω^* =1/20, a^* =1/20 and Ω^* =1/20mod experiments. Figure 3.8 shows the vertical cross section of the time- and zonal-mean eddy acceleration (related to the convergence of the momentum transport, see eq. 3.9), the zonal-mean wind and a line indicating the levels where the EOF analysis was applied. Figures 3.9 and 3.10 depict the main variability modes of the geopotential height and winds at these lower- and higher-levels and the acceleration associated with the EOFs. The first four EOFs for each experiment, which roughly correspond to 90% of the explained variance of the data, were divided in two groups with the same spatial characteristics and similar variance, thus indicating two distinct, spatially propagating modes.

Although acceleration at the lower troposphere of the equatorial region is observed for the experiment Ω^* =1/20 (Figure 3.8a), the eddies are confined in the regions of intense meridional wind shear close to the jets in the very high latitudes (as previously observed in Figure 3.4c) where non-homogeneous PV is created (Figure 3.7a). In this experiment, the general circulation behaves as if it is nearly axisymmetric and the Hadley cell dominates momentum transport (Figure 3.4c), such that superrotation does not develop. Thus simulations under high *R*o and strong damping (see section 3.3.3) would generate axisymmetric circulations without any significant eddy activity and superrotating jets (GEISLER et al., 1983) at the equatorial region, which was indeed observed in the experiment Ω^* =1/20. The two modes in the geopotential height anomalies (taken at 400 and 600 hPa) are depicted in Figures 3.9a and 3.10a. They are basically composed by high latitude perturbations associated with instabilities generated by strong meridional wind shear on the poleward flanks of the jets. The 1st group (representing more than 80% of the explained variance of the anomalies of geopotential height) is a zonal-wavenumber-one wave whose phase is shifted 180° between the hemispheres (Figures 3.9a and 3.10a) and tilts with latitude in both lower- and higher-levels. Such a horizontal structure is characteristic of a n = 0 mixed Rossby-gravity-like wave (see Figure 3.3c from KILADIS et al., 2009) with a barotropic vertical structure.

This mode is responsible for the acceleration patterns shown by Figure 3.8a, generating small acceleration at the equatorial region at 600 hPa and strong deceleration in high latitudes at 400 hPa. The 2nd group (roughly representing 12% of the explained variance) is composed by a wavenumber one Rossby wave (in phase between the hemispheres), and it does not exert accelerations on the equator.

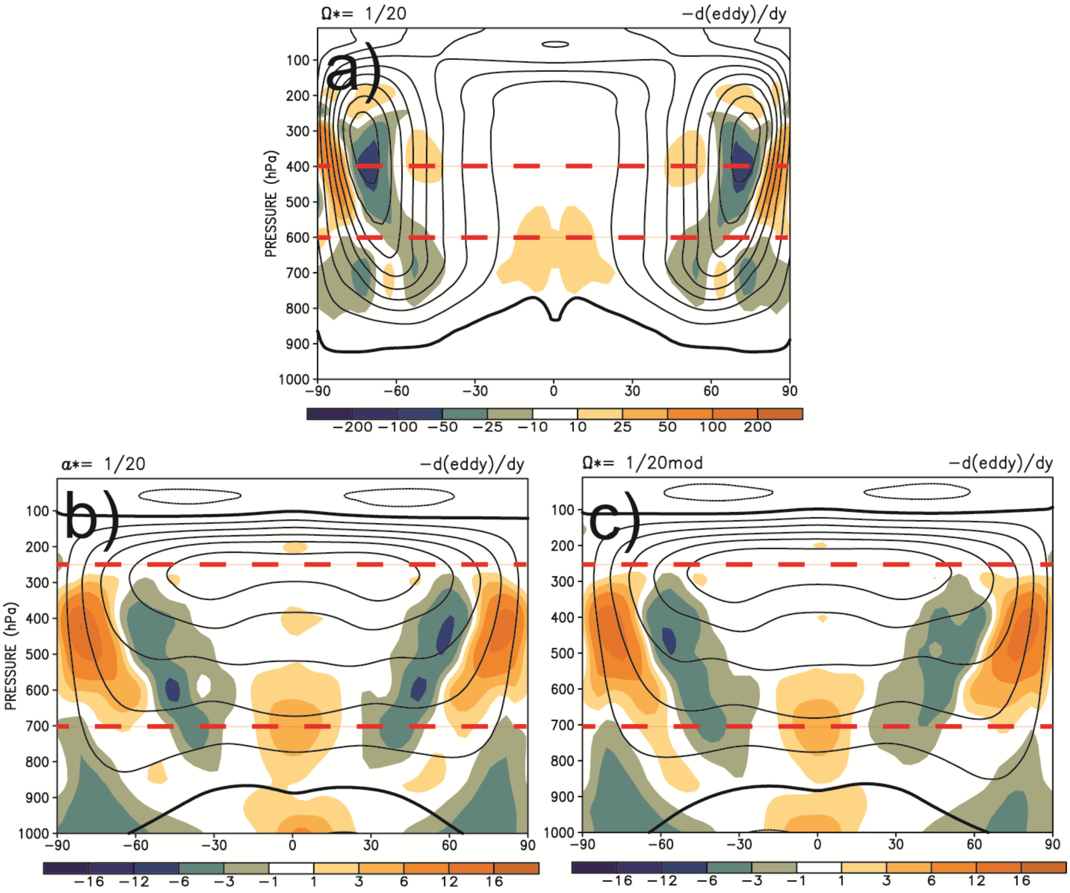

Figure 3.8. Vertical cross section of the zonal mean convergence of momentum by the eddy transients $-\frac{1}{a\cos^2\phi}\frac{\partial}{\partial\phi}\left(\cos^2\phi[\overline{u^*v^*}]\right)$ (shaded, in m s^{-1} day^{-1}) and zonal mean zonal wind (contour with a bold line for zero values, m s^{-1}) for: a) Ω^* =1/20, b) a^* =1/20 and, c) Ω^* =1/20mod experiments. The red dashed lines indicate the levels from which the anomalies of geopotential were taken to perform the EOF analysis.

In superrotating cases, however, a completely different wave pattern emerges. The vertical cross section (Figures 3.8b and 3.8c) of time mean accelerations show the eddies have considerable effects in all equatorial troposphere below 500 hPa with peak aroud 700 hPa, which is the level close to the boundary layer of the model. Above this level at the equator, the time-mean momentum convergence practically vanishes. The pattern of acceleration and deceleration between 60° S – 60° N reinforces the existence of a wider wave guide with eddy source at the equator to promote acceleration of the zonal flow there and deceleration at the flanks. Other regions of acceleration (with maximum between 400 – 500 hPha) are closely related to the meridional wind shear at the high latitudes as in the previous experiment.

Both in the reduced radius and in the modified slow-rotating experiment, the presence of strong and persistent westerly winds in the equatorial region is accompanied by the same two wave modes (Figures 3.9 and 3.10b,c). The 1st group shows pairs of cyclones and anticyclones in high latitudes with unit zonal wavenumber. The geopotential anomalies associated with these planetary-scale Rossby waves are stronger in higher levels although the waves have a barotropic structure with the alignment of cyclones and anticyclones in height. The acceleration/deceleration in the 1st group is located poleward of 30° in lower-levels of the atmosphere.

The 2nd group, although less important to the explained variances (i.e. patterns more transient in time), is the most important source of momentum convergences at the equator (b and c plots in Figures 3.8, 3.9 and 3.10). It is composed of a pair of wavenumber-one equatorial waves coupled with high latitude waves with a shift of around 180° between their phases. The spatial pattern resembles that observed in equatorial Rossby waves $n = 1$ from Matsuno's theory, consisting of a quadrupole of streamfunctions anomalies of opposite signs, symmetric about the equator giving rise to the characteristic "cyclone/anticyclone" pairs (WHEELER; KILADIS, 1999) with an extratropical projection. Differently from 1st group, the vertical structure has strong variation, with the equatorial wave more intense and meridionally wider in higher levels than its extratropical counterpart, thus indicating that the 2nd group is a baroclinic mode. Consistent with the baroclinic structure, the latitudinal tilting in their phase lines at 700 hPa indicates momentum transport from higher to lower latitudes (grey lines in the Figure 3.8). The wave guide of the equatorial Rossby wave, between 30° S and 30° N at 700 hPa and 60° S and 60° N at 250 hPa, reflects the meridional extension of the acceleration and decelerations described above within the same range of latitudes.

Mitchell and Vallis (2010) noticed in their idealized experiments that when *R*o exceeded unit, a global scale wavenumber one eddy response arose converging momentum in the equatorial region and inducing superrotation. The main mode found by the authors was basically composed by high latitude Rossby waves and a well-developed off-phase Kelvin wave ("the chevron" mode). Such a coupling of Kelvin and Rossby waves has also been reported in other theoretical studies, as for example Iga and Matsuda (2005, Figure 16), Yamamoto and Takahashi (2006, Figure 14) and Potter et al. (2014, Figure 16).

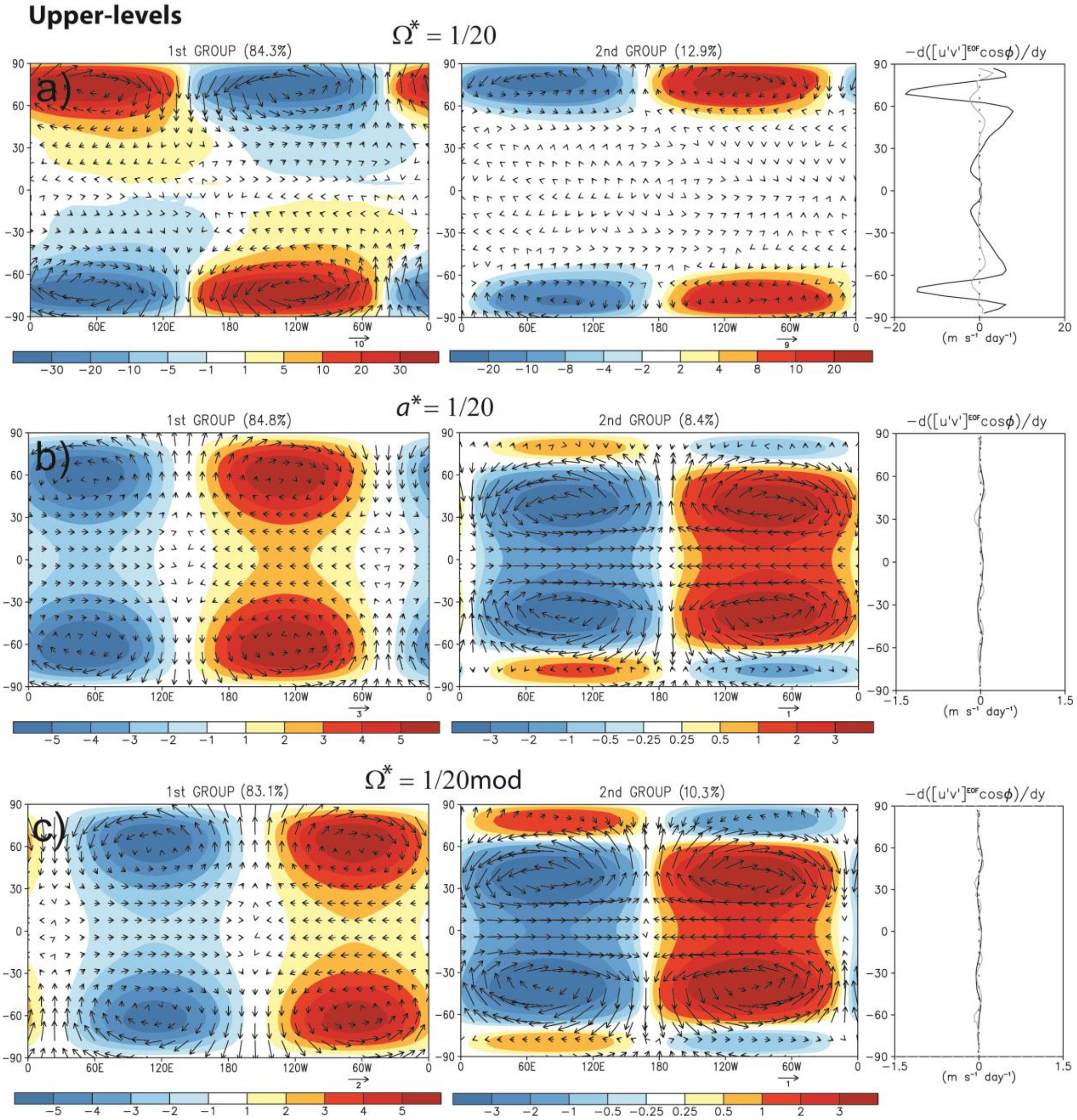

Figure 3.9. Variability patterns of geopotential height (shaded, m) and horizontal wind (vector, m s^{-1}) associated with the EOFs for: a) experiment Ω^* =1/20 at 400 hPa, b) experiment a^* =1/20 at 250 hPa and, c) experiment Ω^* =1/20mod at 250 hPa. Convergence of momentum by each group of modes is also depicted in the panels on the right (black lines for 1st group and grey lines for the 2nd group, m s^{-1} day^{-1}). The percentage refers to the sum of the explained variance of the EOFs related to that mode.

On the other hand, some studies imposing anomalous heat sources in the equatorial region for the Earth's Rossby number regime found a global scale eddy response (for example Figure 3c in KRAUKUNAS; HARTMANN, 2005, and Figure 3b in ARNOLD et al., 2012) with anticyclones flanking the equator upstream of the heating source and cyclones downstream (with structure similar to the 2nd group obtained in Figures 3.9 and 3.10b,c) and with tilted phase lines so that momentum could be transported toward the equator (CABALLERO; HUBER, 2010). The novel results of this thesis suggest that the spontaneous, i.e. not dynamically forced, convergence of momentum to the equator in the higher Rossby number regime involve this same kind of wave structures. This may indicate that not only more dynamical paths are possible but also that different modes could be candidates to produce and/or sustain superrotation in the atmosphere.

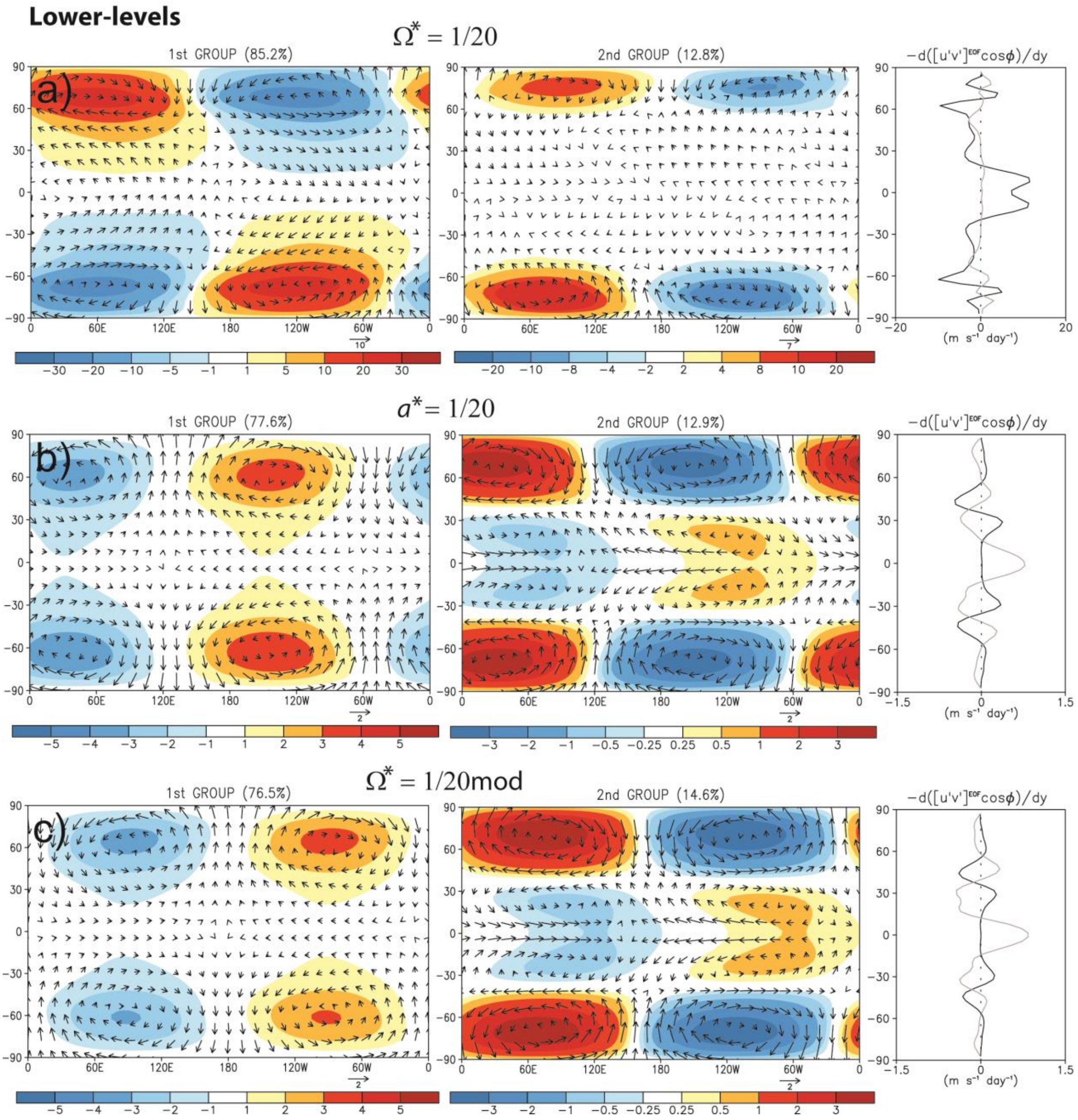

Figure 3.10. Variability patterns of geopotential height (shaded, m) and horizontal wind (vector, m s^{-1}) associated with the EOFs for: a) experiment Ω^* =1/20 at 600 hPa, b) experiment a^* =1/20 at 700 hPa and, c) experiment Ω^* =1/20mod at 700 hPa. Convergence of momentum by each group of modes is also depicted in the panels on the right (black lines for 1st group and grey lines for the 2nd group, m s^{-1} day^{-1}). The percentage refers to the sum of the explained variance of the EOFs related to that mode.

3.3.5. Dynamical origin of the modes from experiment a^* = 1/20

In this section, some possible origins of the modes present in the experiment $a^* = 1/20$ are briefly explored. Spectral analysis was applied in order to identify the main frequencies of oscillation of the modes described in the last section. Power spectra of the zonal wind anomalies (more details will be given in Chapter 4) indicates that there are two main frequency bands: the 1st group is a slower mode with frequency around $0 < \omega < 0.1$ cycles-per-day; whereas the faster 2nd group has a frequency lying $0.4 < \omega < 0.6$ cycles-per-day. Figure 3.11 shows the time series of the geopotential height at 250 hPa filtered to only retain these two bands. Based on the horizontal structure of the waves in Figure 3.9b we identified the latitude of the grid point closest to maximum amplitude of the waves (for both the longitude was arbitrarily chosen to be 0°).

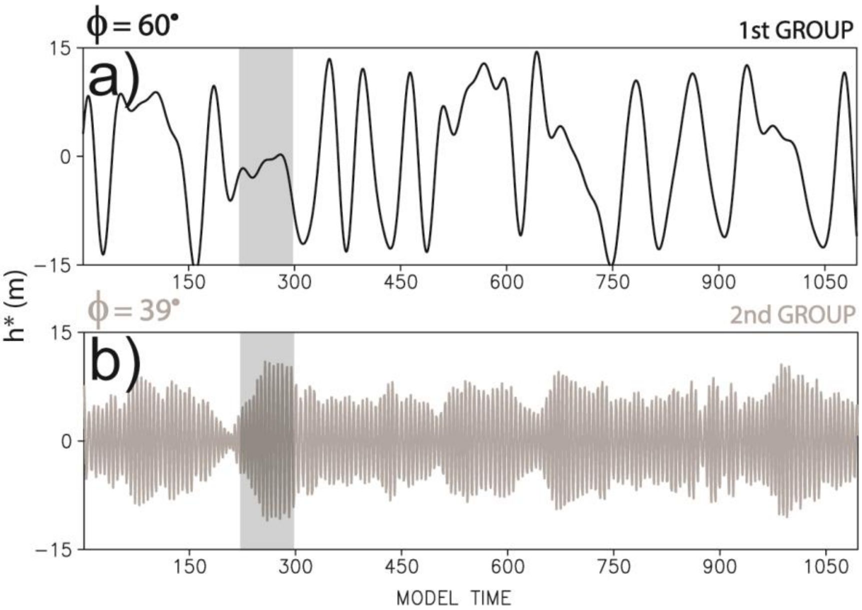

Figure 3.11. Time series of the geopotential height anomalies (contours, m) at 250 hPa filtered in the frequency bands of the two dominant modes present in the experiment a^* = 1/20. a) 1st group, taken at latitude of 60° and b) 2nd group, taken at latitude of 39°. Both longitudes were arbitrarily chosen to be 0°. The area highlighted in grey was used to compute the meridional PV gradient and potential temperature in Figure 3.12b.

Apart from the natural oscillation of each mode, there are modulations of the amplitude of these oscillations. When 1st group has minimum in amplitude, the 2nd group obtains slightly higher amplitude (highlighted area in grey, for example, on Figures 3.11a and 3.11b). This coordinated behavior might indicate some interaction between these two modes and will be investigated in Chapter 4. The role of both barotropic and baroclinic instabilities, however, acting in the maintainance of the superrotation during the steady state is explored in Figure 3.12. According to Vallis (2006), Mitchell and Vallis (2010) the presence of the barotropic and baroclinic instabilities is identified through the spatial distribuition of the meridional gradient of the zonal-mean potential vorticity ($\partial\overline{[\mathrm{PV}]}/\partial y$). When meridional gradient of absolute vorticity (also PV) changes sign in the absence of horizontal gradient of potential temperature, there are conditions favorable for barotropic instability, whereas changes in sign of meridional gradient of PV indicates condition favorable for baroclinic instability in the presence of horizontal gradient of potential temperature.

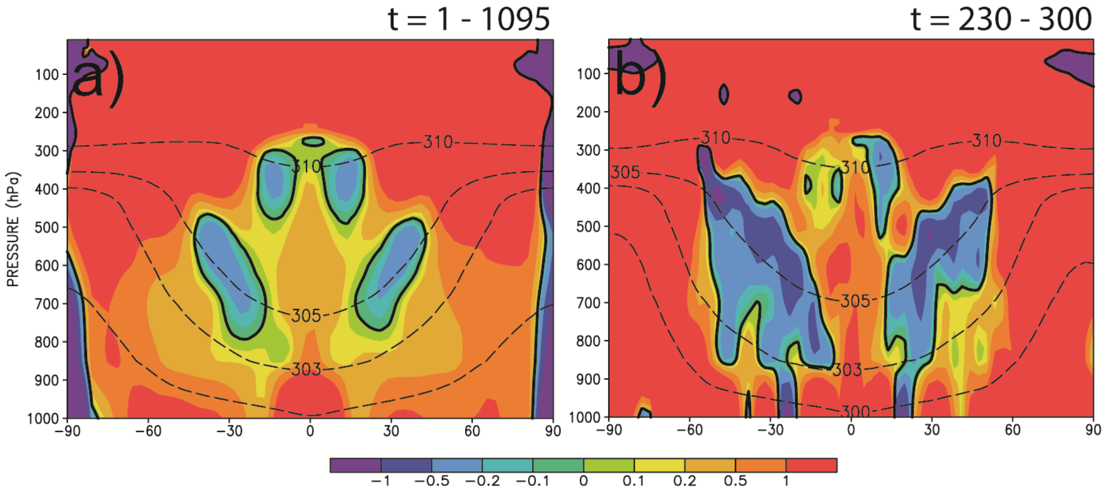

Figure 3.12. Vertical cross section of time- and zonal-mean potential vorticity gradient (shaded, x10^{12}) and potential temperature (dashed lines, K) for the experiment a^* = 1/20. a) values averaged over the entire period, b) values averaged from model time 230 to 300, which is roughly represented by the grey box in Figure 3.11.

When averaged over the entire analysis period of the simulation (Figure 3.12a), it is clear that there are several regions of PV reversal in the troposphere. At very high latitudes the abrupt change in signal of $\partial\overline{[\mathrm{PV}]}/\partial y$ indicates a possible the role for barotropic instability at these regions, which is confirmed by the existence of the slow-propagating barotropic Rossby waves (1st group, see Figures 3.9b and 3.10b). Near the subtropical latitudes, PV gradient reverses sign in the presence of potential temperature gradient, which is confirmed by the existence of the fast-propagating baroclinic equatorial Rossby-waves from the 2nd group. There is also reversal of the PV gradient in low levels at the equatorial region, which may indicate a mixed barotropic-baroclinic instability as argued in Mitchell and Vallis (2010).

As mentioned before, during the periods of weak amplitude oscillation of 1st mode, the amplitude mode from the 2nd group grows. One of these periods is displayed in

Figure 3.12b. The high latitude PV gradient reversal vanishes whereas abrupt and strong vertical variation in the lower-level PV gradient is observed. This behavior along with a bigger slope of the 300 K isothermal contour indicates stronger role of the baroclinic instability at this short periods. Therefore there is a mix in average of the barotropic and baroclinic instabilities acting in the troposphere, but there is a clear distinction between the modes and each related instability.

3.3.6. Analysis of the spin-up period of the model

Motivated by the fact that different wave modes could be responsible for the generation and maintenance of the superrotation in a high Rossby number atmosphere as the literature suggests, here an analysis of the spin-up of the simulation $\alpha^* = 1/20$ is presented.

Figure 3.13a shows the vertical cross section of the time evolution of the zonal mean zonal wind $[\bar{u}]$ averaged between 15° S – 15° N latitudes, from the initial axisymmetric phase to the establishment of superrotation. Westerly winds are initially generated in the upper atmosphere near 200 hPa, but rapidly extend to 600 hPa by day 150. A gradual increase in the wind intensity between 400 – 200 hPa occurs until time 500. This is followed by an abrupt adjustment phase leading to the steady-state configuration after time 600. Since eddy disturbances are necessary for the convergence of momentum at the equator, Figure 3.13b depicts the instantaneous accelerations within the same region (15° S – 15° N) due to the horizontal momentum convergence by the eddies.

Two distinct regimes are also noted for the same period of Figure 3.13a. In the first one, which is active from time 150 until around time 500, the level of maximum acceleration is around 600 hPa with only sporadic episodes in levels above and below. Between times 500 and 600, the period of abrupt downward shift of the westerly wind layer, the level of maximum acceleration also shifts to 700 hPa (roughly tracking where the velocity of the wind was around 5 – 10 $\mathrm{ms^{-1}}$). In the steady state, the maximum of the eddy acceleration remains around 1000 and 700 hPa (see also Figure 3.8b). As already shown in the steady state analysis, the areas of most intense eddy momentum convergence do not correspond to the level of wind maximum (~ 250 hPa). However, studying the levels where eddy convergence is present reveals which modes contribute to the maintenance of superrotation. Given the transient state and fast evolution of the quantities during the spin-up, an EOF analysis is problematic, and thus it was shown snapshots of the zonally asymmetric components, filtered for wavenumber one, during the generation of superrotation.

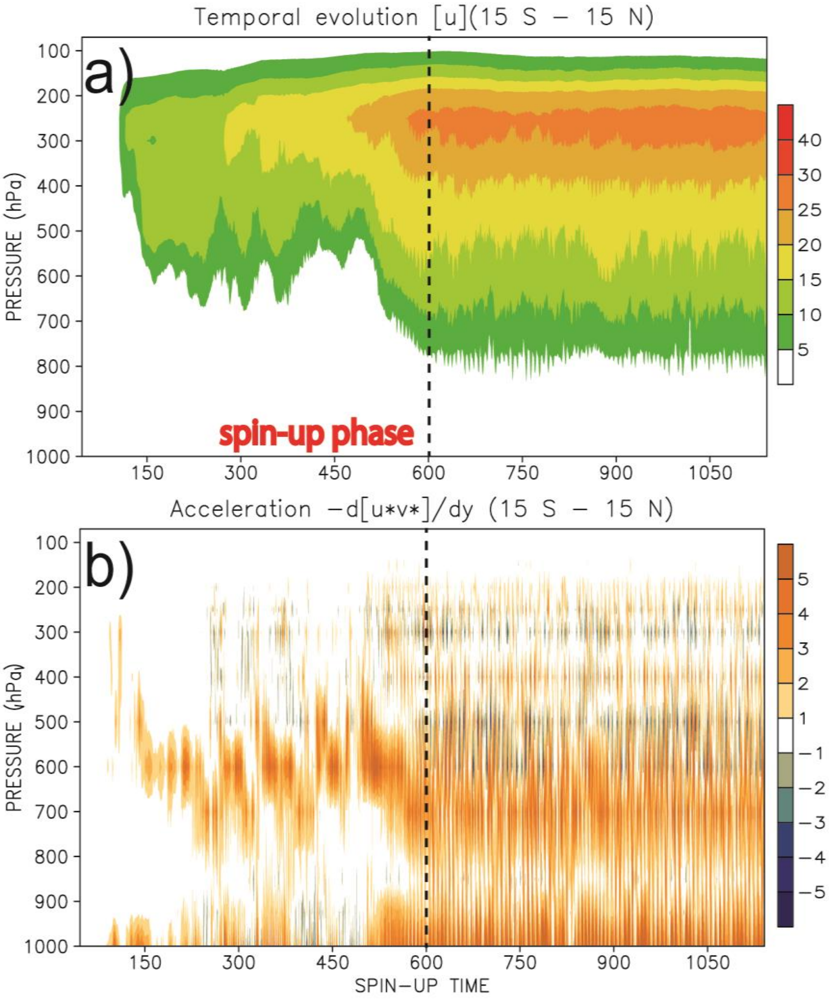

Figure 3.13. Vertical cross section of the time evolution of the: a) zonal mean zonal wind component (m s^{-1}) and b) instantaneous acceleration due to eddies (m s^{-1} day^{-1}). Both variables are averaged between 15º S and 15º N latitudes. The dashed line indicated the approximated time that divides the spin-up and the steady state of the simulation.

Figure 3.14 shows snapshots of the zonally asymmetric component of wind and geopotential filtered for wavenumber one, and the zonal mean of their instantaneous acceleration. The selected periods are roughly related to times of maximum acceleration in 600 hPa. During the gradual evolution of the wind field, between times 150 and 500, the anomalies are very close in shape to the wavenumber one Kelvin- and Rossby-like waves (Figures 3.14a, 3.14b and 3.14c). These high latitude Rossby-like waves are coupled to an equatorial Kelvin-like wave. Although the signature of the equatorial Kelvin wave is weaker, the patterns related to positive and negative anomalies of geopotential and the winds match those found in a pure Kelvin wave n = -1, obtained from the shallow-water solutions of Matsuno (1966) (KILADIS et al., 2009, Figure 3f). The positive geopotential anomalies are associated with eastward zonal flow whereas the negative ones are associated with westward zonal flow, and the zonal flow associated with this Kelvin wave decays away from the equator. The building-up of persistent westerly equatorial winds during this period is due to the coupling of these modes, as described in Mitchell and Vallis (2010), Potter et al. (2014).

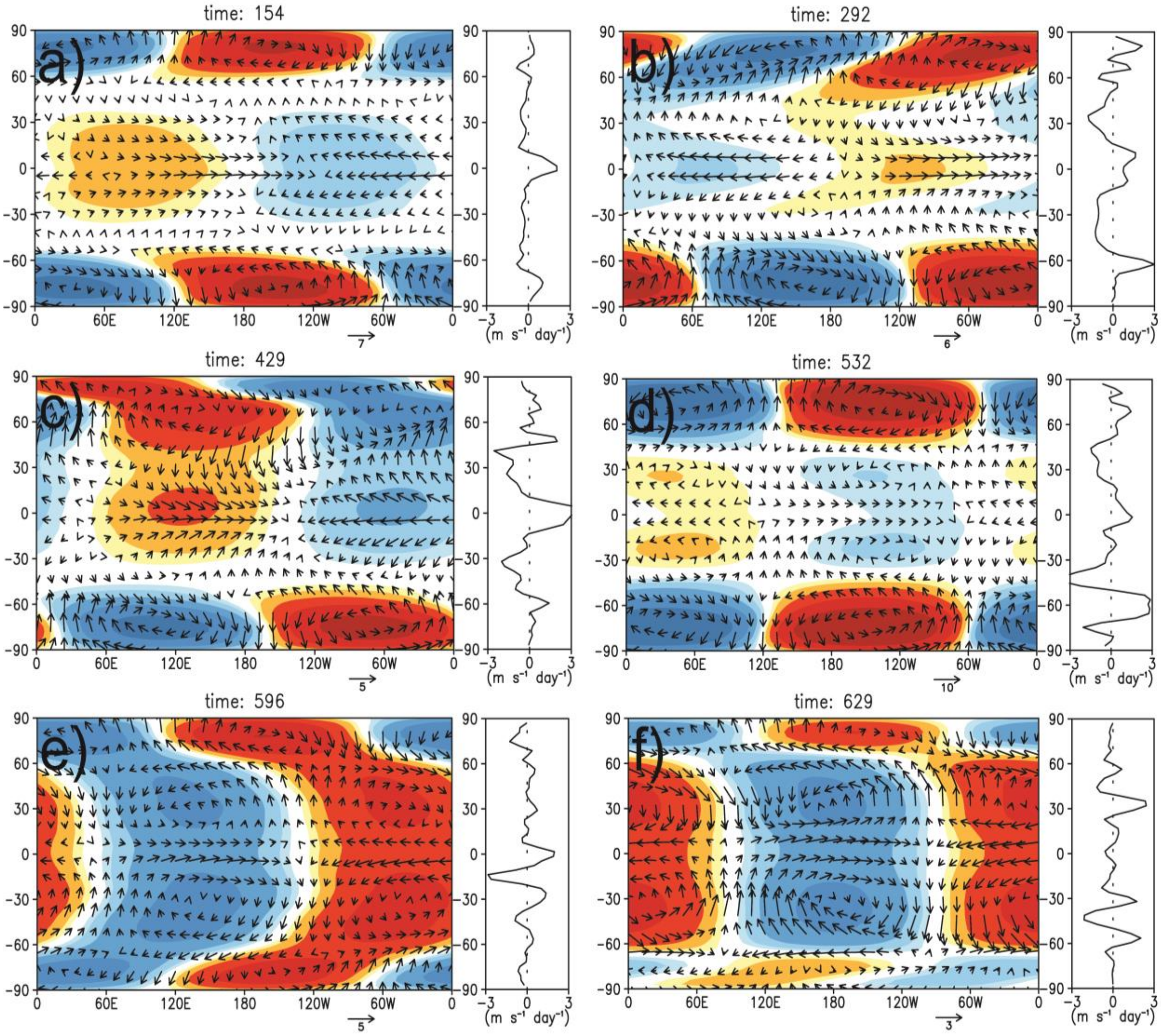

Figure 3.14. 600 hPa geopotential anomalies (shaded, m), wind (vectors, m s^{-1}) and instantaneous accelerations (contours, m s^{-1} day^{-1}) at different instants during the spin-up of the simulation a^* = 1/20: a) time 154, b) time 192, c) time 429, d) time 532, e) time 596, and f) time 629. The selected period refer roughly to the times of maximum acceleration in Figure 3.13b.

After time 429, the abrupt transition occurred leading to another regime in which, as shown by Figure 3.14d, equatorial Rossby-like waves accelerate the equatorial winds. It is just after this period that superrotation is fully established in whole troposphere. Afterwards the accelerations are no longer intense and persistent at 600 hPa, and the eddy field is dominated by a Rossby-like mode similar to those found in the 2nd group of the steady state (Figures 3.9c, 3.14e and 3.14f). Such an evolution indicates that the formation and existence of the Rossby-Kelvin-like coupling is crucial to the onset of persistent westerly winds over the equator, while Rossby-Rossby-like coupling promote expansion of westerly equatorial winds through the depth of the troposphere and maintain superrotation through the steady state.

3.4. Discussion

In this first part of the results, superrotation in the context of higher Rossby number atmospheres was studied by performing numerical simulations with a simplified Earth-like GCM set for either a slow rotation rate or a reduced planetary radius. Substantial differences in strength and zonal mean pattern of the zonal winds were found when running the model with a slow rotation rate, which is the traditional approach, and a smaller planetary radius. By analysis of the simulations, the key elements inhibiting superrotation in slowly rotating Earth-like GCMs were elucidated.

When set to a slower rotation rate, the model generated an almost axisymmetric circulation, with strong jets in the very high latitudes and wider Hadley cells. The transport of momentum in this experiment was due basically to the strong mean meridional circulation that diverges momentum from the equatorial region and brings it into the high latitudes feeding the jets. Any convergence of momentum at the equator does not overcome the effects of the strong Hadley cell. The simulation with a reduced planetary radius, on the other hand, develops robust superrotation, produces a nearly barotropic thermal structure, i.e., lacking strong latitudinal temperature gradients, in almost all troposphere and has a very weak mean meridional circulation with momentum transport very similar in magnitude to the eddy transport. Differently from the slowly rotating experiment, stronger convergence of momentum is produced in a large part of the lower troposphere, where the effects of the friction are present. The momentum convergence practically vanishes in the upper troposphere in the steady state. A small, vertical transport of momentum is provided by the mean meridional circulation. In the strongly superrotating levels aloft, on the other hand, the lack of forcing by eddies indicates that little is required to maintain the zonal flow, in contrast to the lower levels where stronger dissipation from Rayleigh friction is present. In the steady state, two dynamically active modes are dominant. The first one is a slow-propagating, barotropic, high-latitude Rossby wave and causes acceleration just in higher latitudes. The second one is a fast-propagating, baroclinic, equatorial Rossby-like wave with an extratropical projection and it is responsible for all convergence of momentum at the equator. Although the 1st mode is not responsible for the maintenance of the superrotation, its interaction with 2nd mode seems important in short and transient periods of time. For the spin-up phase, on the other hand, it is the Rossby-Kelvin coupling that is responsible for the onset of the superrotation.

CHAPTER 4.

Results – Part II

Wave structure and dynamics in a superrotating terrestrial atmosphere

The interplay between the mean meridional circulation and transient eddies define the form of the basic general circulation of a planetary atmosphere. Under higher Rossby number regime the poleward momentum transport by a wider Hadley cell combined with equatorward large-scale eddy momentum transport generate a superrotating equatorial zonal circulation. The general shape of these disturbances and how they transfer kinetic energy to the basic state flow through the convergence of momentum at the equator are, nonetheless, still object of controversy. In this second part of the results, a comprehensive analysis of the tridimensional structure and life cycle of atmospheric waves is presented and their interaction with the mean flow which maintain the strong, long-lived superrotating state in a higher Rossby number regime atmosphere is analyzed. The results show that the mean zonal superrotating circulation is maintained by only evoking the dynamical interaction between Rossby waves to converge eddy momentum fluxes at the equatorial region. The energetics of the circulation indicates massive transfer of kinetic energy from the equatorial Rossby wave to the mean flow occurring during short periods of stronger activity of the baroclinic instability. The modulation of amplitude of the equatorial and extratropical Rossby waves suggests a non-linear mechanism of eddy-eddy interaction between these modes.

4.1. Theoretical background

The existence of a predominantly zonal circulation with a fast jet at the equatorial region in higher Rossby number atmospheres, such as in Venus and Titan, is a characteristic of the phenomenon of superrotation. In Chapter 1 it was shown that a pure axisymmetric circulation could not have a maximum of angular momentum in the equatorial region unless momentum was transported upgradient by non-axisymmetric motions. In an attempt to explain how superrotation was maintained in Venus, the Gierasch-Rossow-Williams mechanism, GRW, (GIERASCH, 1975; ROSSOW;

WILLIAMS, 1979) establishes that there is a balance between the angular momentum carried by the mean meridional overturning circulation and equatorward eddy angular momentum transport (Figure 4.1). Therefore it is expected that wave-like disturbances transport momentum toward the equatorial region and consequently the superrotating state is maintained.

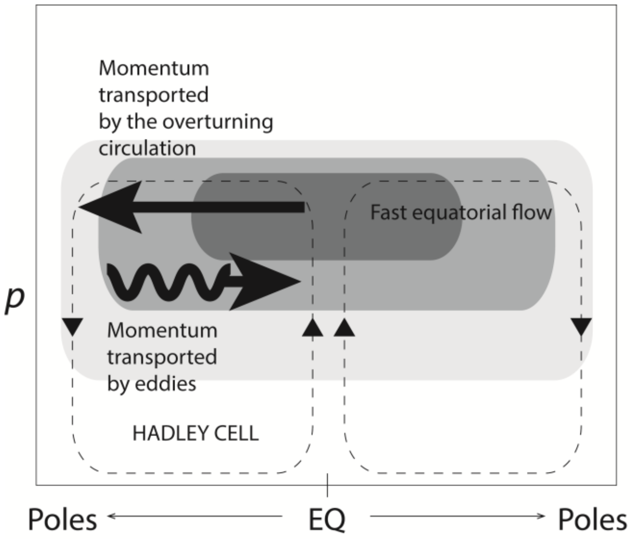
Momentum transported by the overturning circulation
Fast equatorial flow
p
Momentum transported by eddies
HADLEY CELL
Poles
EQ
Poles

Figure 4.1 – Schematic vertical cross section displaying the zonal mean zonal wind (shaded, arbitrary scale) and the balance of momentum described the Gierasch-Rossow-Williams mechanism in a superrotating atmosphere. Theory shows that the vertically integrated momentum is transported poleward by the mean overturning circulation (black arrow, arbitrary size) and equatorward by eddies ("wavy" black arrow, arbitrary size) so that fast zonal current is maintained at the equatorial region.

Observational data from several spacecraft missions to Venus have provided valuable information on the large-scale wave modes that could be responsible for this mechanism. The existence of a "Y"-like cloud structure in Venus has always been considered as a wave phenomenon manifestation (Figure 4.2a). Belton et al. (1976) analyzed UV contrast of images from Marineer 10 and speculated that the hemispherically symmetric large-scale brightness distribution could be result of a superposition between an equatorial-like Kelvin wave and mid-latitude Rossby waves. Del Genio and Rossow (1990) confirmed these results by analyzing UV images from Pioneer Venus, and Smith et al. (1992, 1993) provided an explanation of the "Y" feature as being the wave coupling modulating the advective patterns of the clouds. New studies using improved techniques and data from other missions such as, Venus Express and Galileo (SANCHÉZ-LAVEGA et al., 2008; KOYAMA et al, 2012) have also confirmed previous analyses.

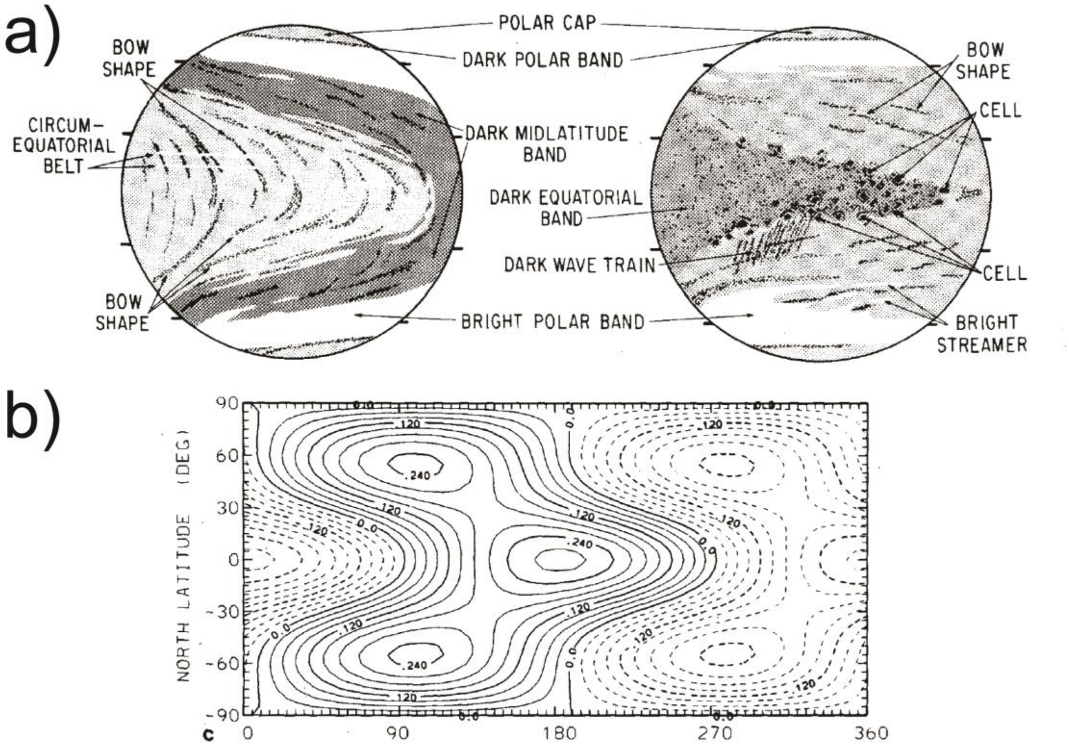
a)
POLAR CAP
DARK POLAR BAND
BOW SHAPE
CIRCUM-EQUATORIAL BELT
DARK MIDLATITUDE BAND
DARK EQUATORIAL BAND
DARK WAVE TRAIN
BOW SHAPE
BRIGHT POLAR BAND
BOW SHAPE
CELL
CELL
BRIGHT STREAMER
b)
NORTH LATITUDE (DEG)
90
60
30
0
-30
-60
-90
c
0
90
180
270
360
.120
.240
0.0

Figure 4.2 – Large-scale features on the cloud-top of Venus atmosphere based on: a) schematic diagram describing the main cloudiness features observed by the ultraviolet images of Pioneer Venus; the two views represent the maximum and minium configurations of the tilt and typically occur two days apart (adapted from ROSSOW et al., 1980); and b) the horizontal combination of the horizontal structure of a extratropical Rossby wave and an equatorial Kelvin wave which explains the Y-like shape of the Venus upper level clouds (adapted from COVEY; SCHUBERT, 1982)

The observations revealed two interesting aspects: one, the main feature of the wave remained almost unchanged through the decades, and two, this wave is sporadic in nature (DEL GENIO; ROSSOW, 1990; SMITH et al, 1992; YAMAMOTO; TAKAHASHI, 2012). Numerical modelling of the Venus atmosphere (COVEY; SCHUBERT, 1982; IGA; MATSUDA, 2005; YAMAMOTO; TAKAHASHI, 2006; IMAMURA, 2006; YAMAMOTO; TAKAHASHI, 2012) also relates the existence of coupling between Kelvin and Rossby waves as the dynamical mechanism behind the superrotation maintenance at the cloud top of Venus. Yamamoto and Takahashi (2003) showed that different kinds of waves contributed in different vertical levels of their model to produce equatorward transport of momentum, especially Mixed-Rossby-Gravity, Rossby and gravity waves. Although these studies are valuable in the sense that most of the features detected in observations were reproduced in simulations, they have not provided a deeper insight on the dynamics of interaction of these waves and the mean flow. Nevertheless they have shown a different mechanism than that proposed by Rossow and Williams (1979) that barotropic extratropical propagating Rossby waves would drive superrotation.

These findings suggest that there is evidence that a hybrid, large-scale mode comprised of an equatorial Kelvin wave and a mid-latitude Rossby wave is the major feature of Venus upper atmosphere (Figure 4.2b). For Titan, however, due to the lack of observations to identify signatures in the lower- and higher-levels of its atmosphere, the structure of the main modes is still not certain. Mitchell et al. (2011) provided numerical results of waves that could be responsible for the large-scale cloudiness patterns observed by the Cassini spacecraft during singular storm events near Titan's northern hemisphere spring equinox. The authors suggest that the same coupling that was observed in Venus could be responsible to force vertical motions, consequently forming methane clouds and, ultimately, precipitation on the surface. The authors did not provide an assessment on how these waves might dynamically interact with the mean flow to maintain superrotation. On the other hand, idealized simulations for Titan's dynamical regime, from Mitchell and Vallis (2010), suggested that a mixed barotropic and baroclinic instability could act in order to generate a mode that possessed the same characteristic that was observed in the Rossby-Kelvin coupling. Indeed, Wang and Mitchell (2014) demonstrated the existence of a linear instability between equatorial Kelvin waves and high latitude Rossby waves that leads to superrotation.

Chapter 3 presented a comprehensive study to identify why idealized models tend to produce different results when, in order to reproduce a condition of higher Rossby number regime, either the rotation rate or the planetary radius is reduced. Principal component analysis from the eddy component of the geopotential height during the steady state suggested that, differently from the results obtained by Mitchell and Vallis (2010), another coupling involving only Rossby waves could be responsible for the maintenance of superrotation. The analysis presented here aims to extend the ideas of Chapter 3 by analyzing the three dimensional structure and life cycle of the atmospheric waves and their interaction with the mean flow in the superrotating regime. The main goal is to provide a description of how the modes evolve in time and transfer kinetic energy to the mean state through convergent equatorward momentum transport (the wavy arrow in the Figure 4.1). This chapter is organized as follows: section 4.2 describes the methodology, section 4.3 presents the spectral analysis and the energetic processes of the filtered modes, and section 4.4 gives the main discussions.

4.2. Methodology

4.2.1. Numerical experiments

The analyses are based on two numerical experiments: the control, set for the Earth parameters, and second one with the planetary radius 20 times smaller than Earth's (380 km), corresponding to the superrotating simulation of $a^* = 1$ and $a^* = 1/20$ from Chapter 3. Starting from a motionless atmosphere, the simulations were run for ten years in order to achieve a statistically steady state, and additional three years for the analysis. In terms of resolution and vertical levels, the simulations are similar to the previous numerical experiments, with 3.0° X 3.0° of horizontal grid spacing and 32 levels, respectively.

4.2.2. Spectral analysis technique

Following Hayashi (1982), the spectral analysis is used to interpret observed and simulated disturbances in terms of wave modes by determining their wave characteristics, structure and energetics. The space-time Fourier components can resolve the disturbances into eastward and westward moving components (ZANGVIL; YANAI, 1980), and the main dominant wavelength, frequency and direction of propagation are obtained directly by inspection of the power.

Consider that both u and v wind data series are cyclic in longitude (x direction) and limited in time ($0 < t <$ T). The time-space spectra of the non-axisymmetric component of the wind are determined from the complex Fourier transform,

$$U_{k,\omega} = \frac{1}{2\pi T}\int_0^T dt \int_0^{2\pi} u(\lambda, t)e^{-i(k\lambda+\omega t)}d\lambda \tag{4.1}$$

$$V_{k,\omega} = \frac{1}{2\pi T}\int_0^T dt \int_0^{2\pi} v(\lambda, t)e^{-i(k\lambda+\omega t)}d\lambda \tag{4.2}$$

where ω is the frequency and k the zonal wavenumber that fits along a latitude circle. By definition here, k is always positive; and $\omega > 0$ and $\omega < 0$ correspond to eastward- and westward-propagating modes, respectively. The power spectrum (P) of the zonal wind component is defined as the variance of the time-space Fourier component (Hayashi, 1982),

$$P_{k,\omega} = \frac{1}{2}\left\langle \left|U_{k,\omega}\right|^2 \right\rangle \tag{4.3}$$

where ⟨ ⟩ indicates the time average in the Fourier space computed by smoothing frequencies with a Gaussian window (see RANDEL; HELD, 1991; MITCHELL; VALLIS, 2010).

Additionally cross-spectral analysis was employed to compute the meridional eddy momentum fluxes in the wavenumber-frequency domain in order to determine which modes contribute to these fluxes in both Earth-like and superrotating regimes. Following Randel and Held (1991) the estimate of the time-space cospectrum power density (*CP*) of the momentum flux is given by the real part of,

$$CP_{k,\omega} = 2Re(\langle U_{k,\omega}\tilde{V}_{k,\omega}\rangle) \tag{4.4}$$

where the "~" term refers to the complex conjugate and *Re* the real component. To determine the phase speed of the modes that contribute to the eddy fluxes, it is necessary to transform the cospectra from the wavenumber-frequency to wavenumber-phase speed spaces. According to Randel and Held (1991) the spectral power density in the wavenumber-phase speed space is determined in such a way that the total power is conserved in the transformation from the frequency domain, so

$$CP_{k,\omega}\,\Delta\omega = CP_{k,c}\,\Delta c \tag{4.5}$$

Since the frequency is defined as $\omega = c(k/a\,cos\phi)$, we have

$$CP_{k,c} = CP_{k,\omega}\left(\frac{k}{a\,cos\phi}\right) \tag{4.6}$$

Fourier transforms were computed by the Fast Fourier Transform (FFT) in space and time, and after the operations the fields gridded in zonal wavenumber k and phase speed c were obtained.

4.2.3. The Lorenz energy cycle

The Lorenz energetics (LORENZ, 1955, 1967) represent the processes of generation, conversion and dissipation of available potential and kinetic energies and their relation with the general circulation of the atmosphere. Based on the idea of eddies embedded in a mean flow, Lorenz derived a set of equations from the momentum, mass and thermodynamics relationships that described the energetic processes related to eddies, to the zonally-averaged flow and the interaction between them. By portioning the energies into zonal mean and eddy forms, the budget equations for the available potential energy and kinetic energy are given by,

$$\frac{\partial A_Z}{\partial t} = -C_Z - C_A + G_Z \tag{4.7}$$

$$\frac{\partial K_Z}{\partial t} = C_Z + C_K - D_Z \tag{4.8}$$

$$\frac{\partial A_E}{\partial t} = C_A - C_E + G_E \tag{4.9}$$

$$\frac{\partial K_E}{\partial t} = C_E - C_K - D_E \tag{4.10}$$

where, A and K refer to the available potential and kinetic energies; the subscripts Z and E indicates the zonal mean and the eddy contents of these energies. C_Z is the conversion between A_Z and K_Z; C_A is the conversion between A_Z and A_E; C_E is the conversion between A_E and K_E, and C_K is the conversion between K_E and K_Z. G_Z and G_E denote the generation of zonal available and eddy available potential energies, and D_Z and D_E indicate the dissipation terms of kinetic energy.

The notation proposed by Brennan and Vincent (1980), regarding mean and eddy motions, is adopted. The averaging operators are defined as,

$$[(\ \ )] = \frac{1}{\lambda_E - \lambda_W} \int_{\lambda_W}^{\lambda_E} (\ \ ) d\lambda \tag{4.11}$$

the zonal average and,

$$\overline{(\ \ )} = \frac{1}{\sin \phi_N - \sin \phi_S} \int_{\phi_S}^{\phi_N} [(\ \ )] \cos \phi \, d\phi \tag{4.12}$$

the area average over the globe. Here ϕ is the latitude, λ the longitude, and *N*, *S*, *E* and *W* the boundaries in the north-, south, east and west directions respectively.

The deviations of these averages are defined as,

$$(\ \ )^* = (\ \ ) - [(\ \ )] \qquad (\ \ )'' = [(\ \ )] - \overline{(\ \ )} \tag{4.13}$$

Based on the fact that the disturbances develop superposed to a zonal flow, Lorenz (1955, 1967) partitioned the available potential and kinetic energies in the zonal and eddy forms,

$$A_Z = \int_{p_t}^{p_b} \frac{\overline{T''^2}}{2\bar{\sigma}} dp \quad (4.14) \qquad A_E = \int_{p_t}^{p_b} \frac{\overline{T^{*2}}}{2\bar{\sigma}} dp \quad (4.15)$$

$$K_Z = \frac{1}{g}\int_{p_t}^{p_b} \frac{\overline{([u]^2 + [v]^2)}}{2} dp \qquad (4.16) \qquad\qquad K_E = \frac{1}{g}\int_{p_t}^{p_b} \frac{\overline{(u^{*2} + v^{*2})}}{2} dp \qquad (4.17)$$

The averaged static stability parameter is

$$\bar{\sigma} = \left(\frac{g\bar{T}}{c_P} - \frac{pg}{R}\frac{\partial \bar{T}}{\partial p}\right) \qquad (4.18)$$

The conversions terms are given by:

$$C_Z = -\frac{1}{g}\int_{p_t}^{p_b} \frac{R}{p}\overline{\omega^{''}T^{''}}\, dp \qquad (4.19) \qquad\qquad C_E = -\frac{1}{g}\int_{p_t}^{p_b} \frac{R}{p}\overline{\omega^{*}T^{*}}\, dp \qquad (4.20)$$

$$C_A = -\frac{1}{g}\int_{p_t}^{p_b} \frac{1}{\bar{\sigma}}\left(\frac{1}{a}\overline{v^{*}T^{*}\frac{\partial T^{''}}{\partial \phi}} + \overline{\omega^{*}T^{*}\frac{\partial T^{''}}{\partial p}}\right) dp \qquad (4.21)$$

$$C_K = \frac{1}{g}\int_{p_t}^{p_b} \left(\frac{\cos\phi}{a}\overline{u^{*}v^{*}\frac{\partial}{\partial \phi}\left(\frac{[u]}{\cos\phi}\right)} + \overline{v^{*2}\frac{\partial [v]}{\partial \phi}} + \frac{\tan\phi}{a}\overline{u^{*2}[v]} + \overline{\omega^{*}u^{*}\frac{\partial [u]}{\partial p}} + \overline{\omega^{*}v^{*}\frac{\partial [v]}{\partial p}}\right) dp \qquad (4.22)$$

The terms related to generation and dissipation processes are generally computed as residuals of the Lorenz equations. However their general form is expressed by

$$G_Z = \int_{p_t}^{p_b} \frac{\overline{Q^{''}T^{''}}}{c_p\bar{\sigma}} dp \qquad (4.23) \qquad\qquad G_E = \int_{p_t}^{p_b} \frac{\overline{Q^{*}T^{*}}}{c_p\bar{\sigma}} dp \qquad (4.24)$$

$$D_Z = \int_{p_t}^{p_b} \overline{\left([u][F_\lambda] + [v]\left[F_\phi\right]\right)} dp \qquad (4.25) \qquad\qquad D_Z = \int_{p_t}^{p_b} \overline{\left(u^{*}F_\lambda^{*} + v^{*}F_\phi^{*}\right)} dp \qquad (4.26)$$

For the equations above, u, v and ω are the components of the wind; T is the absolute temperature; g is the gravity acceleration (9.81 m s^{-2}); c_P is the specific heat at constant pressure (1004 J kg^{-1} K^{-1}); a is the planetary radius; R is the gas constant of the dry air (287 J kg^{-1} K^{-1}); p_b, p_t are the pressure-level limits of the vertical integration (1000 – 10 hPa); Q is the diabatic heating, and F the frictional forces.

Figure 4.3 depicts the energy cycle in the Earth's atmosphere, given by the eqs. (4.7) – (4.10), by showing the positive sense of generation, conversion and dissipation among the zonally-averaged and eddy forms of available potential and kinetic energies. Besides, the main mechanisms responsible for the conversion of energy as seen by Lorenz are also illustrated in this figure. The cycle starts with the generation of available potential energy with positive correlation of diabatic heat sources and temperature (eqs. 4.22 and 4.23) enhancing thermal contrasts along either the latitudinal (G_Z) or longitudinal (G_E) directions (LORENZ, 1967; ASNANI, 1993). The surplus of energy in the "warmer" latitudes and the lack in the "colder" ones lead to creation of upward motion of warmer air and downward motion of colder air masses in different latitudes circles by means of a thermally-driven overturning circulation. This process indicates negative correlation between mean vertical motions ω'' and temperature T'', and consequently generation of positive C_Z (eq. 4.19). In this situation, kinetic energy is generated at expenses of the available potential energy of the mean state (LORENZ, 1967). According to Peixoto and Oort (1992), the Hadley cell is one example of this conversion between Earth's tropical and subtropical latitudes, whereas the Ferrell cell is a case of indirect cell with subsidence of relatively warm air and ascending of relatively cold air.

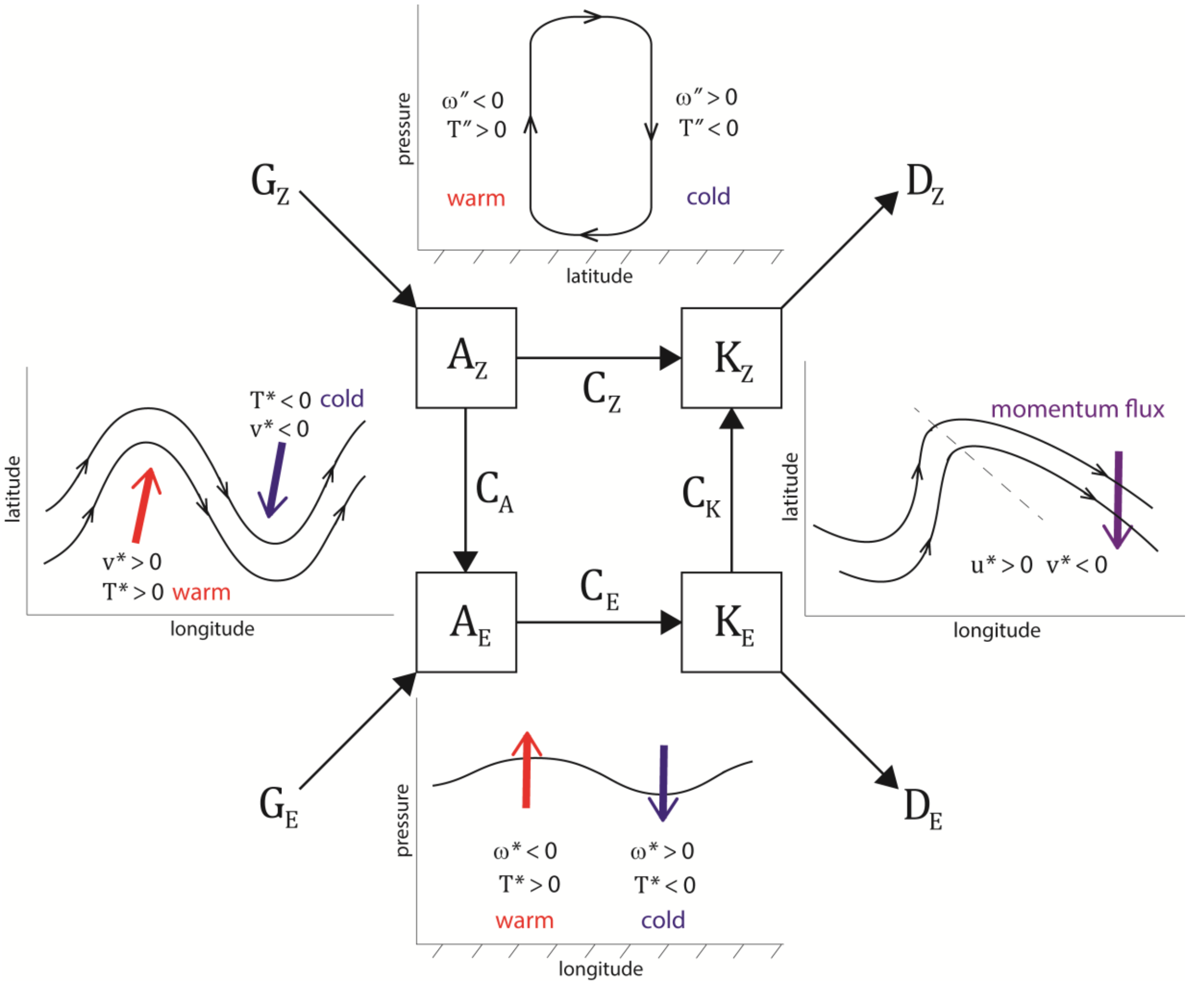
pressure
ω″ < 0
T″ > 0
warm
ω″ > 0
T″ < 0
cold
latitude
G_Z
D_Z
A_Z
K_Z
C_Z
C_A
C_K
A_E
K_E
C_E
G_E
D_E
latitude
T* < 0 cold
v* < 0
v* > 0
T* > 0 warm
longitude
momentum flux
latitude
u* > 0 v* < 0
longitude
pressure
ω* < 0
T* > 0
warm
ω* > 0
T* < 0
cold
longitude

Figure 4.3 – Schematic plot of the complete energy cycle in the atmosphere as seen by Lorenz for the Northern Hemisphere. The main physical processes associated with positive conversion (given by the arrows) of the one form of energy to another is also shown (see text for more details).

In a developing baroclinic wave, axisymmetric meridional heat transports (given by the C_A term) will carry relatively warmer air toward “colder” latitudes whereas relatively colder air is brought into “warmer” latitudes. Since this transport is non-zonally uniform, thermal contrast in the same latitude circle will be created and A_Z is converted into A_E (eq. 4.21). According to Carlson (1991) the wavy structure of troughs and ridges in the jets of the Earth atmosphere are manifestation of the C_A term. Regions of vertical motion in a baroclinic wave are manifestation of the term C_E (HOLTON, 2004) in which vertical transport of warm and cold air is accomplished by an induced vertical circulation along one latitude band converting A_E into K_E (eq. 4.20). In general, it is difficult to obtain the sign of the term C_K (WIIN-NIELSEN; CHENG, 1993), although small positive values are found in a global perspective (see OORT, 1964) expressing conversion between K_E and K_Z (eq. 4.22). Star (1948) showed that the orientation of the troughs and ridges axes in meteorological charts indicates momentum fluxes toward the poles. ¨Therefore the momentum transport associated with the baroclinic transient disturbances in the Earth atmosphere return kinetic energy to the mean flow, thus contributing to the maintenance of the mid-latitude jets structure against the turbulent dissipation (JAMES, 1994), which is given by the D terms (eqs. 4.25 and 4.26). In episodes of barotropic instability, on the other hand, the signal of C_K is reversed, meaning that kinetic energy is extracted from the mean flow in order to amplify the kinetic energy of the disturbances.

In the literature (see for example in WIIN-NIELSEN; CHENG, 1993) the sense of the energy flow given by $A_Z \rightarrow A_E \rightarrow K_E$ and $K_Z \rightarrow K_E$ are defined, respectively, as the baroclinic and barotropic chains. The interpretation of the energy cycle for the superrotating atmosphere (section 4.3.3c) is presented in terms of the physical processes that were described above, which are familiar for the Earth’s atmosphere.

4.3. Results

4.3.1. Earth-like vs. Superrotating regime: zonal wind and eddy momentum fluxes distribution

The resulting atmospheric circulation exhibits two different behaviors when the simulation is performed under either Earth-like or higher Rossby number regimes. Figure 4.4 depicts the vertical cross section of the time- and zonal-mean wind and eddy momentum fluxes. The Earth-like regime is characterized by a mid-latitude and subtropical westerly flows, with maximum in the upper levels, and a weaker easterly flow at the low levels in the tropical region (Figure 4.4a). In the higher Rossby number configuration, however, the bulk circulation is predominately eastward with maximum of the wind velocities at the tropical region. Although weaker compared to the actual values of wind speed found in both Venus and Titan atmospheres, the zonal wind is strong and persistent throughout the simulation with mean values about 25 m s^{-1} (Figure 4.4b). Such a pattern of strong long-lived westerlies at the equator is defined as the superrotating state (Williams, 2003).

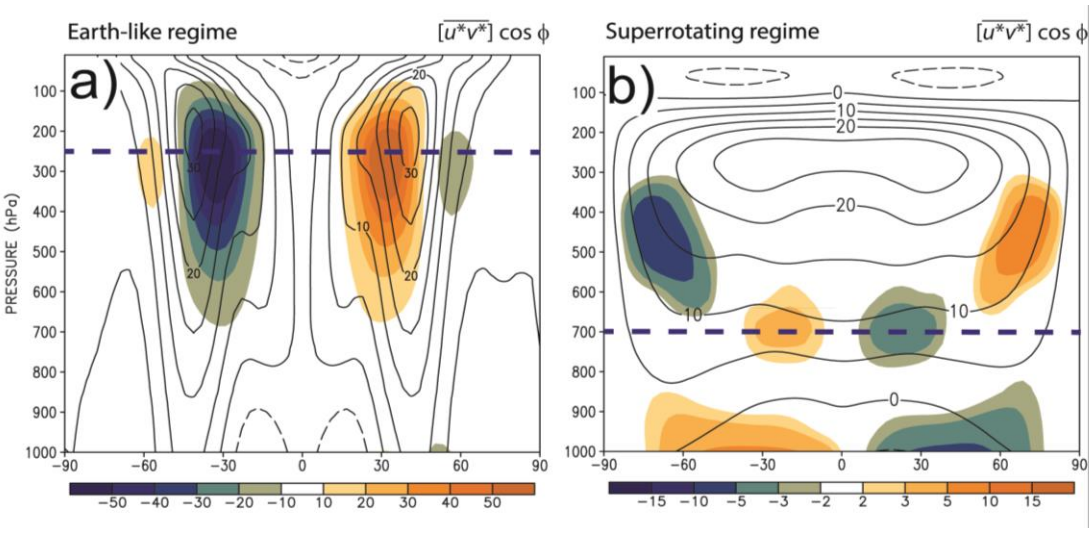

Figure 4.4 – Vertical cross-sections of the time- and zonal-mean wind (contour, each 5 m s^{-1}) and eddy momentum fluxes (shaded, m^2 s^{-2}) for the: a) Earth-like regime and b) Superrotating regime. The blue dashed lines over the two plots indicate the vertical pressure level where the spectral analysis technique was applied (see text for more details).

The difference in the zonal mean wind distribution is also apparent in different eddy momentum transport configurations. Strong momentum fluxes are found around the jet cores in the Earth-like regime. In this dynamical regime (also valid for Mars) mid-latitude baroclinic instability generates perturbations by which the mean zonal flow is maintained (PEIXOTO; OORT, 1992). Although eddy velocities have no mean by definition, the average of the product between them can be nonzero if the eddies have a particular configuration in space (GROTJAHN, 1993). The strong poleward transport in both hemispheres in the higher levels (Figure 4.4a) is a characteristic due to large-scale disturbances in the troposphere. According to Peixoto and Oort (1992), the wave-like structure of the eddies is meridionally oriented in such a way that the trough-ridge axes are tilted and then poleward eddy momentum fluxes are generated (see Figure 11.6 from PEIXOTO; OORT, 1992). These fluxes are maximum about 40° of latitude in both hemispheres, and tend to converge close to wind maxima around 250 – 300 hPa.

In the superrotating regime, on the other hand, a wind maximum at the equatorial region demands transport of momentum toward equator such that momentum flux converges there. Such a behavior is constrained by Hide's theorem (HIDE, 1963) and forms the basis of the GRW mechanism (Gierasch-Rossow-Williams; see Chapter 1 for more details) to explain Venus superrotation. Although the maximum of the eddy fluxes and winds is tightly coupled in the same region of the atmosphere in the Earth-like regime, in a configuration of atmospheric superrotation, they are not coincident. While the maximum of the winds is located near 250 hPa, the maxima of the equatorward eddy momentum fluxes are in the low levels close to 700 hPa (Figure 4.4b and Figure 3.9b), which is consistent with findings from idealized experiments of Mitchell and Vallis (2010), Potter et al. (2014). According to results in Chapter 3 (section 3.3.2), in a superrotating atmosphere eddies transport more momentum where friction is present to sustain westerly flow against friction, which is applied as a Rayleigh friction in the low levels of the model (see the formulation of the idealized forcing in Chapter 2, section 2.2). Since superrotation is achieved in the high levels of the atmosphere, where little dissipation is applied, less momentum transport is required from the disturbances to maintain the zonal flow at the equator in the steady state (SARAVANAN, 1993; MITCHELL; VALLIS, 2010).

The shape and main properties of the eddies, which can explain the pattern of the momentum fluxes from the Earth regime are widely known, as discussed before. However in a higher Rossby number configuration and within an atmosphere in superrotation these characteristics require further investigation. In the next section some fundamental elements of the eddies are described through spectral analysis from the eddy components of the wind.

4.3.2. Spectral analysis of the eddy component of the wind

The existence of non-zero eddy fluxes in the Earth-like and superrotating atmospheres requires a deeper analysis on the main characteristic of the existing disturbances in both circulation patterns. For that, spectral analyses were employed in order to assess the dominant wavenumber, phase speed and frequency of the wave-like modes.

Figure 4.5 shows the latitudinal distribution of the cospectra of the eddy momentum fluxes in both regimes. FFT was applied to the vertical pressure levels where the fluxes important for the maintenance of the jets were maxima. Based on Figure 4.4 the levels of 250 hPa and 700 hPa, for Earth-like and superrotating regimes respectively, were chosen for the computation (dashed blue lines on the plots). For the Earth-like regime, the latitudinal structure and strength of the zonal wind control the momentum flux distribution in the phase speed domain (Figure 4.5a). According to the linear theory, the absence of $\overline{[u^{*}v^{*}]}$ for phase speeds faster than $[\bar{u}]$ indicates that disturbances will not propagate meridionally further than critical latitudes where $[\bar{u}] \approx c$ (RANDEL; HELD, 1991; ZANGVIL; YANAI, 1980). Thus eddies with faster phase speed tend to be more confined closer to the jet cores. According to Randel and Held (1991), Vallis (2006), high-level disturbances generated by mid-latitude baroclinic instability with phase speed c will propagate away from their source region (around 40° latitude), where $[\bar{u}]$ is faster than c, toward regions with small $[\bar{u}] - c$ where they preferentially break and dissipate. Therefore disturbances with slower phase speed tend to penetrate deeper into the subtropical region (around 10°) (Figure 4.5a). Poleward momentum fluxes are mostly transported by eddies with phase speed between 5 – 15 m s^{-1}.

Figure 4.5b displays the horizontal scale of the dominant eddies. The substantial portion of the fluxes are due to the large scale waves with wavenumber ranging from k = 5 – 8, which gives a characteristic wavelength about 4,300 – 6,900 km.

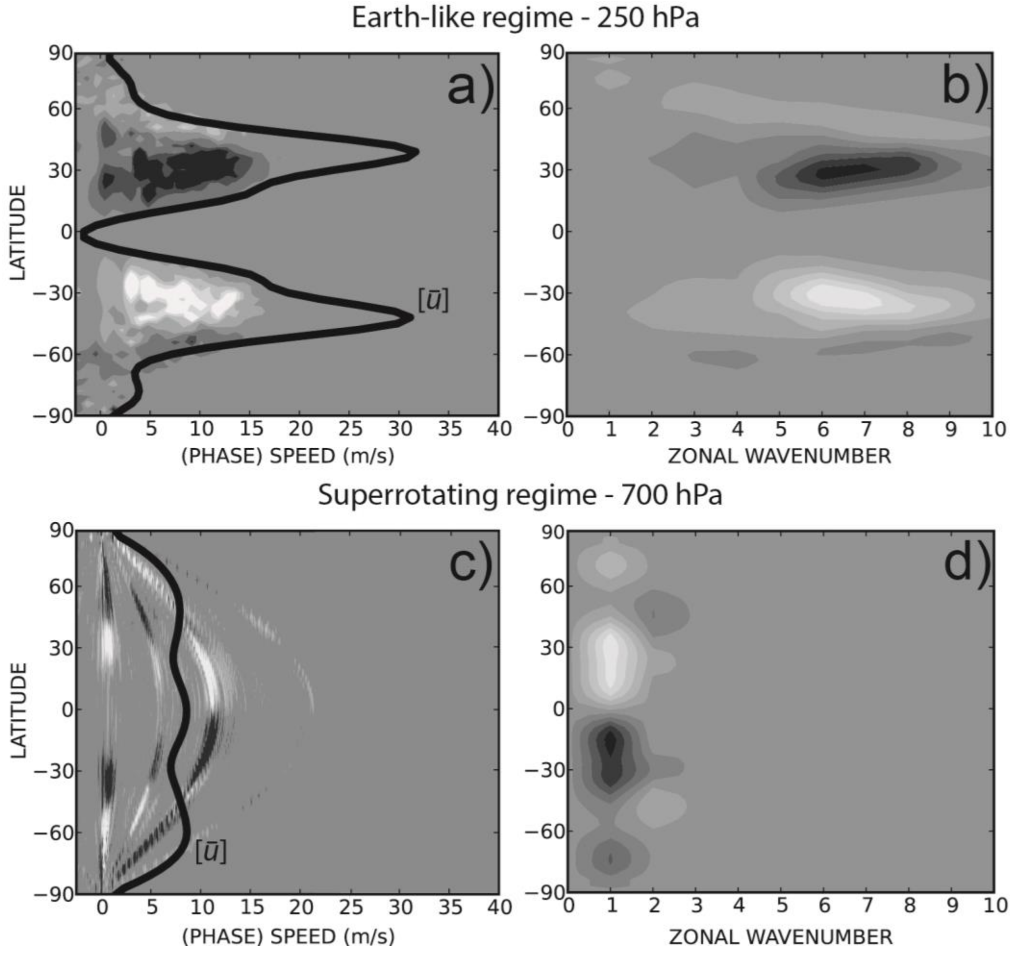

Figure 4.5 – Latitudinal distribution of the eddy momentum flux cospectra $CP_{k,\omega}$ (m^2 s^{-2}, shaded) computed for the Earth-like regime at 250 hPa level (upper panels) and for the superrotating regime at 700 hPa (lower panels), as function of: a) and c) phase speed (integrated over all wavenumbers) and, b) and d) zonal wavenumber (integrated over all phase speeds). The contour represents the time- and zonal-mean zonal winds (m s^{-1}) averaged over the entire period at the respective levels. Dark colors indicate northward eddy momentum transport while brighter colors indicate southward transports.

Spectral analysis applied in the superrotating regime reveals striking differences, as depicted by Figures 4.5c and 4.5d. The latitude-phase speed distribution of the eddy cospectrum shows that the disturbances associated with equatorward eddy momentum fluxes act in the tropical region (between 30° S and 30° N) and they have phase speed faster than the time mean zonal flow. It is clear that there is no association between the momentum fluxes and zonal winds distribution in this regime. Decoupling between the momentum fluxes and zonal flow was also found by several authors, including idealized experiments from Yamamoto and Takahashi (2003), Mitchell and Vallis (2010) and more realistic simulations by Newman et al. (2011). In this condition, the linear theory to explain the acceleration of the mean flow based on the propagation of modes toward their critical lines should not be applied. Zonal wavenumber one disturbances transporting momentum towards equator (Figure 4.5d) have been found by several authors as another common feature among all superrotating circulations and indicates that superrotation is maintained by global-scale modes.

Although the dominant eddies in the Earth dynamical regime are certainly turbulent at some aspects, they still retain some behavior in which the linear theory could be applied (RANDEL; HELD, 1991). On the other hand, some characteristics depicted by the spectral analysis for the superrotating regime indicate that linear theory is not sufficient in explaining the momentum fluxes distribution. Thus a deeper study about the properties and structure of the main modes in the superrotating state will be carried out in the next sections.

4.3.3. Wave structure and properties in the superrotating state

4.3.3a. Spatial characteristics of the filtered modes

The logarithm of the power spectrum applied for the zonal wind component $P_{k,\omega}(u^*)$ at 700 hPa is shown in Figure 4.6. Each individual power spectrum corresponding to single latitudes was summed up in the whole domain to give the characteristic frequency and wavenumber from the modes present in the superrotating atmosphere. The existence of wavenumber one modes is not only the main spatial characteristic of the waves responsible for the eddy momentum fluxes (Figure 4.5d) but also for the whole disturbed component of the circulation. Here the energy is concentrated basically in two distinct eastward-propagating modes: one of very low frequency ($0 < \omega < 0.1$ cycles-per-day) and another one with higher frequency ($0.4 < \omega < 0.6$ cycles-per-day). These two main modes are in line with those derived by the EOF analysis in Chapter 3 and analyzed to some extent in section 3.3.5.

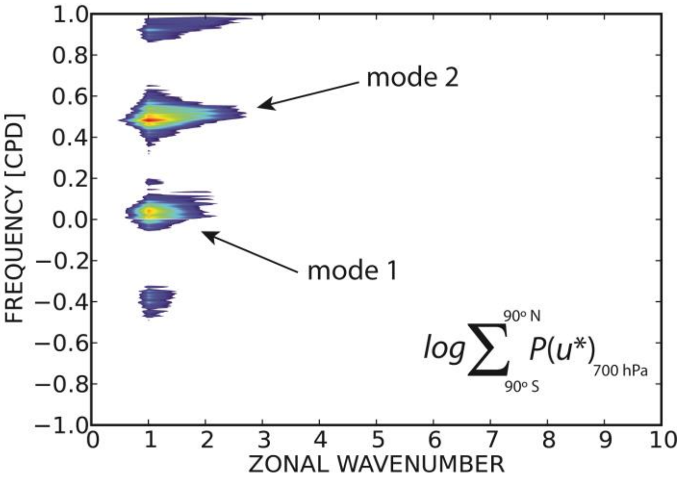

Figure 4.6 – Frequency versus zonal wavenumber plot of the logarithm of the power spectrum of the nonaxisymmetric component of the zonal wind ($m^2\ s^{-2}$, shaded) computed for the superrotating regime at 700 hPa level and summed for all latitude circles. Values are plotted from 3.7.

In order to isolate each mode, filtering was applied by computing space-time Fourier transforms of the wind and geopotential height fields over the entire domain. Then the coefficients of the Fourier transform with wavenumber one and frequencies lying within the frequency bands described before were truncated. After that, another transformation back to the physical space was applied giving gridded fields of wind (u^*, v^*) and geopotential height (h^*) for each wave mode. Time and zonal means of eddy variables are zero by definition; however the variance, given by the product of the variable with itself, is non-zero. Based on this property, the latitudinal structure of the modes were mapped though the time- and zonal-mean variance of geopotential height $\overline{[h^{*2}]}$ and the wind components, $\overline{[u^{*2}]}$ and $\overline{[v^{*2}]}$ and they are depicted in Figure 4.7.

The mean meridional structure of the wave mode 1 is characterized by a strong peak of geopotential height at the extratropics in both lower- and higher-levels of the troposphere (Figure 4.7a). Although the intensity of the wave's signature increases with height, the maxima tend to be aligned in the vertical indicating a barotropic structure. The patterns of both zonal and meridional wind components indicate a gyre-shape circulation close to the peaks of geopotential with stronger circulation poleward the vortex. Following the vertical variation of the geopotential variance $\overline{[h^{*2}]}$, stronger winds are found in higher-levels as well (Figure 4.7a). The wave mode 2, on the other hand, has a more complex structure (Figure 4.7b). Differently from mode 1, mode 2 presents signatures in both tropical and extratropical regions, though its pattern changes from lower to higher levels. In 700 hPa the strongest signature of the geopotential variance is located at the higher latitudes, while within the tropics a small signature height is observed. The patterns of $\overline{[u^{*2}]}$ and $\overline{[v^{*2}]}$ suggest the existence of a weak hemispherically-symmetric vortex structure in the topics, and a stronger counterpart in higher latitude (Figure 4.7b). In 250 hPa, however, the tropical signature dominates the zonal mean variance while the extratropical projection becomes very small. Besides, the peaks of the geopotential variance are shifted toward the poles, indicating an expansion of the meridional extention of the tropical disturbances aloft. As in 700 hPa, the wind component variances still indicate a gyre-shape for both tropical and extratropical signatures, albeit slight differences in the latitudinal position and intensity of the peaks are found.

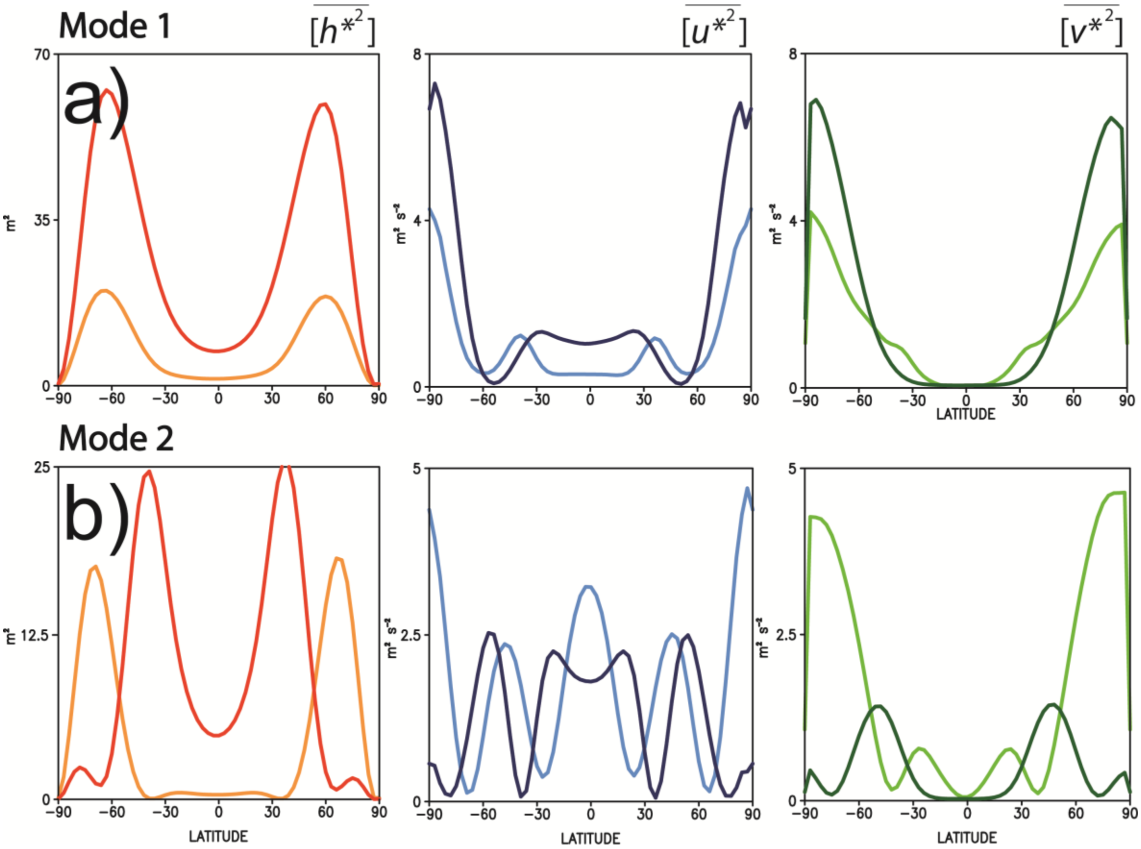

Figure 4.7 – Time- and zonal-mean of the variance of the filtered geopotential height (m^2) and wind components (m^2 s^{-2}) for: a) wave mode 1 (k = 1, $0 < \omega < 0.1$ cycles-per-day), and b) wave mode 2 (k = 1, $0.4 < \omega < 0.6$ cycles-per-day). The wave structures are given for the vertical pressure levels of 250 hPa (darker colors) and 700 hPa (lighter colors).

Based on the characteristics of wind and geopotential height distributions in both vertical levels it was possible to reconstruct the mean spatial structure of the main modes present in the superrotating atmosphere. In Figure 4.8 the latitudes of ϕ_{E}, ϕ_{T} and ϕ_0 indicate, respectively, the position of the wave maxima signature in the extratropics and tropics, and the meridional extension of the tropical wave guide associated with the tropical projection of the mode 2.

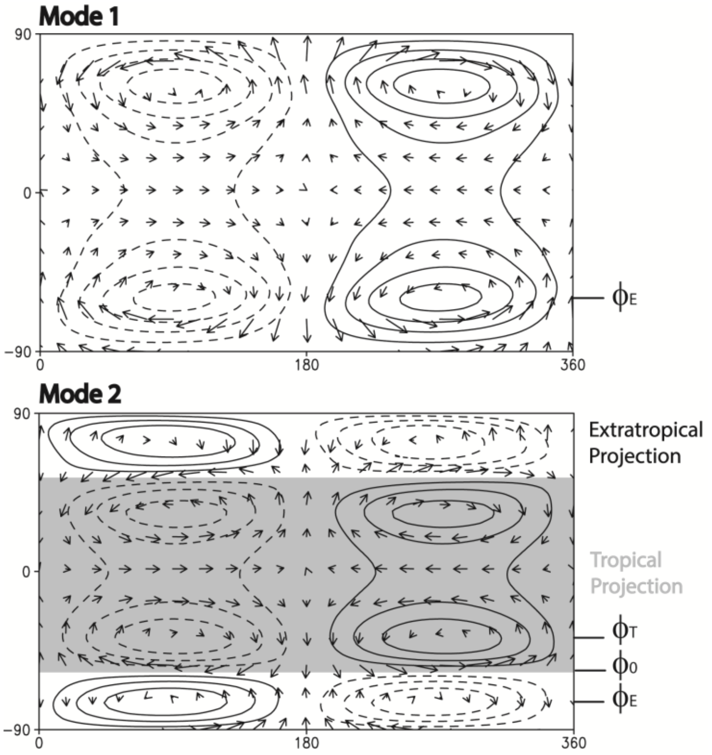

Level	700 hPa		250 hPa	
Latitude	Mode 1	Mode 2	Mode 1	Mode 2
ϕ_T	n/a	21°	n/a	39°
ϕ_0	n/a	36°	n/a	66°
ϕ_E	60°	69°	60°	78°

Figure 4.8 – Averaged spatial structure of the geopotential height and wind associated with wave mode 1 and wave mode 2. Although the scales are arbitrary, the intensity of the extratropical and tropical portions of the waves changes with height. ϕ_E and ϕ_T indicate the latitudes where the extratropical and tropical projections have their maximum amplitude; ϕ_0 delimits the meridional extension of the tropical wave guide for mode 2. See text for more details.

The slowly-propagating mode 1 is basically composed by a planetary scale Rossby wave with peaks of geopotential and winds located in the extratropics (Figure 4.8). Although the intensity of the wave enhances with height, as shown in Figure 4.7a, the peak of the geopotential associated with the gyres in the low- and high-pressure centers of the wave train remained at about the same latitude of 60°. Analysis based on EOF and potential vorticity distribution conducted in sections 3.3.4 and 3.3.5 had indicated that mode 1 is barotropic, which is in line with vertically stacked nature in height of the vortex tube described here. The faster-propagating mode 2 has a diverse structure combining both tropical and extratropical elements. This mode is comprised by a global scale equatorial Rossby wave with a hemispherically-symmetric extratropical projection. Such a signature at the equatorial region resembles that found for Matsuno (1966) shallow water equation solutions for the n = 1 equatorial waves, with pairs of cyclones and anticyclones centered at the equator. While the tropical signature is strengthened with height, as depicted in Figure 4.7b, the extratropical projection is much weaker at upper levels. Moreover, there is a considerable meridional variation of the wave guide width between low- and high-levels. As shown in table of Figure 4.8, there is a variation of about 30° in the meridional extension, indicating that the Rossby wave is less equatorially-trapped in higher- than lower–levels of the atmosphere. These variations in width and position of the vortex in the latitudinal plane are consistent with a baroclinic nature of the mode 2, as suggested by the potential vorticity analysis of Chapter 3.

Much of the spatial structure depicted in Figure 4.8 can be described in terms of the effects of the basic state wind shear on the waves, especially for those with tropical nature. According to several authors, the sense of the basic state wind and both its vertical and meridional shear have significant impact on the Rossby wave modes. Figure 4.9 shows the time- and zonal-mean distribution of the zonal wind component u in both vertical and meridional planes. In this superrotating regime, the prograde zonal wind increases with height reaching its maximum in 250 hPa, then decreasing again aloft. Although $\partial[\bar{u}]/\partial z > 0$ throughout the atmosphere, the basic state has a more intense shear in the tropical zone, between 30° S – 30° N, than in the extratropics. On the meridional plane, stronger shear is found on the poleward flanks of the jet in 250 hPa. In700 hPa, however, winds are weaker and small shear occurs.

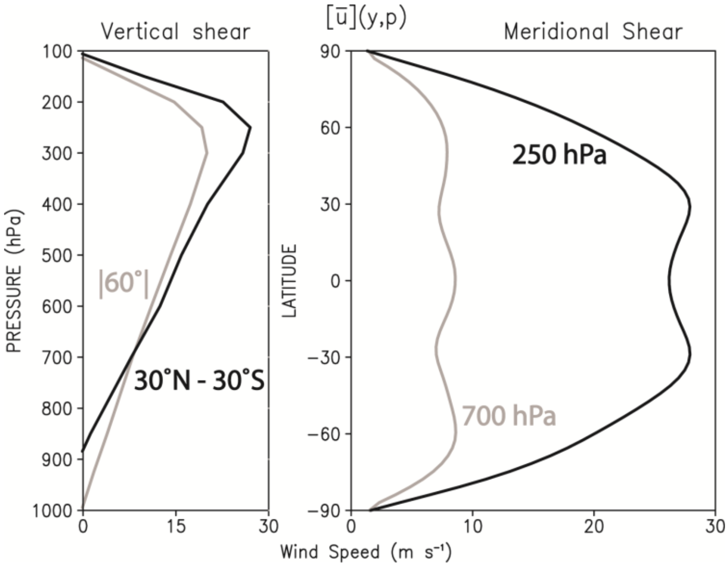

Figure 4.9 – Time- and zonal-mean distribution of the basic state zonal wind (contour, m s^{-1}) in the vertical plane (1000 – 100 hPa) averaged over the tropical zone and the extratropics; and in the meridional plane taken in 700 and 250 hPa.

According to Zhang and Webster (1989), a westerly basic state flow leads to a weaker equatorial trapping of Rossby waves and increases their autofrequencies.

Besides, Rossby waves propagating embedded in a prograde zonal flow extend their influence toward the extratropics. In fact, for the baroclinic wave mode 2 (Figure 4.7b and 4.8), a wide meridional extent of the equatorial wave guide was observed, increasing at higher levels of the atmosphere where the equatorial westerly jet is stronger, and occupying a much larger portion of the globe, compared with its lower-level counterpart. The fact that the meridional shear becomes important only toward higher latitudes (Figure 4.8) is relevant here for the mode 2 dynamics. Boyd (1978) pointed out that only $n = 1$ equatorial Rossby waves with a wide meridional extention will be affected by the meridional wind shear. Additionally intense meridional shear of the mean flow induces tight trapping of rotational waves (Rossby waves are mostly rotational) near the equator and does not favor baroclinic instability in the tropical zone (XIE; WANG, 1996). Therefore since the wave mode 2 is wide in the meridional plane, a situation of stronger meridional shear in the tropical zone would not only affect its structure but also its dynamics, by reducing its meridional extension and suppressing the baroclinic instability.

Wang and Xie (1996) have shown that a pure equatorial Rossby wave has its properties altered under a situation of positive vertical shear, exhibiting stronger signature in the upper atmosphere and an extratropical projection in higher latitudes. By comparing Figure 8a from their study with Figures 4.7b and 4.8, it is possible to observe that similar changes happened in the wave mode 2, and thus a vertically shearing basic state flow has a deeper impact on the equatorial Rossby waves in a superrotating state. The authors have also indicated that a barotropic Rossby wave in a presence of vertical shear extends toward the poles, with maximum of the winds and geopotential occurring in the extratropics. The maximum signature of the barotropic wave mode 1 around 60° of latitude is the effect of the existence of this vertical wind shear (Figure 4.7a and 4.9). Moreover, both modes have their amplitude increased with height, which is another consequence of the existence of the westerly wind shear. The Rossby modes respond sensitively to the meridional variations of the vertical westerly shear (Figure 4.9), suggesting that the responses are enhanced where this shear is strengthened and the local shear is important for the *in situ* modification of the modes properties (WANG; XIE, 1996).

4.3.3b. Temporal behavior of the filtered modes

In the last section our interest relied on the averaged time- and zonal-mean meridional structure of the two main wave modes in the superrotating state. However, some aspects of the temporal behavior of the geopotential height time series described in section 3.3.5 from Chapter 3 had indicated that these two modes underwent significant changes of the their amplitude through time. Therefore, in this section, the temporal behavior of the wave modes will be explored in more details.

Previous analysis of the whole data set (not shown) revealed that, apart from the natural oscillation of the waves, there are substantial changes of their amplitudes during sporadic periods of time. Based on the time changes of mode 1 two different behaviors, named the periodic and non-periodic one, were identified. Figure 4.10 shows the time series of the geopotential height h^* in two selected periods of time for both wave mode 1 and 2 in order to illustrate these two different behaviors.

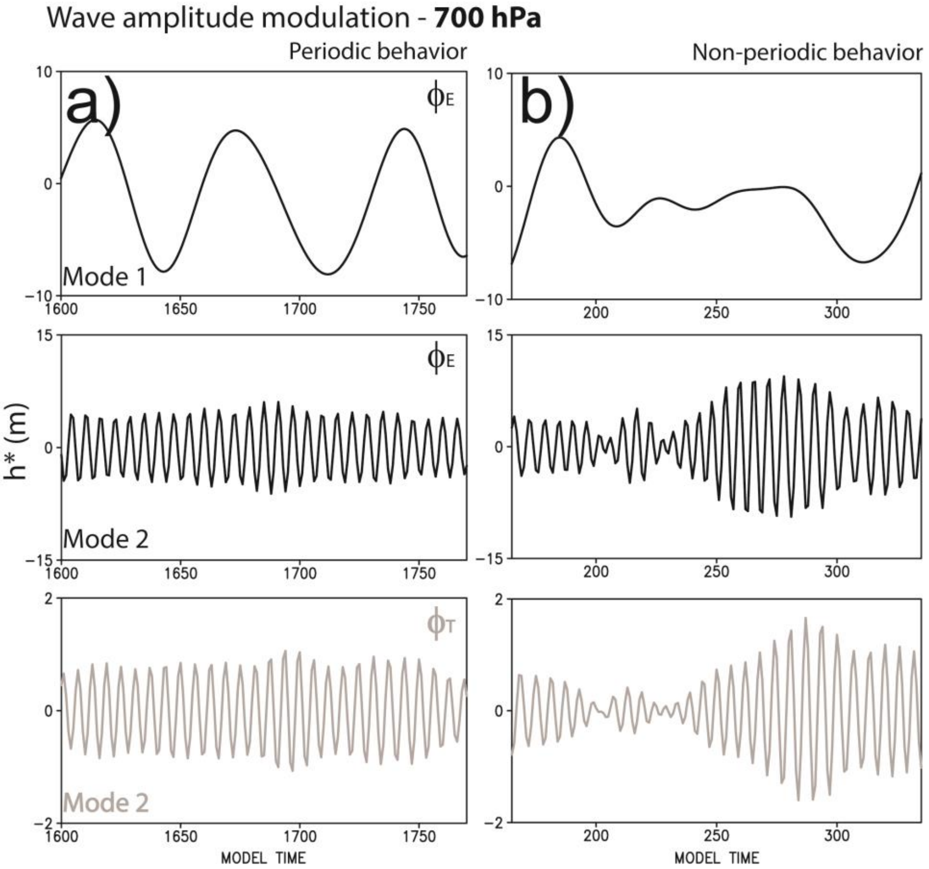

Figure 4.10 – Time series of the geopotential height (m) taken at the specific latitudes where the mode have their maxima amplitude and at 700 hPa where the convergence of momentum by the eddies is maximized: a) during the period of the periodic behavior and b) during the period of the non-periodic behavior. Although just two periods of time have been displayed here, such patterns are found throughout the whole data. See table in Figure 4.8 for more details about the chosen latitudes.

Based on Figure 4.8, the temporal series were taken at the latitudes ϕ_{E} and ϕ_{T}, and at longitude $\lambda = 0°$ and pressure-level $p_0 = 700\,\mathrm{hPa}$. This vertical level was chosen because most of the eddy momentum fluxes in the equatorial region were produced at this level (Figure 4.4b). During the periodic behavior period (Figure 4.10a), the amplitude of the geopotential height oscillates regularly according to the respective frequency bands of each wave mode. On the other hand, during the non-periodic behavior period (Figure 4.10b) this regular oscillation is not observed. Mode 1 practically vanishes for more than 30 model days, and during this time, firstly, mode 2's amplitude abruptly decreases and then reaches values twice bigger than those observed during the periodic behavior. It is possible to observe that there is some kind of modulation of the amplitudes of both tropical and extratropical projections of wave mode 2 when wave mode 1 disappears, suggesting that wave mode 1 affects mode 2 during certain periods of time.

In order to illustrate the changes in the wave structure during these two periods of time, Figures 4.11 and 4.12 show the distribution of winds and geopotential height associated with the two modes, for 250 and 700 hPa in different times of these two periods. Besides, along with the spatial patterns, plots of acceleration based on the convergence of the eddy momentum fluxes generated by each mode are shown.

Figures 4.11a,b and 4.12a,b depict the two wave modes during the period of regular propagation of the waves. Their amplitudes remained the same as the wave trains propagated from west to the east of the domain. Two general aspects are worth noticing; first, the convergence of momentum at the equatorial region displayed in Figure 4.4b, and its consequent acceleration of the zonal wind within this region, is produced by the wave mode 2 at lower levels (Figure 4.12b), whereas some acceleration is produced by mode 1 around 30° of latitude (Figure 4.12a). These findings agree with the results from section 3.3.4, in which only one mode (given by the 3^{rd} and 4^{th} EOF mode) was responsible for the acceleration in the equatorial region. Second, there is a clear meridional tilting in the axis of the gyres associated with the equatorial Rossby wave train. Such a pattern observed for mode 2 is consistent with the equatorward transport of momentum as displayed in Figure 4.3, Figure 4.4b and the spectral analysis (Figure 4.5c) and does not change during the entire period (model time 1634 to 1736).

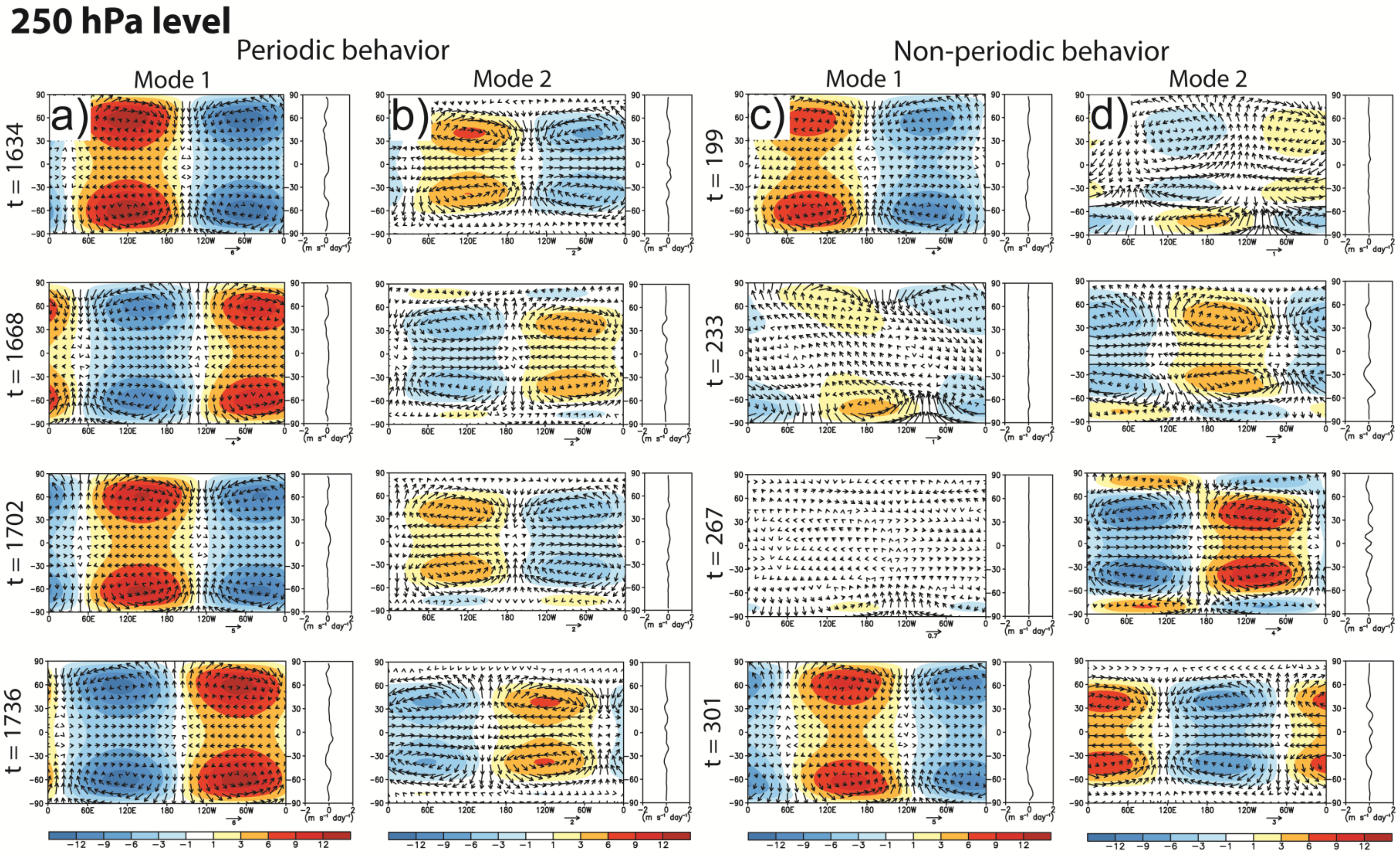
250 hPa level
Periodic behavior
Non-periodic behavior
Mode 1
Mode 2
Mode 1
Mode 2
a)
b)
c)
d)
t = 1634
t = 1668
t = 1702
t = 1736
t = 199
t = 233
t = 267
t = 301
90
60
30
0
−30
−60
−90
0
60E
120E
180
120W
60W
0
−2
2
(m s⁻¹ day⁻¹)
−12
−9
−6
−3
−1
1
3
6
9
12

Figure 4.11 – Geopotential height (shaded, m), horizontal wind (vectors, ms^{-1}) and eddy momentum flux convergence (contour, m s^{-1} day^{-1}) associated with the two wave modes during the periods of the: a), b) periodic behavior (model times 1634, 1668, 1702 and 1736) and c), d) non-periodic behavior (model time 199, 233, 267 and 301) at 250 hPa.

According to Xie and Wang (1996), some distinct characteristics in wave structure can be observed between baroclinically unstable and stable equatorial Rossby waves. The authors pointed out that unstable equatorial Rossby waves present latitudinal tilting of their phase lines and more trapping in the equatorial region. These ideas are in line with the findings here; at 250 hPa mode 2 has symmetric gyres and consequently there are neither net eddy momentum fluxes nor accelerations. At 700 hPa, on the other hand, there is meridional tilting in the wave and then non-zero equatorward momentum fluxes are generated. Besides, apart from the effects of the shearing basic state itself mentioned in the last section, wave mode 2 is much less trapped in the equatorial region at 250 hPa than its counterpart at 700 hPa, reinforcing that wave mode 2 is baroclinically unstable in low levels

During the period of the non-periodic behavior (Figures 4.11c,d and 4.12c,d) both shape and amplitude of geopotential height and winds are drastically changed as the waves propagate toward east. At model time 199, the spatial structure of wave mode 1 and 2 was already altered most in the lower-levels of the atmosphere. Both modes are weaker if compared with their patterns during the periodic behavior period (Figures 4.11a,b and 4.12a,b). As the time passed by, the vortex associated with the extratropical Rossby wave train of wave mode 1 decreased radically, while wave mode 2 started enhancing again. At time 267 wave mode 1 almost vanished, while wave mode 2 was strengthened. Finally at time 301, wave mode 2 was much stronger than during the regular period (compare with time 1739 from Figure 4.11b and 4.12b) in both upper- and lower-levels. At this same period wave mode 1 reappears and starts enhancing again. Although this description is limited to only two periods of time, this behavior occurred systematically through the whole 3 years of data, although the duration of the period in which wave mode 1 vanished varied from one non-periodic period to another one (Figure not shown). These repeated variations of amplitude therefore might indicate that there is a potential interaction between the two wave modes in short periods of time. Moreover the dynamics between these two different periods may be possibly different, not only because the waves change their amplitude but also because the content of energy associated with these modes also changes. The next section will investigate the energetic processes in the superrotating atmosphere in order to verify the exchange of energy between the mean flow and the waves, and their interactions.

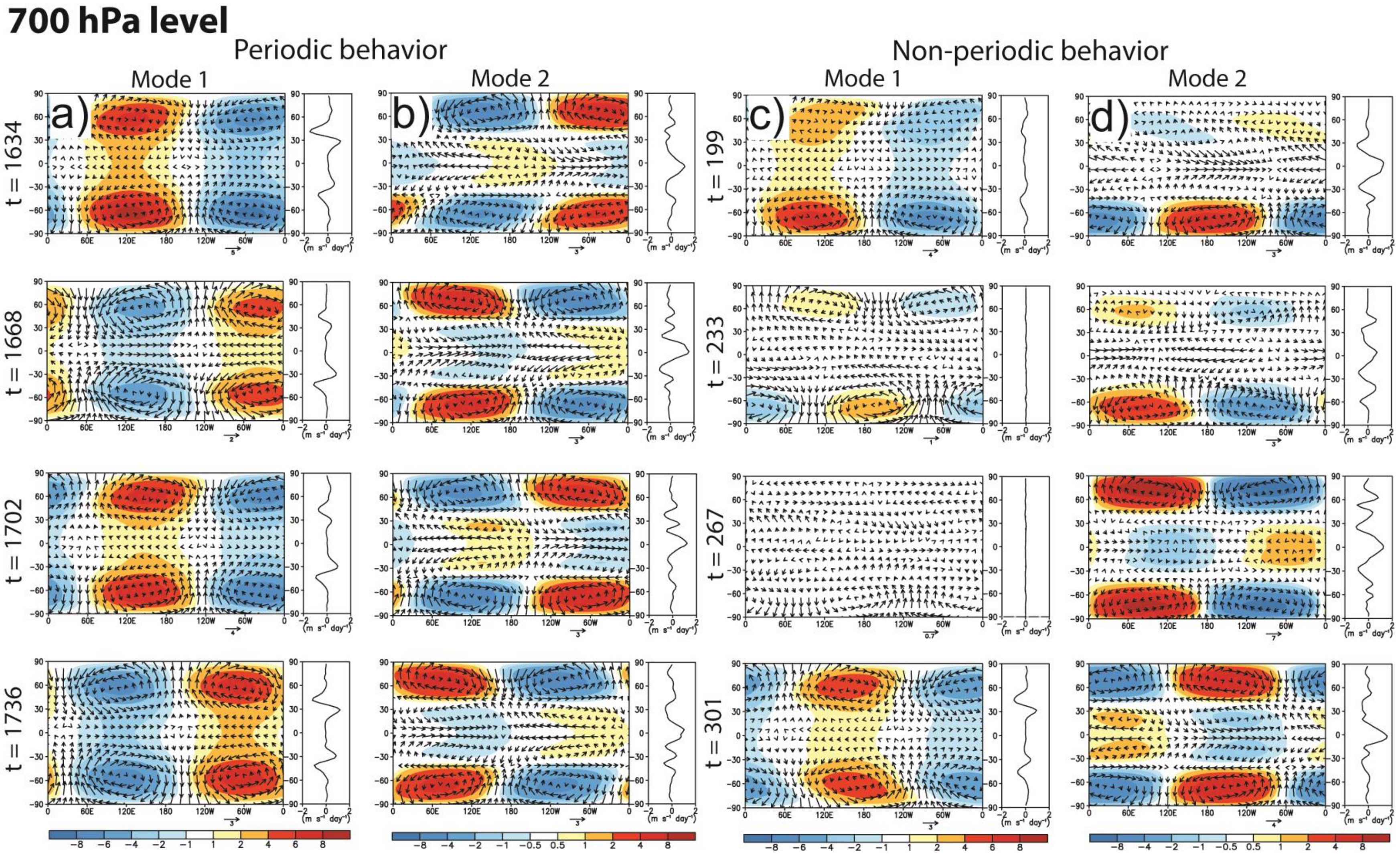

Figure 4.12 – Same of Figure 4.11 but for 700 hPa.

4.3.3c. Interactions among the basic state and the eddies

Based on the equations of the Lorenz energetics (eqs. 4.7 – 4.26), there is a clear separation between the physical processes associated with the basic state and eddies. If eddies are treated as if they were disturbances superimposed over this basic state, i.e. departures of the zonal mean, and if they were as a linear sum of different wave modes possessing different frequencies and wavenumbers, the contribution of each mode to the energy cycle could be analyzed separately. Thus the total energy cycles for the two modes were computed separately, i.e., the energetic processes between the basic state and wave mode 1, and the basic state and wave mode 2. By doing so, there is a more clear representation of the interaction between each mode and the basic state.

Figure 4.13 describes the Lorenz energy cycle averaged for the entire period of the model output. Since for long periods the total energy of the atmosphere is neither decreasing nor increasing deliberately, its time change can be considered zero, and therefore the generation and dissipation terms could be computed as residuals of eqs. (4.7) – (4.10). The superscripts (0), (1) and (2) were defined to refer to the basic state, or the zonally-averaged flow, wave mode 1 and wave mode 2, respectively. Although the description of the energetics in the section 4.2.3 is related to the Earth dynamical regime, here a parallel between the physical mechanisms that represent each conversion for the superrotating regime is presented.

The available potential energy is generated basically trough the G_Z term, which is parameterized by the relaxation thermal profile in the Held-Suarez diabatic forcing (see Figure 2.3a and eq. 23 in Chapter 2) in such a way that there is surplus of energy at the tropical regions and deficit at higher latitudes. This heating leads to the generation of the mean overturing circulation Hadley cell which converts part of A_Z into K_Z ($C_Z^{(0),(0)}$ is positive and strong). The lower part of the energy diagram (Figure 4.13) involves the interaction between the mean flow and the wave modes described in the section 4.3.3a. In average, the conversion terms related to the baroclinic chain (C_A and C_E) are stronger for the wave mode 2. Here part of the available potential energy of the basic state is converted by $C_A^{(0),(2)}$ into available potential energy of the wave mode 2 and then it is transferred to the disturbance as kinetic energy ($C_E^{(0),(2)}$). The structure of the equatorial unstable wave is such that it favors the conversion $A_Z \rightarrow A_E$ (XIE; WANG, 1996), which indicates baroclinic conversion, and therefore acts in order to maintain the existence of this mode. The $C_K^{(2),(0)}$ term is very small compared to other terms but its positive value indicates transfer of kinetic energy from eddies to the mean flow. The barotropic term is more important for the wave mode 1, in which $C_K^{(1),(0)}$ is, in average, negative indicating that part of the energy of the mean flow is transferred to the disturbance. This indicates that barotropic instability operates to maintain this wave mode, also confirming the analysis in the last section. The dissipation terms (D_Z and D_E) are both positive, completing then the cycle, with friction removing kinetic energy from the motion.

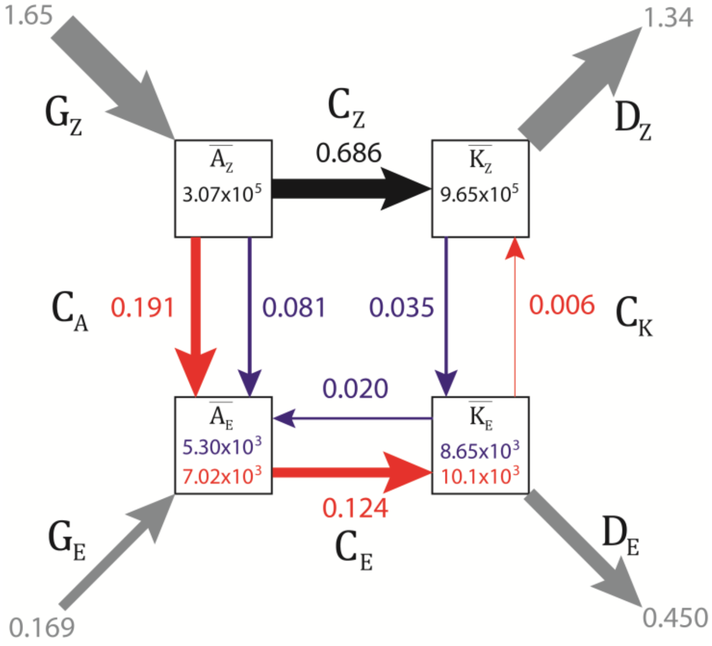

Figure 4.13 – Diagram of the total Lorenz energy cycle for the superrotating atmosphere. Here we split the energy cycle envolving the basic state and wave mode 1 (blue colors) and the basic state and wave mode 2 (red colors). The generation and dissipation terms (grey colors) are computed as residual values from the eqs. (4.7) – (4.10). The black color refers to only terms related to the basic state quantities (see text for more details). The energy amounts are given in J m^{-2} and the other terms are given in W m^{-2}.

Figure 4.14 shows the time evolution of the vertically-integrated total energy and the conversions during the periods of periodic and non-periodic behavior. The total energy is defined as the sum of the available potential energy and the kinetic energy, thus we have $E^{(0)} = A_Z + K_Z$, for the basic state, $E^{(1)} = A_E^{(1)} + K_E^{(1)}$, for the wave mode 1, and finally $E^{(2)} = A_E^{(2)} + K_E^{(2)}$ for the wave mode 2. In order to illustrate the relative role of barotropic and baroclinic instabilities during these two periods, we limited our attention just to the time changes of the conversion terms C_E and C_K.

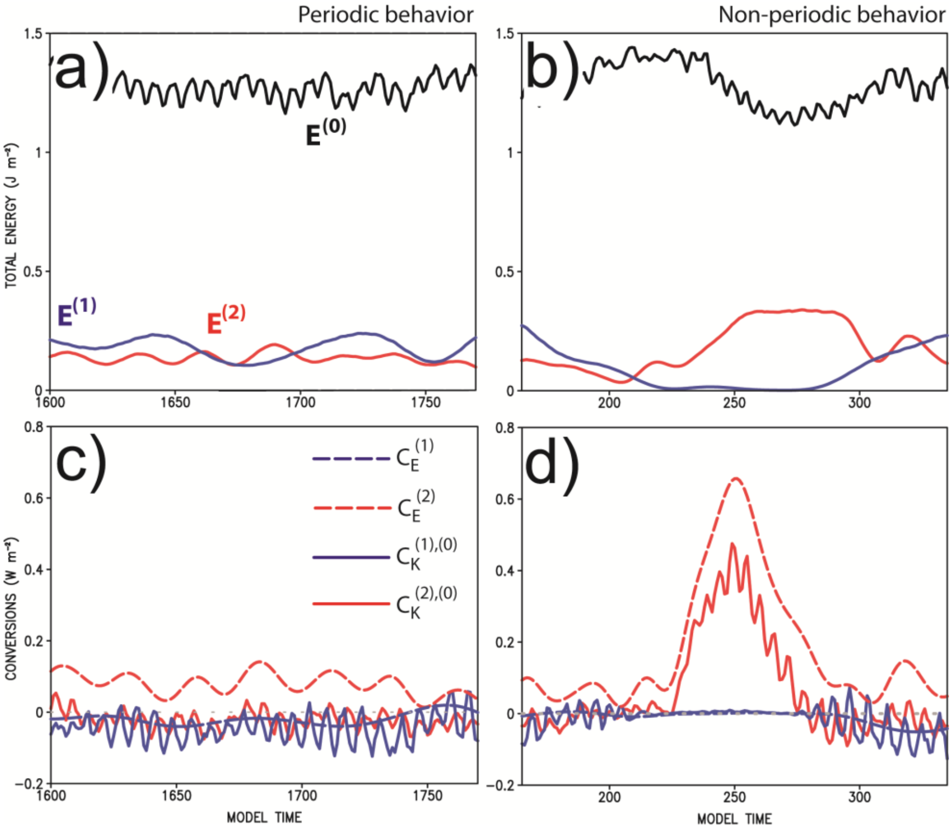

Figure 4.14 – Vertically integrated energy (x10^5 J m^{-2}) and conversion terms (W m^{-2}) for the periodic and non-periodic behaviors: a) and b) total energy of the basic state, wave modes 1 and 2; c) and d) baroclinic C_E and barotropic comversion C_K. The subscripts (0), (1) and (2) are related to the basic state (black lines), wave mode 1 (blue lines) and wave mode 2 (red lines), respectively (see text for more details).

During the periodic behavior, apart from the fluctuation of the basic state and both wave modes energies, the averaged energy of these components remained nearly constant (Figure 4.14a). Both modes have almost the same energy amount, although wave mode 1 has a more pronounced variation of the amplitude. The non-periodic behavior, on the other hand, presents a distinct temporal variation (Figure 4.14b). As mentioned in the last section during these periods there is a marked difference of the wave structure and its evolution, which is evident here in different temporal variation of the energy contents. Wave mode 1 reached almost zero energy after model time 200, meaning that it had been dissipated. When that happened wave mode 2 grew, maintaining for a considerable period of time a total energy bigger than 0.25 J m^{-2}, which was more than twice its mean value during the periodic behavior (Figure 4.14b). In addition to to these variations, the basic state also shows a marked decrease of energy after mode 1 vanished, reaching its minimum when mode 2 reached its maximum, and then increasing again at model time 300.

In general, during the periodic behavior (Figure 4.14c) the conversion terms $C_E^{(1)}$ and $C_K^{(2),(0)}$ are on average almost zero, whereas $C_E^{(2)}$ and $C_K^{(1),(0)}$, although small, are active during the whole period. This indicates that the positive values of term $C_E^{(2)}$ express conversion of eddy available potential energy related to wave mode 2 into kinetic energy of this mode. In opposition, the averaged negative values of $C_K^{(1),(0)}$ represents the transfer of the basic state kinetic energy to the kinetic energy associated with the wave mode 1. Such a general behavior during the periodic behavior period is very similar to the total averaged energy cycle in Figure 4.13. During the time interval of the non-periodic behavior when mode 1 disappeared, there is a strong signal related to wave mode 2 (Figure 4.14d). The conversion terms related to wave mode 1 decrease toward zero, and those related to the wave mode 2 reach their maximum values. Between model time 225 – 275, the conversion terms $C_E^{(2)}$ and $C_K^{(2),(0)}$ are positive and strong (0.7 and 0.5 W m^{-2}), both indicating maxima of the transfer of energy $A_E^{(2)} \rightarrow K_E^{(2)} \rightarrow K_Z$. This indicates that available potential energy related to wave mode 2 is being converted into kinetic energy to the disturbance itself, and then this kinetic energy is transferred to the mean flow. The increase of the total energy of $E^{(2)}$ follows the increase of $C_E^{(2)}$, although the peaks are not in phase in time. When the term $C_K^{(2),(0)}$ acquires its maximum, the energy of the basic state $E^{(0)}$ starts increasing again, which indicates the maintenance of the mean flow by the wave mode 2. This analysis shows that during these sporadic periods in which wave mode 1 vanishes and wave mode 2 reaches its maximum strength, there is net transfer of kinetic energy from the wave mode 2 to the mean flow. At this short period, baroclinic instability is the major driver of the superrotation. Newman et al. (2011) by analyzing the superrotation in a full Titan 3D GCM noticed maintenance of the superrotation in, what they called, short and episodic angular momentum transfer events, indicating that during the steady state the atmosphere experinced short periods of instability. Their findings agree with the existence of the non-periodic behavior period in which massive transfer of the kinetic energy to the mean flow is found in short and sporadic intervals of time. Since atmospheres in higher Rossby number regimes have a more barotropic thermal structure (see for example WILLIAMS, 1988a,b; NAVARRA; BOCALLETTI, 2002), it is natural to attribute the dynamical driver of superotation to disturbances originated from barotropic instability (HOURDIN et al., 1995; WILLIAMS, 2003; LUZ; HOURDIN, 2003; NEWMAN et al., 2011). However, it is possible that baroclinic instability can be also a candidate, as the results suggest, if it occurred within a shallow region of the lower atmosphere with stronger temperature gradients during these sporadic periods of non-periodic behavior.

To illustrate this aspect, Figure 4.15 shows for the three analyzed years the zonal mean zonal wind in 250 hPa averaged between 30° S – 30° N, the $C_K^{(2),(0)}$ conversion, and the averaged thermal contrast and vertical wind shear in mid-latitudes. The thermal contrast was measured by the difference of the zonal- and time-mean temperature $[\bar{T}]$ averaged between two distinct latitude bands (50° - 75°, and 75° - 90°) at 925 and 400 hPa. The difference of zonal winds $[\bar{u}]$ between 300 hPa and 925 hPa at 75° of latitude was used to measure the strength of the vertical shear. The general behavior of the time series shows that there is a tendency for systematic kinetic energy transfers from the wave mode 2 to the basic state during periods in which the mean velocity of the superrotating equatorial jet reached smaller values (Figures 4.15a and 4.15b). These periods of non-periodic behavior, when all the dynamics described before take place, present strong increase of baroclinicity restricted in the lower level of the atmosphere, reaching differences of more than 3 K and with peaks of 6 K during the stronger events (Figure 4.15c). Following the enhancing of the latitudinal temperature contrasts in lower levels, intense increasing of the vertical wind shear is also observed during the stronger episodic instability events (Figure 4.15d).

The increase of vertical shear seemed to have a profound influence on the equatorial Rossby waves, since it can couple both barotropic and baroclinic modes in such a way that the baroclinic Rossby mode force the barotropic mode as the literature suggests (WANG; XIE, 1996). Besides, the vertical wind shear allows sufficiently fast non-linear energy exchange between mid-latitudes and the tropics through the interaction between barotropic extratropical and baroclinic equatorial Rossby waves as reported in Majda and Bielo (2003). Additionally Reznik and Zeitlin (2009) showed that the equatorial wave guide with a mean baroclinic current (i.e. positive vertical shear) acts as resonator, and responds to barotropic waves by making baroclinic equatorially-trapped Rossby modes grow, which later are nonlinearly saturated and stop growing.

In contrast, other processes could be behind the origin and time evolution of the Kelvin-Rossby coupling in Venus. Literature suggests that energy fluxes from mid-latitudes laterally forcing Kelvin waves (DEL GENIO; ROSSOW, 1990), mixed source of energy from the hydrodynamic instabilities (MITCHELL; VALLIS, 2010) or planetary ageostrophic instabilities (PENG; MITCHELL, 2014) might be candidates for this kind of wave coupling.

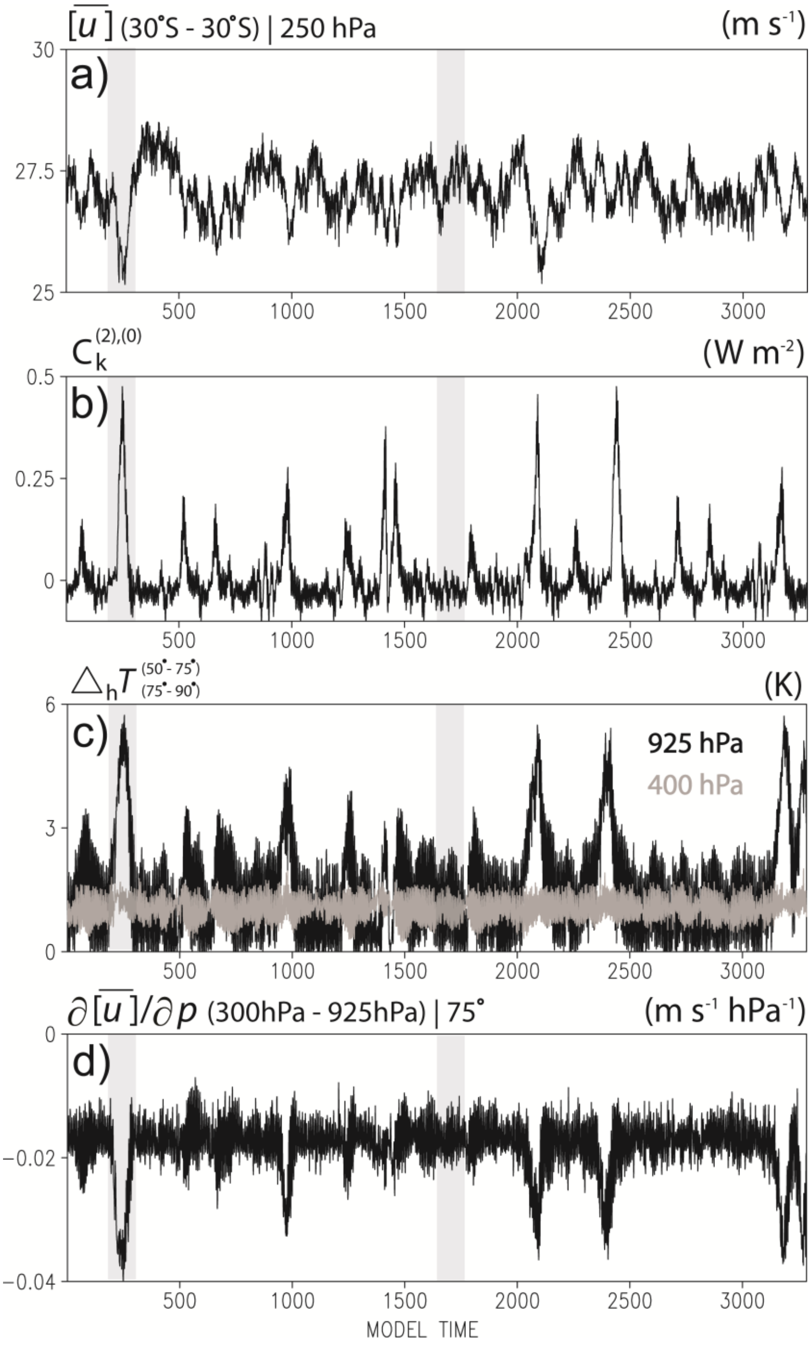

Figure 4.15 – Kinetic energy transfers and baroclinic instability during three years of simulated steady-state. a) Zonal mean zonal wind (m s^{-1}) in 250 hPa averaged in the tropical region, b) The conversion of the wave mode 2 eddy kinetic energy into basic state kinetic energy (W m^{-2}), c) Time- and zonal-mean temperature difference between the latitude circles of 50° - 75° and 75° - 90° computed at the levels of 925 hPa (black line) and 400 hPa (grey line). d) Time- and zonal-mean zonal vertical wind shear (m s^{-1} hPa $^{-1}$) taken at the latitude of 75°. The grey box on the plots indicates the location within the total data set where the periods of periodic and non-periodic behavior are analyzed in the thesis.

Although the Lorenz formulation is unable to represent the transfer of energy among waves, such a mechanism of exchange could be an important mechanism of energy redistribution for these large scale equatorial waves (DOMARACKI; LOESCH, 1977). The general combined behavior of the wave modes suggests that non-linear interactions between the barotropic and baroclinic Rossby waves are likely possible to be present in the superrotating atmosphere since modulation of their amplitude was noted during the non-periodic behavior period, and possibly energy exchange between these modes occurred. During the episode of periodic behavior, on the other hand, the energy transfer was absent, the mean flow was more stable and both thermal contrast and wind shear were weaker and quasi constant in time.

4.4. Discussion

Without considering the effects of the mean meridional overturning circulation, it was presented a comprehensive study of the three dimensional structure and dynamics of the waves controlling the eddy momentum fluxes that maintain the strong, long-lived superrotating state in a higher Rossby number regime atmosphere. In order to reproduce the dynamical regime found in a slow-rotating body, such as Venus and Titan, a simulation in an idealized GCM with reduced planetary radius was performed.

In the superrotating numerical experiment, equatorward momentum fluxes were produced mostly in the lower level of the atmosphere where frictional effects are important. Spectral analysis applied on this region revealed that the eddy component of the general circulation is comprised of two global-scale wavenumber one modes: a slow-propagating, barotropic extratropical Rossby wave and a fast-propagating, baroclinic tropical equatorial Rossby wave. Since they are global in dimensions it is unlikely that either meridional or vertical propagation of these modes could occur and therefore, the idea of the linear model based on critical latitudes of absorption is not sufficient to explain the eddy momentum flux distribution, and consequently the wave-mean flow interaction in this regime. Filtering analysis provided a better picture of the tridimensional structure of these modes and it indicated that equatorward momentum fluxes were generated mostly by the equatorial Rossby wave due to meridional tilting in the axis of the gyres associated with the wave train. In addition, the positive time- and zonal-mean vertical wind shear had a profound impact on the structure and dynamics of these waves by changing their intensity and meridional extension, with less equatorial trapping, and vertical structure.

The dynamical maintenance of superrotation was basically due to the interplay between Rossby wave modes in sporadic periods of stronger instability. Analysis of the time evolution showed two distinct behaviors throughout the whole period of study. In the first one, named periodic behavior, the amplitude of the waves remained almost unchanged as the wave trains propagated from west to east. During this period the basic state mean flow was constant and both thermal contrast and wind shear values did not present great variations. In the second regime, termed non-periodic, both wave modes underwent abrupt changes of amplitude, so the tropical mode grew while the extratropical mode almost vanished. The modulation of their amplitude suggested possible non-linear interaction between these two wave modes during these periods of non-regular propagation. During this period the basic state showed a decrease in its total energy.

The Lorenz energetics indicated that the massive transfer of kinetic energy from the waves to the mean flow occurred just during the short periods of non-periodic behavior. The equatorial superrotating flow was maintanined at the expense of the eddy kinetic energy from the equatorial Rossby wave excited through baroclinic instability. Inspection of the averaged thermal contrast and vertical wind shear indicated that the action of the baroclinc instability at this dynamical regime is more sporadic in nature and acts on a shallow layer of the atmosphere, but with effects in the whole three dimensional structure of the waves and mean basic state. Barotropic instability, on the other hand, was found to be important in providing kinetic energy to the extratropical Rossby wave at higher latitudes. The systematic amplitude changes of these modes during the non-periodic behavior possibly suggest non-linear energy exchange between the two wave modes, which could indicate non-linear eddy-eddy processes coupling them.

CHAPTER 5.

Final discussions and beyond

This thesis has been devoted to study the dynamics of the atmospheric superrotation based on a set of idealized numerical experiments run in a regime of higher Rossby number (*R*o). The regime achieved in the superrotating simulation was characterized by a *R*o with order of magnitude about 100 times bigger than Earth-related values. In such a condition the general circulation of the atmosphere possessed different elements from an Earth-like one; the existence of a predominately zonal circulation at almost all levels of the atmosphere with a faster westerly equatorial jet was one of the most striking distinctions between the two atmospheric circulations (Figure 5.1). The meandering subtropical jets in Earth regime were replaced by a more uniform wind distribution, and the overturning Hadley cell became meridionally wider.

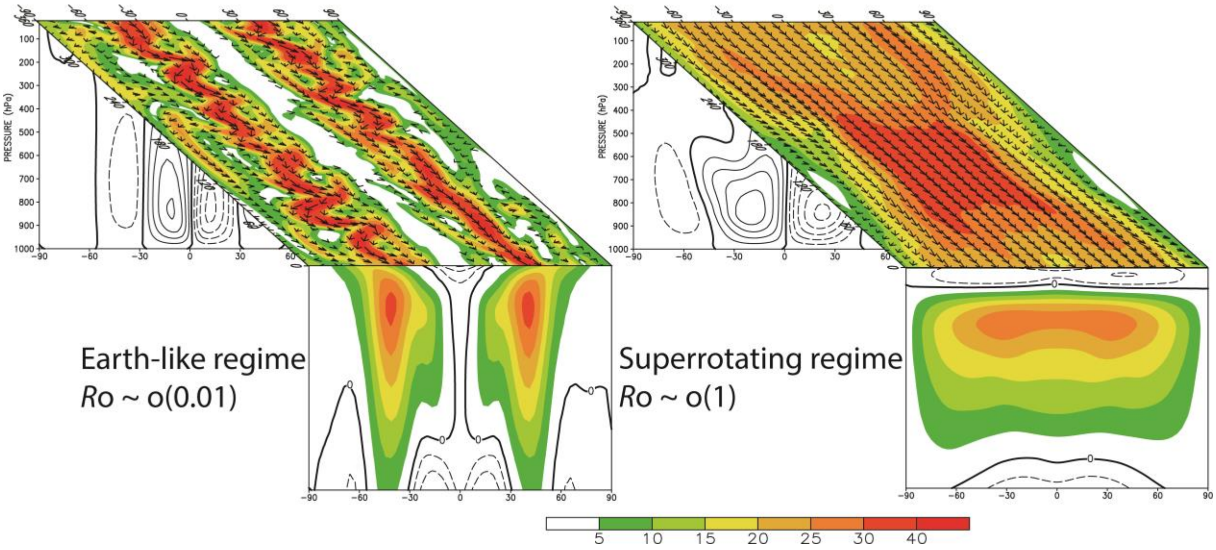

Figure 5.1 – Zonal mean zonal wind and stream function taken from Figure 3.3 to represent the main differences of the atmospheric general circulation between the Earth-like and the superrotating regimes. The horizontal plot refers to an instantaneous snap-shot of the wind magnitude and direction.

The analysis showed that superrotation could only emerge in a planet of slow rotation rate if the damping was weak and the thermal time scales in the atmosphere were long enough. This fact can be represented by the solid arrows in Figure 5.2, which indicate the reduction of the friction effects and the increase of the thermal inertia in the slowly-rotating simulation. Thus when only the rotation rate is reduced our model generated a nearly axisymmetric circulation with intense Hadley cells, which prevents the development of superrotation. In this case friction was strong and the thermal inertia was shorter, which is represented by the dashed arrow pointing upward on the left Figure 5.2. Therefore, a large Rossby number is a necessary condition but not sufficient one to achieve superrotation; Hadley cell intensity seems also to be important.

Further studies aiming the effects of changes in the thermal structure of the Held-Suarez benchmark, and how that could affect the Hadley cell strength, are necessary to understand how the overturning circulation influences superrotation.

The changes in different elements of a simulation and how they can interfere in the resulting circulation pattern can be evaluated by estimating nondimensional numbers, even for more complex models. Interestingly, simulations with different dimensional parameters but the same nondimensional numbers share the same behavior of mean general atmospheric circulation, and therefore a GCM satisfies the principle of dynamical similarity (Figure 5.2). Based on that, superrotation should not be thought of as a phenomenon that only occurs on slowly rotating planets, since for instance superrotation could be also present on fast-rotating planets if they are sufficiently small.

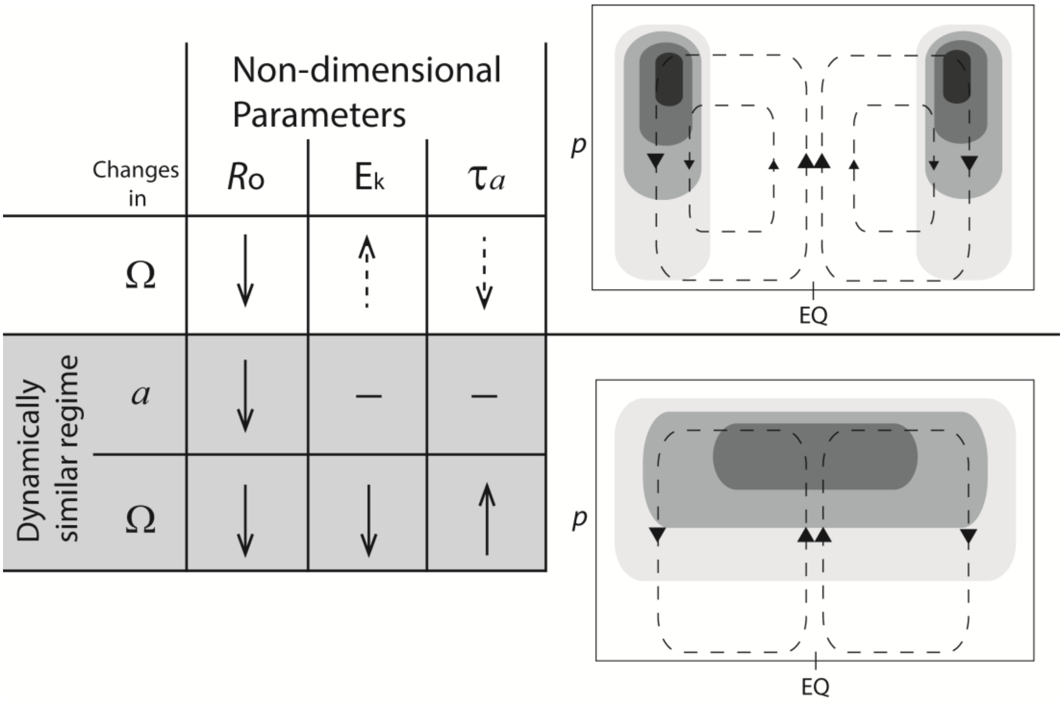

Figure 5.2 – Relation between the simulated zonal mean circulation and the non-dimensional parameters of Rossby (R_O), Ekman (E_K) and Thermal (τ_a) numbers. The solid arrows indicate direct changes of these numbers whereas the dashed arrows depict indirect changes caused by only modifiying in the planetary rotation rate. The winds and mean overturning circulation (arbitrary scale) show the mean pattern obtained in different arrangement of the parameters.

Considering the momentum balance between mean meridional circulation and eddy transports, as described by the Gierasch-Rossow-Williams mechanism, the numerical results presented here represent one consistent, dynamical model that explains how superrotation is maintained in a superrotating higher Rossby number planetary circulation. The mean zonal flow was maintained by only evoking the dynamical interaction between Rossby waves to converge eddy momentum fluxes at the equatorial region (Figure 5.3). If we estimate an averaged value of Rossby number by using typical scales of mean velocity, rotation rate and planetary radius for Venus, Titan and the simulation described here, it would be obtained values around 27.6, 4.3 and 1.3. This indicates the dynamical regime of the numerical experiment closely approaches Titan's, and therefore it could represent one possible mechanism for the superrotation in the atmosphere of Saturn's moon. Additional studies focusing on search and detection of planetary, large-scale waves in the upper and lower levels of Titan's atmosphere are required for validation. Among the myriad of planets that have been found each year outside the Solar System, it is possible that the results described here could be used to explain superrotation in slow-rotating extrasolar planets as well.

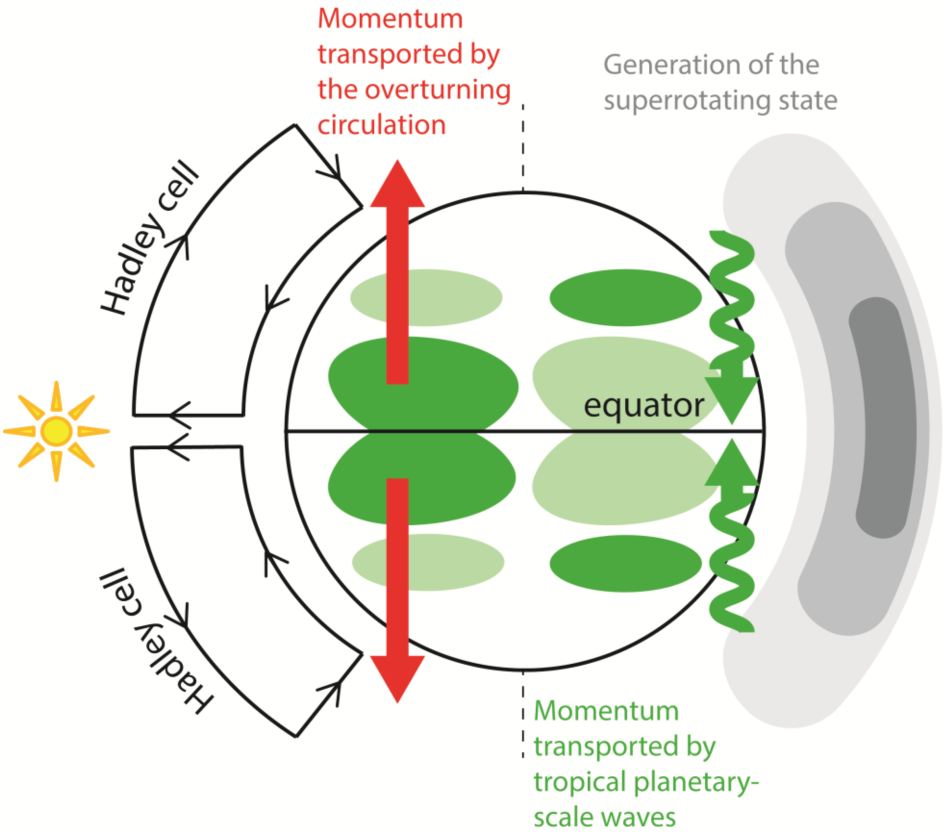
Momentum
transported by
the overturning
circulation
Generation of the
superrotating state
Hadley cell
equator
Hadley cell
Momentum
transported by
tropical planetary-
scale waves

Figure 5.3 – Sketched view of the main transport and momentum balance in a superrotating atmosphere: the role of tropical modes.

Although most of the literature used here to explain the wave structure and energetics is related to processes that take place in Earth's atmosphere, the results are straightforward and could represent a modification of the GRW mechanism. The analysis also demonstrated the possibility that different wave couplings can generate superrotation, indicating that multiple paths could be possible to produce such a regime. Further model inter-comparison may help to illuminate this variety of waves that participate in generating and maintaining spontaneous superrotation. Additionally many aspects of the interaction between waves and the mean flow under a high Rossby number regime remain unclear. Since quasi-geostrophic theory cannot be applied in such slowly-rotating systems, traditional ideas about mid-latitude instabilities cannot be used as well. Further theoretical study of equatorial waves in higher Rossby number regime is also needed, in order to better understand the dynamical behavior of these disturbances.

REFERENCES

ARNOLD, N. P.; TZIPERMAN, E.; FARRELL B. Abrupt Transition to Strong Superrotation Driven by Equatorial Wave Resonance in an Idealized GCM. **Journal of Atmopheric Sciences**, 69, p. 626–640, 2012.

ASNANI, G. C. **Tropical Meteorology**. Vol. 1, Pune: Indian Institute of Tropical Meteorology, 1993, 603 p.

BELTON, M. J. S. et al. Cloud Patterns, Waves and Convection in the Venus Atmosphere. **Journal of Atmopheric Sciences**, 33, p. 1394–1417, 1976.

BIRD, M. K. et al. The vertical profile of winds on Titan. **Nature**, 438, p. 800–802. 2005.

BOUGHER S. W.; HUNTEN, D. M.; PHILLIPS, R. J. **Venus II – Geology, Geophysics, Atmosphere and Solar Wind Environment**. Tucson: The University of Arizona Press, 1997, 1362 p.

BOYD, J. P. The Effects of Latitudinal Shear on Equatorial Waves. Part II: Applications to the Atmosphere. **Journal of Atmopheric Sciences**, 35, p. 2259–2267, 1978.

BRENNAN, F. E.; VINCENT, D. G. Zonal and Eddy Components of the Synoptic-Scale Energy Budget during Intensification of Hurricane Carmen (1974). **Monthly Weather Review**, 108, p. 954-965. 1980.

CABALLERO, R.; HUBER, M. Spontaneous transition to superrotation in warm climates simulated by CAM3. **Geophysical Research Letters**, 37, L11701, 2010.

CARLSON, T. N. **Mid-latitude weather systems**. Boston: American Meteorological Society. 1991, 507 pp.

DEL GENIO, A.; ROSSOW, W. B. Planetary-Scale Waves and the Cyclic Nature of Cloud Top Dynamics on Venus. **Journal of Atmopheric Sciences**, 47, p. 293–318, 1990.

DEL GENIO, A.; SUOZZO, R. J. A comparative study of rapidly and slowly rotating circulation regimes in a terrestrial general circulation model. **Journal of Atmopheric Sciences**, 44, p. 973–986, 1987.

DEL GENIO, A.D.; ZHOU, W. Simulations of superrotation of slowly rotating planets: Sensitivity to rotation and initial condition. **Icarus**, 120, p. 332–343, 1996.

DEL GENIO, A.D.; ZHOU, W.; EICHLER, T.P. Equatorial superrotation in a slowly rotating GCM: Implications for Titan and Venus. **Icarus**, 101, p. 1–17, 1993.

DOMARACKI, A.; LOESCH, A. Z. Nonlinear Interactions Among Equatorial Waves. **Journal of Atmopheric Sciences**, 34, p. 486–498, 1977.

EADY, E. Long waves and cyclone waves. **Tellus**, 1, p. 33–52, 1949.

FLASAR, F. M. Atmospheric Dynamics and Meteorology. In: **Titan from Cassini-Huygens**. Chap. 13, p. 323–352, 2009. Edited by R. Brown, J. P. Lebreton and J. Hunter Waite.

FRIEDSON, A. J. et al. A global climate model of Titan´s atmosphere and surface. **Planetary and Space Sciences**, 57, p. 1931–1949, 2009.

GEISLER, J.E.; PITCHER, E.J.; MALONE, R.C. Rotating-fluid experiments with an atmospheric general circulation model. **Journal of Geophysical Research**, 88, p. 9706–9716, 1983.

GIERASCH, P. J. Meridional Circulation and the Maintenance of Venus Atmospheric Rotation. **Journal of Atmopheric Sciences**, 32, p. 1038–1044, 1975.

GROTJAHN, R. **Global Atmospheric Circulation: Observations and Theories**. Oxford: Oxford University Press, 1993, 452 p.

HANNACHI, A.; JOLLIFFE, I. T; STEPHENSON, D. B. Empirical orthogonal functions and related techniques in atmospheric science: A review. **International Journal of Climatology**, 9, p. 1119–1152, 2007.

HAYASHI, Y. Space-Time Spectral Analysis and its Applications to Atmospheric Waves. **Journal of the Meteorological Society of Japan**, **60¸** p. 156–170, 1982.

HELD, I. **Equatorial Superrotation in Earth-like Atmospheric Models**. Bernhard Haurwitz Memorial Lecture, Boston: American Meteorological Society, 1999.

HELD, I. M; SUAREZ, M. J. A proposal for intercomparison of the dynamical cores of Atmospheric general circulation models. **Bulletin of the American Meteorological Society**, 75, p. 1825–1830, 1994.

HELD, I. M.; HOU, A. Y. Nonlinear axially symmetric circulation in a nearly inviscid atmosphere. **Journal of Atmopheric Sciences**, 35, p. 515–533, 1980.

HIDE, R. Dynamics of the Atmospheres of the Major Planets with an Apendix on the Viscous Boundary Layer at the Rigid Bounding Surface of an Electrically-Conducting Rotating Fluid in the Presence of a Magnetic Field. **Journal of Atmopheric Sciences**, 26, p. 841–853, 1969.

HOLLINGSWORTH J. L., et al. A simple-physics global circulation model for Venus: Sensitivity assessments of atmospheric superrotation. **Geophysical Research Letters**, 34, L05202, 2007.

HOLTON, J. R. **An Introduction to Dynamic Meteorology**. 4th Edition, New York: Elsevier Academic Press, 2004, 535 p.

HOURDIN, F. Numerical simulation of the general circulation of the atmosphere of Titan. **Icarus**, 117, p. 358–374, 1995.

HUNT, B. G. The influences of the Earth's rotation rate on the general circulation of the atmosphere. **Journal of Atmopheric Sciences**, 36, p. 1392–1408, 1979.

IGA, S.-I.; MATSUDA, Y. Shear Instability in a Shallow Water Model with Implications for the Venus Atmosphere. **Journal of Atmopheric Sciences**, 62, p. 2514–2527, 2005.

IMAMURA, T. Meridional Propagation of Planetary-Scale Waves in Vertical Shear: Implication for the Venus Atmosphere. **Journal of Atmopheric Sciences**, 63, p. 1623–1636, 2006

JAMES, I. **Introduction to Circulating Atmosphere**. Cambridge: Cambridge University Press, 1994, 422 pp.

JAMES, I.; GRAY, L. Concerning the effect of surface drag on the circulation of a baroclinic planetary atmosphere. **Quarterly Journal of The Royal Meteorological Society**, 112, p. 1231–1250, 1986.

KILADIS, G. N. et al. Convectively coupled equatorial waves. **Reviews of Geophysics**, 47, RG2003, 2009.

KOSTIUK, T. Direct measurement of winds on Titan. **Geophysical Research Letters**, 28, p. 2361–2364, 2001.

KOUYAMA, T. et al. Horizontal structure of planetary-scale waves at the cloud top of Venus deduced from Galileo SSI images with an improved cloud-tracking technique. **Planetary and Space Sciences**, 60, p. 207-216, 2012.

KRAUCUNAS, I.; HARTMANN, D. L. Equatorial Superrotation and the Factors Controlling the Zonal-Mean Zonal Winds in the Tropical Upper Troposphere. **Journal of Atmospheric Sciences**, 62, p. 371–389, 2005.

LEBONNOIS, S. et al. Superrotation of Venus' atmosphere analyzed with a full general circulation model. **Journal of Geophysical Research**, 115, E06006, 2010.

LEBONNOIS, S. et al. Angular momentum budget in General Circulation Models of superrotating atmospheres: A critical diagnostic. **Journal of Geophysical Research**, 112, E12004, 2012.

LEE, C.; LEWIS, S. R.; READ, P. L. A numerical model of the atmosphere of Venus. **Advances in Space Research**, 36, p. 2142–2145, 2005.

LEE, C.; LEWIS, S. R.; READ, P. L. Super-rotation in a Venus general circulation model. **Journal of Geophysical Research**, 112, E04S11, 2007.

LINDZEN, R. S. **Dynamics in atmospheric physics**. Cambridge: Cambridge University Pres, 1990, 310 p.

LORENZ, E. N. Available potential energy and the maintenance of the general circulation, **Tellus**, 7, p. 157–167, 1955.

LORENZ, E. N. **Empirical orthogonal functions and statistical weather prediction**, Rep. 1, Statist. Forecasting Project. Boston: Massachusetts Institute of Technology, 1956, 52 pp.

LORENZ, E. N. **The nature of the general circulation of the atmosphere**. Genebra: World Meteorological Organization, No. 218, TP. 115, 1967, 161 pp.

LORENZ, E. N. **The nature of general circulation of the atmosphere: a present view**. In: The global circulation of the atmosphere. London: *Royal Meteorological Society*, 1969, p. 2–23.

LUZ, D.; HOURDIN, F. Latitudinal transport by barotropic waves in Titan's stratosphere: I. General properties from a horizontal shallow-water model. **Icarus**, 166, p. 328–342, 2003.

MAJDA, A. J.; BIELLO, J. A. The Nonlinear Interaction of Barotropic and Equatorial Baroclinic Rossby Waves. **Journal of Atmospheric Sciences**, 60, p. 1809–1821, 2003.

MATSUNO, T. Quasi-geostrophic motion in the equatorial area. **Journal of the Meteorological Society of Japan**, 44¸ p. 24–43, 1966.

MITCHELL, J. L.; VALLIS, G. K.. The transition to superrotation in terrestrial atmosphere. **Journal of Geophysical Research**, E12008, 2010.

MITCHELL, J. L. Titan’s transport-driven methane cycle. **Astrophysical Journal Letters**, 756, L26, 2012.

MITCHELL, J. L. et al. Locally enhanced precipitation organized by planetary-scale waves on Titan. **Nature Geosciences**, 4, p. 589-592, 2011.

NAVARRA, A.; BOCALLETTI, G. Numerical general circulation experiments of sensitivity to Earth rotation rate. **Climate Dynamics**, 19, p. 467–483, 2002.

NEWMAN, C. et al. Stratospheric superrotation in the TitanWRF model. **Icarus**, 213, p. 636–654, 2011.

NORTH, G. R. Empirical Orthogonal Functions and Normal Modes. **Journal of Atmospheric Sciences**, 41, p. 879–887, 1984.

OORT, A. H. On estimates of atmospheric energy cycle. **Monthly Weather Review**, p. 92, p. 483–493. 1964.

PARISH, H. F. Decadal variations in a Venus general circulation model. **Icarus**, 21**2**, p. 42–65, 2011.

PASCALE, S. et al. Nonequilibrium thermodynamics of circulation regimes in optically thin, dry atmospheres. **Planetary and Space Sciences**, 84, p. 48–65, 2013.

PEIXOTO, J. P.; OORT, A. H. **Physics of Climate**. American Institute of Physics, 1992, 520 p.

POTTER, S. F.; VALLIS, G. K.; MITCHELL, J. L. Spontaneous Superrotation and the Role of Kelvin waves in an Idealized Dry GCM. **Journal of Atmospheric Sciences**, 71, p. 596–614, 2014.

RANDEL, W. J.; HELD, I. M. Phase Speed Spectra of Transient Eddy Fluxes and Critical Layer Absorption. **Journal of Atmospheric Sciences**, 48, p. 688–697, 1991.

READ, P. Dynamic and circulation regimes of terrestrial planets. **Planetary and Space Sciences**, 59, p. 900–914, 2011.

REZNIK, G. M.; ZEITLIN, V. The interaction of free Rossby waves with semi-transparent equatorial waveguide – wave-mean flow interaction. **Nonlinear Processes in Geophysics**, 16, p. 381–392, 2009.

RICHARDSON, M. I.; TOIGO, A. D.; NEWMAN, C. E. PlanetWRF: A general purpose, local to global numerical model for planetary atmospheric and climate dynamics. **Journal of Geophysical Research**, 112, E09001, 2007.

ROSSOW, W. B.; WILLIAMS, G. Large-Scale Motion in Venus Stratosphere. **Journal of Atmospheric Sciences**, 36, p. 377–389, 1979.

SÁNCHEZ-LAVEGA, A. Variable winds on Venus mapped in three dimensions. **Geophysical Research Letters**, 35, L13204, 2008.

SARAVANAN, R. Equatorial Superrotation and Maintenance of the General Circulation in Two-Level Models. **Journal of Atmospheric Sciences**, 50, p. 1211–1227, 1993.

SCHNEIDER, T. The general circulation of the atmosphere. **Annual Review of Earth and Planetary Sciences**, 34, p. 655–688, 2006.

SHELL, K. M.; HELD, I. M. Abrupt Transition to Strong Superrotation in an Axisymmetric Model of the Upper Troposphere. **Journal of Atmospheric Sciences**, 61, p. 2928–2935, 2004.

SKAMAROCK, W. C. et al. **A description of the Advanced Research WRF Version 3**, NCAR Tech. Note 475+STR, Boulder: National Center for Atmospheric Research, Boulder, 2008, 125 pp.

SMITH, M. D.; GIERASCH, P. J.; SCHINDER, P. J. A Global Traveling Wave on Venus. **Science**, 256, p. 652 – 655, 1992.

SMITH, M. D.; GIERASCH, P. J.; SCHINDER, P. J. Global-Scale Waves in the Venus Atmosphere. **Journal of Atmospheric Sciences**, 50, 4080–4096. 1993.

STAR, V. P. An essay on general circulation of the Earth's atmosphere. **Journal of Meteorology**, 5, p. 39-43, 1948.

TOIGO, A. et al. The impact of resolution on the dynamics of the martian global atmosphere: Varying resolution studies with the MarsWRF GCM. **Icarus**, 221, p. 276–288, 2012.

TOKANO, T. Near-surface winds at the Huygens site on Titan: interpretation by means of a general circulation model. **Planetary and Space Sciences**, 55, p. 1990–2009, 2007.

TOKANO, T. et al. Seasonal variation of Titan's atmospheric structure simulated by a general circulation model. **Planetary and Space Sciences**, 47, p. 493–520, 1999.

VALLIS, G. K. **Atmospheric and Ocean Fluid Dynamics**. Cambridge: Cambridge University Press, 2006, 745 p.

WANG, B.; XIE, X. Low-Frequency Equatorial Waves in Vertically Sheared Zonal Flow. Part. I: Stable Waves. **Journal of Atmospheric Sciences**, 53, p. 449–467, 1996.

WANG, P.; MITCHELL, J. L. Planetary ageostrophic instability leads to superrotation. **Geophysical Research Letters**, 41, p. 4118–4126, 2014.

WHEELER, M.; KILADIS, G. N. Convectively coupled equatorial waves: Analysis of clouds and temperature in the wavenumber-frequency domain. **Journal of Atmospheric Sciences**, 56, p. 374–399, 1999.

WIDEMANN, T.; LELLOUCH, E.; DONATI, J-F. Venus Doppler winds at cloud tops observed with ESPaDOns at CFHT. **Planetary and Space Sciences**, 56, p. 1320–1334, 2008.

WIIN-NIELSEN, A.; CHEN, T. C. **Fundamentals of Atmospheric Energetics**. Oxford: Oxford University Press, New York, 1993, 376 p.

WILLIAMS, G. P. The dynamical range of global circulations — I. **Climate Dynamics**, 2, p. 205– 260, 1988a.

WILLIAMS, G. P. The dynamical range of global circulations — II. **Climate Dynamics**, 3, p. 45–84, 1988b.

WILLIAMS, G. P. Barotropic Instability and Equatorial Superrotation. **Journal of Atmospheric Sciences**, 60, p. 2136–2152, 2003.

WILLIAMS, G.P.; HOLLOWAY, J. L. The range and unity of planetary circulations. **Nature**, 297, p. 295–299, 1982.

XIE, X.; WANG, B. Low-Frequency Equatorial Waves in Vertically Sheared Zonal Flow. Part. II: Unstable Waves. **Journal of Atmospheric Sciences**, 53, p. 3589–3605. 1996.

YAMAMOTO, M.; TAKAHASHI, M. The fully developed superrotation simulated by a general circulation model of a Venus-like atmosphere. **Journal of Atmospheric Sciences**, 60, p. 561–574, 2003.

YAMAMOTO, M.; TAKAHASHI, M. Venusian middle-atmospheric dynamics in the presence of a strong planetary-scale 5.5-day wave. **Icarus**, 217, 702–713. 2012.

YAMAMOTO, M.; TAKAHASHI, M. Superrotation Maintained by Meridional Circulation and Waves in a Venus-like GCM. **Journal of Atmospheric Sciences**, 63, p. 3296–3314, 2006.

ZANGVIL, A.; YANAI, M. Upper-Tropospheric Waves in the Tropics. Part. I: Dynamical Analysis in the Wavenumber-Frequency Domain. **Journal of Atmospheric Sciences**, 37, p. 283–298, 1980.

ZHANG, C.; WEBSTER, P. J. Effects of Zonal Flows on Equatorially Trapped Waves. **Journal of Atmospheric Sciences**, 46, p. 3632–3652, 1989.